2016

Deformation Of Multifunctional Materials At Various Time And Length Scales: A DIC-Based Study

Behrad Koohbor
University of South Carolina

Recommended Citation
Koohbor, B.(2016). *Deformation Of Multifunctional Materials At Various Time And Length Scales: A DIC-Based Study.* (Doctoral dissertation). Retrieved from https://scholarcommons.sc.edu/etd/3896

DEFORMATION OF MULTIFUNCTIONAL MATERIALS AT VARIOUS TIME AND LENGTH SCALES: A DIC-BASED STUDY

by

Behrad Koohbor

Bachelor of Science
Sharif University of Technology, 2008

Master of Science
Sharif University of Technology, 2011

Submitted in Partial Fulfillment of the Requirements

For the Degree of Doctor of Philosophy in

Mechanical Engineering

College of Engineering and Computing

University of South Carolina

2016

Accepted by:

Addis Kidane, Major Professor

Michael A. Sutton, Committee Member

Xiaomin Deng, Committee Member

Wei-Yang Lu, Committee Member

Cheryl L. Addy, Vice Provost and Dean of the Graduate School

ACKNOWLEDGEMENTS

First I wish to offer my sincere gratitude to Dr. Addis Kidane, my research advisor, for his continued support and generous guidance over the entire course of my PhD studies.

Dr. Michael Sutton is highly acknowledged here for his encouragement, inspiring nature and support in a number of ways. Dr. Wei-Yang Lu is sincerely acknowledged for his financial support of one of the projects, as well as his constructive suggestions and ideas. I gratefully acknowledge Dr. Xiaomin Deng for his positive mindset and valuable comments on my work. I am also grateful to Dr. Michel Van Tooren, for his valuable comments during my comprehensive exam, and Dr. David Rocheleau for his assistance and guidance.

I would also like to express my gratitude to my fellow graduate and undergraduate students: Silas Mallon, Suraj Ravindran, Addis Tessema, Ali Fahem, Guillermo Valeri, Milad Rohanifar, Ronak Patel, Peter Malchow and Abigail Wohlford. Former graduate student Silas Mallon is especially acknowledged for his friendship and many contributions to all the projects I have been involved in. My gratitude is extended to Bill Bradly, David Westbury, Renee Jenkins, Lalitha Ravi and Misty O’Donnell, for their kind assistance.

Finally and most importantly, I would like to thank my beloved wife, Donya, my incredibly supportive parents, Bijan and Maryam, and my wonderful brother, Behshad, for their love and kindness, comfort, encouragement and emotional support.

ABSTRACT

The focus in the present work is to explore and characterize the underlying deformation and failure mechanisms in multifunctional materials including woven composites and polymeric foams, using full-field measurements. Attention has been especially drawn towards the challenges associated with characterizing these materials at extreme length and time scales, and investigating the advantages of full-field measurements to resolve the existing limitations. Accordingly, the current limitations in the study of dynamic deformation response of low-impedance materials are identified. An approach based on the general stress equilibrium is presented and successfully implemented to include the concurrent effects of inertia and material compressibility into the analysis of direct impact response of various low impedance rigid closed-cell foams. The approach takes advantage of full-field measurement based on stereovision digital image correlation (3D-DIC) to measure the full-field acceleration and material density, later used to determine the distribution of inertia stresses developed in the material. The inertia stress is superimposed with the boundary-measured stress to give the local variation of stress in the dynamically deformed specimen.

The rest of the work is dedicated to the characterization of orthogonally woven fiber reinforced composites, with emphasis on exploring the origin of deformation nonlinearity and orientation dependence of these materials when subjected to far-field loads. Attempts have been made to quantify the local deformations over fiber bundles and matrix-rich areas in woven composites with different reinforcements (glass fiber and carbon fiber) and different yarn dimensions. The full-field deformation captured through the use of 2D and 3D DIC at sub-millimeter scales is utilized to reveal the underlying load-bearing mechanisms, dominant failure modes and the origin of non-linearity in the global stress-strain response of the material subjected to in-plane axial tensile load. Results obtained through the application of full-field measurements are validated using post-mortem fracture surface study in the composites.

PREFACE

The present work addresses the full-field characterization of mechanical behavior of two material systems at various time and length scales. Material types presented herein include closed-cell cellular polymers (polymeric foams) and woven composites. Full-field measurements are conducted using 2D and 3D digital image correlation, presenting the versatility of this technique in multiscale deformation study of materials.

Chapter 1 provides a general background on the importance of characterizing the mechanical behavior of materials at elevated strain rates and at mesoscopic scales. Commonly used experimental approaches in the study of dynamic deformation response of low impedance materials with their current limitations are discussed. The challenges in the characterization of meso-scale deformation response of heterogeneous materials are also presented and discussed in a concise manner.

Chapter 2 presents a thorough investigation on the dynamic stress-strain response of rigid closed-cell polymeric foams under intermediate-velocity direct impact loading conditions. The application of high speed photography in conjunction with stereovision digital image correlation is highlighted by introducing a novel non-parametric approach by which the concurrent influences of inertia stresses and material compressibility can be included in the dynamic stress analysis.

Chapter 3 extends the application of the non-parametric analysis introduced in Chapter 2 to high-velocity impact loadings, where strong deformation gradients are produced in the material. An analytical approach has been introduced and successfully implemented to take advantage of the strong spatial variabilities in strain and strain rate in the identification of visco-plastic constitutive laws using minimum number of dynamic experiments.

Chapter 4 presents the application of the non-parametric approach in the study of constitutive response and energy absorption performance of closed-cell polymeric foams subjected to intermediate-velocity impact. Attempts have been made to design the impact experiments such that the material undergoes a complete loading-unloading cycle.

Chapter 5 focuses on the study of multi-scale deformation and failure mechanisms in an orthogonally woven glass fiber reinforced composite. Particular attention has been drawn towards the influence of fiber orientation angle on the meso-scale load bearing mechanisms and apparent failure response of the examined material.

Chapter 6 presents a thorough study conducted to reveal the source of deformation nonlinearity and large global failure strains in off-axis woven composites subjected to in-plane tension. The evolution of meso-scale strain distribution over fiber-rich and matrix-rich regions has been obtained using full-field measurements. Fiber trellising mechanism is studied in detail in this chapter.

Finally, a concise summary of the present work and recommendations for future research are presented in Chapter 7.

TABLE OF CONTENTS

LIST OF TABLES

LIST OF FIGURES

CHAPTER 1

INTRODUCTION

1.1 DYNAMIC MECHANICAL BEHAVIOR OF POLYMERIC FOAMS: CHALLENGES AND PROPOSED SOLUTIONS

Characterizing the deformation and failure mechanisms of cellular polymers at elevated strain rates have been a subject of great interest in the engineering community for decades. The idea is mainly supported by the fact that the variations in mechanical and failure response of polymeric foams take place rapidly with increasing the rate of deformation imposed on the material (see e.g. Figure 1.1) [1]. Such significant strain rate sensitivity is associated with (1) rate sensitive mechanical response of the parent solid polymer [2, 3]; and (2) the release rate of the gas entrapped within the closed cellular structure of the material [4].

Regardless of what the sources of such strong strain rate sensitivity of polymeric foams are, accurate assessment of the dynamic mechanical properties of polymeric foams is of great significance. The importance in characterizing high strain rate constitutive response of polymeric foams is essentially supported by the fact that many applications of these material inherently entail high loading rates; while due the unavailability of well-defined and reliable constitutive models, foam structures are usually designed based on their quasi-static constitutive models.

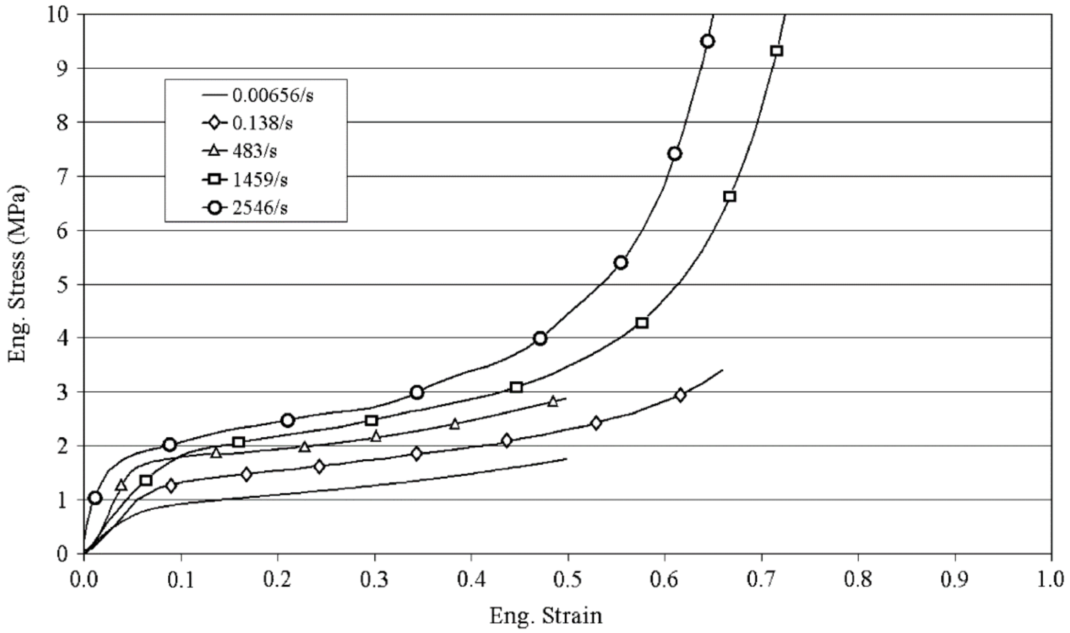

Figure 1.1 Stress-strain curves at different strain rates for a closed-cell expanded polystyrene (EPS) foam with a bulk density of 112 kg/m^3 [1].

The reason behind the scarce constitutive information on polymeric foams is basically due to certain challenges confronted in dynamic testing of these materials. One particular challenge in this regard originates from the low mechanical impedance of the material, whereas such low impedance behavior is itself a direct result of the porous structure of polymer foams. The low mechanical impedance and its consequent low wave propagation speed result in a belated state of quasi-static stress equilibrium, and intensifies the challenges in the acquisition of an accurate dynamic stress-strain response using conventional boundary measurements.

From a material testing perspective, there have been a number of solutions proposed to remedy the issues associated with the delayed quasi-static stress equilibrium in dynamic testing of low impedance materials. These solutions include, but are not limited to the application of hollow and/or polymeric bars to reduce the impedance mismatch between the bars and the specimen in Hopkinson bar test [5], and pulse shaping techniques [6]. Although these solutions can diminish the unfavorable effects due to the belated stress equilibration to some extent, they are essentially applicable in the Hopkinson bars only. A more general solution that is independent of the testing apparatus is the use of short specimens in order to reduce the wave reverberation time and achieve stress equilibrium in a shorter duration. However, shortening the specimen can impose other adverse effects which are: (1) decreasing the specimen length-to-diameter ratio promotes the adverse effects of end friction and results in the acquisition of inaccurate dynamic stress-strain curves [7]; (2) in particular case of cellular solids, the specimen dimensions must be such that the results would represent the effective continuum-scale response of the bulk material. In this regard the size of the representative volume element (RVE) of a cellular material may impose limitations on the dimensions of the test specimen [8, 9].

Recent advances in the areas of high speed photography and full-field measurements have provided an alternative solution for the above-mentioned limitations. Particularly, the extensive recent development of digital image correlation (DIC) has shown the great potential of this full-field measurement technique in the study and dynamic deformation and failure response of materials under high speed deformation conditions. In light of this, for the specific case of low impedance materials, direct measurement of acceleration and inertia stress fields facilitated by DIC, have made it possible to directly evaluate the non-equilibrium state of stress, without the necessity for design and application of complicated experimental approaches and/or specimen size consideration. The basic idea in this regard is the calculation of acceleration from the displacement field, determination of the inertia stresses using acceleration data over the entire field of interest, and finally superimposing the inertia stresses with the boundary-measured stress to obtain the distribution of total stress on the surface of the deformed specimen [10].

The fundamental idea of using full-field data to compensate for limitations due to the transient stress state has been successfully implemented in a number of studies to investigate the dynamic deformation and failure response of various material systems [11-14]. Following the successful application of full-field measurements in characterization of deformation response of low impedance materials, our objective in the first part of the present document is to provide an in-depth study on the fundamental ideas and experimental methodology in characterizing the constitutive response of rigid closed-cell polymeric foams subjected to direct impact loading conditions. Attempts have made to present a systematic approach that facilitates (1) the acquisition of dynamic stress-strain response of polymeric foams over strain rates of 1000-5000 s^{-1}; (2) characterization of energy absorption performance of polymeric foams subjected to high strain rate loading. Finally, effective stress-strain curves obtained using full-field measurements are compared with the nominal stress-strain data obtained from conventional boundary force and displacement measurements and the differences are discussed.

1.2 MESO-SCALE DEFORMTION IN WOVEN COMPOSITES

Deformation response of fiber composites is established to be heterogeneous. This deformation heterogeneity is a direct result of the very different mechanical behaviors of the two constituents in fiber composites, i.e. fibers and matrix material, as well as complex interfacial mechanisms both between fibers and matrix, and in between different laminas in a composite sheet.

In particular case of woven composites, it has been documented that the macroscale mechanical and failure responses follow a non-linear trend and vary significantly with changing the angle between the applied load and the fiber directions [15-17]. The complex deformation mechanisms giving rise to such orientation-dependent nonlinear response can be investigated through the study of deformation response at micro and meso-scales [18]. Although micro-scale studies can provide useful information on the response of individual components in a woven composite, they are basically incapable of providing any evidence on the prevailing fiber-matrix interaction mechanisms. On the other hand, meso-scale analyses are established to overcome this limitation by allowing the accurate examination of deformation at yarn scales [19-22]. Data extracted from meso-scale studies on woven composites not only reveals the governing deformation mechanisms, but can also be used to capture the local deformation response in order to validate micromechanical and finite element modeling approaches, the concepts which are currently of great interest in the composite research community [23-25].

It is worth noting that with the rapidly growing applications of micromechanical approaches in the composite research community, more attention is being drawn towards the use of meso-scale observations and measurements on different classes of composites. One particular challenge in the application of micromechanics for fiber reinforced composites is that the mechanical response of individual constituents, i.e. fibers and matrix material, must always be used as the input without accounting for the ‘effective response’ of the material when the two components are placed together inside the composite. Moreover, complex interactions between fibers and matrix need to be explored using very complicated experimental approaches, to be later used as another set of input into a micromechanics-based code [23]. Last but not least, it is a common practice to take advantage of homogenization algorithms in micromechanical approaches to identify ‘effective’ constitutive behaviors. Such homogenization algorithms, on the other hand, must be carried out over a carefully selected volume of the material that is sufficiently small to capture the contribution of the individual constituents, and large enough to be representative of the bulk response of the examined composite [26, 27]. Therefore, although the application of micromechanics is indeed a promising approach in modeling and design of composite structures, several challenges are faced due to the use of appropriate properties as the input.

In recent years, the application of full-field measurements has been extended to the meso-scale deformation study of fiber composites, mainly due to their capability in validating the numerical-based studies. DIC-based characterization of meso-scale response in woven and textile composites has been conducted, mostly with the purpose of providing a qualitative measure for the heterogeneous deformation. In addition, optical-based DIC measurements have commonly been carried out over larger areas of interest, containing dimensions as large as several yarn widths, when dealing with the meso-scale study of fiber composites (see for instance [19]). A more detailed survey in the literature confirms the presence of a great gap in the research conducted with the purpose of studying meso-scale deformation response in woven composites focusing on quantitative analyses. The second part in the present research is dedicated to the study of meso-scale deformation characterization in woven composites at millimeter and submillimeter scales. Commonly used optical-based digital image correlation approaches have been implemented to identify the principal load-bearing and deformation mechanisms in on-axis and off-axis woven composites with various reinforcements (glass fiber and carbon fiber). Attempts are first made to establish a correlation between the meso-scale deformation patterns to the bulk failure mechanisms in glass fiber reinforced composites. This goal has been achieved by first identifying the locations on which local strains take low and high magnitudes. Extensive focus has been towards the effects of angle orientation in this section. Fiber trellising has been identified as the major mechanism behind the highly nonlinear stress-strain response, large strain-to-failure and shear fracture surface of the off-axis specimens. To provide more in-depth insight on fiber trellising mechanism in woven composites, an approach has been followed in which the experimental meso-scale deformation measurements are used in conjunction with simple mathematical models to facilitate decoupling local stretch and rotation magnitudes on the fiber bundles. It is finally revealed that relatively large global failure strains in off-axis specimens is associated with the rotation of fiber bundles towards the direction of the applied load; and that the final failure in woven composite is controlled by the maximum tensile strain tolerable by the reinforcing fibers.

1.3 PRESENT STUDY

The present study is aimed at the investigation of the mechanical behavior of two types of materials, namely polymeric foams and woven composites, at various time and length scales. The following have been studied in detail:

- Characterization of the dynamic deformation of cellular polymers subjected to intermediate and high-velocity direct impact, by implementing a novel non-parametric approach which takes into account the concurrent influences of inertia and material compressibility.
- Introduction and successful implementation of a novel idea that takes advantage of spatial and temporal variation of strain rate in an impacted specimen to identify viscoplastic constitutive information from a single impact test.
- Full-field deformation characterization and apparent failure mechanisms at mesoscopic scales in a woven glass fiber reinforced composite.
- Study and quantitative analysis of the underlying deformation response and fiber trellising mechanism in woven carbon fiber reinforced composites at meso-scales using full-field measurements.

1.4 LIST OF REFERENCES

[1] Oullet S, Cronin D, Worswick M. Compressive response of polymeric foams under quasi-static, medium and high strain rate conditions. Polymer Testing 2006; 25: 731-743.

[2] Mulliken AD, Boyce MC. Mechanics of the rate-dependent elastic-plastic deformation of glassy polymers from low to high strain rates. International Journal of Solids and Structures 2006; 43: 1331-1356.

[3] Yi J, Boyce MC, Lee GF, Balizer E. Large deformation rate-dependent stress-strain behavior of polyurea and polyurethanes. Polymer 2006; 47: 319-329.

[4] Bouix R, Viot P, Lataillade J. Polypropylene foam behavior under dynamic loadings: Strain rate, density and microstructure effects. International Journal of Impact Engineering 2009; 36: 329-342.

[5] Chen W, Zhang B, Forrestal MJ. A split Hopkinson bar technique for low-impedance materials. Experimental Mechanics 1999; 39: 81-85.

[6] Song B, Chen W, Frew DJ. Dynamic compressive response and failure behavior of an epoxy syntactic foam. Journal of Composite Materials 2004; 38: 915-936.

[7] Iwamoto T, Yokoyama T. Effects of radial inertia and end friction in specimen geometry in split Hopkinson pressure bar tests: A computational study. Mechanics of Materials 2012; 51: 97-109.

[8] Kanaun S, Tkachenko O. Representative volume element and effective elastic properties of open cell foam materials with random microstructures. Journal of Mechanics of Materials and Structures 2007; 2: 1607-1628.

[9] Tekoglu C, Gibson LJ, Pardoen T, Onck PR. Size effect in foams: Experiments and Modeling. Progress in Materials Science 2011; 56: 109-138.

[10] Pierron F, Zhu H, Siviour C. Beyond Hopkinson's bar. Philosophical Transactions of the Royal Society A 2014; 372: 20130195.

[11] Pierron F, Forquin P. Ultra-high-speed full-field deformation measurements on concrete spalling specimens and stiffness identification with the virtual fields method. Strain 2012; 48: 388-405.

[12] Moulart R, Pierron F, Hallett SR, Wisnom MR. Full-field strain measurement and identification of composites moduli at high strain rate with the virtual fields methods. Experimental Mechanics 2011; 51: 509-536.

[13] Othman R, Aloui S, Poitou A. Identification of non-homogeneous stress fields in dynamic experiments with a non-parametric method. Polymer Testing 2010; 29: 616-623.

[14] Yoon S, Giannakopoulos I, Siviour CR. Application of the virtual fields method to the uniaxial behavior of rubbers at medium strain rates. International Journal of Solids and Structures 2015; 69-70: 553-568.

[15] Ogihara S, Reifsnider KL. Characterization of nonlinear behavior in woven composite laminates. Applied Composite Materials 2002; 9: 249-263.

[16] Pollock P, Yu L, Sutton MA, Guo S, Majumdar P, Gresil M. Full-field measurements for determining orthotropic elastic parameters of woven glass-epoxy composites using off-axis tensile specimens. Experimental Techniques 2012; 38: 61-71.

[17] Lee D, Tippur H, Bogert P. Quasi-static and dynamic fracture of graphite/epoxy composites: An optical study of loading-rate effects

[18] Lam SW, Xue P, Tao XM, Yu TX. Multi-scale study of tensile properties and large deformation mechanisms of polyethylene terephthalate/polypropylene knitted composites. Composite Science and Technology 2003; 63: 1337-1348.

[19] Godara A, Raabe D. Influence of fiber orientation on global mechanical behavior and mesoscale strain localization in a short glass fiber-reinforced epoxy polymer composite during tensile deformation investigated using digital image correlation. Composite Science and Technology 2007; 67: 2417-2427.

[20] Boisse P, Zouari B, Gasser A. A mesoscopic approach for simulation of woven fibre composite forming. Composite Science and Technology 2005; 65: 429-436.

[21] Lomov SV, Boisse P, Deluycker E, Morestin F, Vanclooster K, Vandepitte D, Verpoest I, Willems A. Full-field strain measurements in textile deformability studies. Composites Part A-Applied Science 2008; 39: 1232-1244.

[22] Ivanov D, Ivanov S, Lomov S, Verpoest I. Strain mapping analysis of textile composites. Optics and Lasers in Engineering 2009; 47: 360-370.

[23] Lomov SV, Ivanov DS, Verpoest I, Zako M, Kurashiki T, Nakai H, Molimard J, and Vautrin A. Full-field strain measurements for validation of meso-FE analysis of textile composites. Compos Part A–Appl S 2008; 39: 1218-1231.

[24] Nicoletto G, Anzelotti G, Riva E. Mesoscopic strain field in woven composites: Experimental vs. finite element modeling. Optics and Lasers in Engineering 2009; 47: 352-359.

[25] Lomov SV, Ivanov DS, Verpoest I, Zako M, Kurashiki T, Nakai H, Hirosawa S. Meso-FE modelling of textile composites: Road map, data flow and algorithms. Composite Science and Technology 2007; 67: 1870-1891.

[26] Kanit T, Forest S, Galliet I, Mounoury V, Jeulin D. Determination of the size of the representative volume element for random composites: statistical and numerical approach. International Journal of Solids and Structures 2003; 40: 3647-3679.

[27] Xue P, Cao J, Chen J. Integrated micro/macro-mechanical model of woven fabric composites under large deformation. Composite Structures 2005; 70: 69-80.

CHAPTER 2

INVESTIGATION OF THE DYNAMIC STRESS-STRAIN RESPONSE OF COMPRESSIBLE POLYMERIC FOAM USING A NON-PARAMETRIC ANALYSIS [1]

---

[1] Koohbor B, Kidane A, Lu W, Sutton MA. *International Journal of Impact Engineering* 2016; 91: 170-182. doi:10.1016/j.ijimpeng.2016.01.007
Reused here with permission of publisher.

2.1 ABSTRACT

Dynamic stress-strain response of rigid closed-cell polymeric foams is investigated in this work by subjecting high toughness polyurethane foam specimens to direct impact with different projectile velocities and quantifying their deformation response with high speed stereo-photography together with 3D digital image correlation. The measured transient displacement field developed in the specimens during high stain rate loading is used to calculate the transient axial acceleration field throughout the specimen. A simple mathematical formulation based on conservation of mass is also proposed to determine the local change of density in the specimen during deformation. By obtaining the full-field acceleration and density distributions, the inertia stresses at each point in the specimen are determined through a non-parametric analysis and superimposed on the stress magnitudes measured at specimen ends, to obtain the full-field stress distribution. The process outlined above overcomes a major challenge in high strain rate experiments with low impedance polymeric foam specimens, i.e. the delayed equilibrium conditions can be quantified.

2.2 INTRODUCTION

The determination of a material’s constitutive behavior at intermediate to high strain rate ranges has been a subject of interest for quite a long time [1, 2]. Historically, the importance of obtaining equilibrium state has required special attention in the experimental setup, since configurations where equilibrium can be readily identified make it easier to study the dynamic stress-strain response of the materials. The issue is particularly significant in the case of engineering materials with low strength and low mechanical impedance [3], where conditions of stress/strain equilibrium oftentimes require a time duration that exceeds the time required for the material to undergo failure. In such cases, the determination of stress-strain response of the material based on the load and displacement measurement at specimen ends can introduce a significant degree of inaccuracy in the obtained constitutive response, with continued deterioration in accuracy at higher strain rates [4-6].

Polymeric foams, as a class of materials widely used in applications which require light weight structural design with superior energy dissipation characteristics, are among the materials possessing a low wave propagation speed [7-10]. Their use in areas such as automotive industries, ships and packaging requires precise knowledge of the deformation response of the material at different loading rates. Dynamic deformation and failure behavior of these materials have been studied both experimentally and numerically in recent years [11-16]. In general, most polymeric foams possess remarkable strain rate sensitivity at strain rates above 500 s^{-1} [14]. However, owing to non-homogeneity in the stress and deformation states, particularly during the early stages of dynamic loading, quantifying the dynamic deformation of foams has been a major challenge. One of the most widely used methods in studying the dynamic deformation behavior of soft materials is the split Hopkinson pressure bar technique [17]. Different approaches have been practiced in recent years to increase the accuracy of the measurements in this technique, particularly in testing of low impedance materials. These approaches include pulse shaping techniques [17], use of polymeric bars [18] and long projectiles [19]. A recent study by Liu et al. [16] indicates that in addition to the solutions proposed above, full-field measurements must be incorporated in order to accurately measure the deformation response and reveal the active failure mechanisms in foam specimens subjected to high strain rate loading conditions.

The advent of full-field measurement techniques such as digital image correlation (DIC), in conjunction with different experimental techniques has facilitated the study of deformation of materials in a wide range of time and length scales [16, 19-23]. More importantly, the recent work by Pierron and his group [20, 24, 25] using virtual fields and inverse methods has identified a unique way of analyzing the dynamic deformation of materials by using D'Alembert's principle and incorporating "inertia forces" into the analysis. Though the inverse methods have already been demonstrated to be effective in calculating the stress-stress response of materials at high strain rate loading conditions, the effect of compressibility has not been addressed in previous studies.

The present work focuses on the study of rigid closed-cell polymeric foams subjected to direct impact loading by accounting for material compressibility and the effect of inertia. A shock tube apparatus is used to apply dynamic loading on the foam specimens, while high speed stereovision imaging together with 3D digital image correlation is used to study the full-field deformation of the material under high strain rate loading conditions. A simple mathematical model has also been proposed to account for the material compressibility and the local variation of density during deformation of the specimens. Also, based on the full-field displacement distribution captured by DIC and considering the instantaneous change of material density, a non-parametric analysis is developed to incorporate "inertia effects" into the analysis, following references [5, 6].

Using the proposed methodology, the full-field stress-strain response of the material has been determined during high strain rate loading and the global constitutive behavior of the foam quantified. The original contribution here is the inclusion of the material compressibility into the analysis. In addition, attempts have been made to generalize the methodology to study the dynamic deformation of any low-impedance compressible solid. To the authors' knowledge, this is the first time a thorough analysis of the dynamic deformation of compressible polymeric foams has been performed taking into account the concurrent effects of material compressibility and inertia loading to capture the full-field stress-strain response of the material.

2.3 MATERIAL AND SPECIMEN GEOMETRY

The material used in this study is a rigid closed-cell polyurethane foam of 560 kg/m^3 (35 pcf) nominal density obtained from Sandia National Laboratories [26]. The initial density of the foam specimens was measured in-house and confirmed to be consistent with density values reported in the literature [26]; the measured value was 95% of literature data. A cylindrical foam specimen with a high contrast speckle pattern is shown in Figure 2.1a. The specimen is 25.4 mm in diameter and 25.4 mm in height. Each specimen was extracted from the as-received billets using a waterjet system, resulting in a relatively smooth lateral surface finish with +/- 0.1 mm dimensional variability. The high contrast speckle pattern shown in Figure 2.1a consists of a thin white sub-layer with randomly-distributed black speckles; the black speckles were applied using an airbrush. A histogram of the speckle pattern is shown in Figure 2.1b.

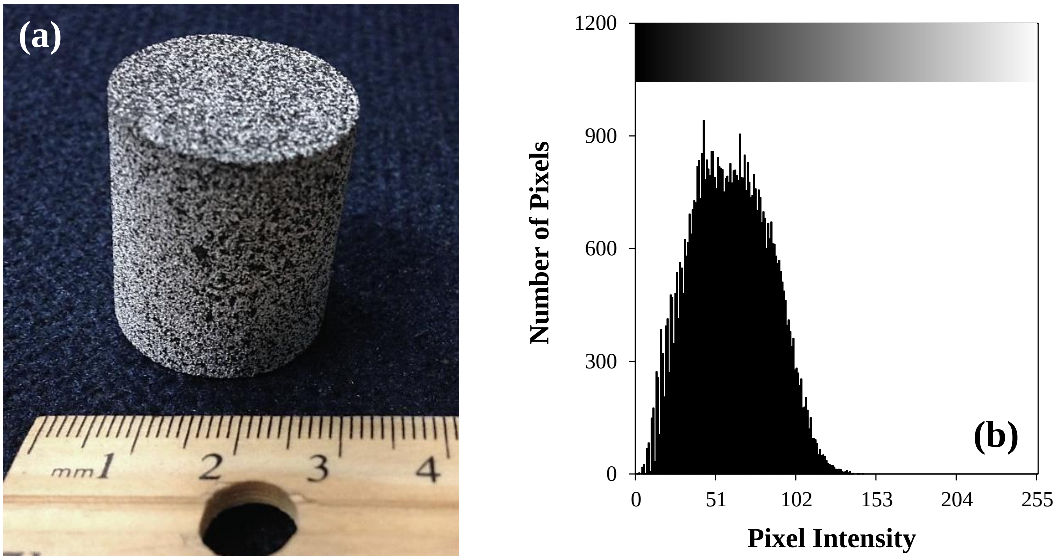

Figure 2.1 (a) Typical speckled specimen with its corresponding grey scale histogram shown in (b).

2.4 IMPACT LOADING

A shock tube apparatus was utilized to apply controlled dynamic loading on the specimens. The shock tube used in this work is shown in Figure 2.2. The apparatus has an overall length of 7.2 m, consisting of a 1.8 m driven section and a 5.4 m driver section. The inner diameter of the entire tube, except the last 0.9 m section near to the muzzle, is 75 mm. The inner diameter of the final 0.9 m end section of the tube is 50 mm, resulting in increasing shock velocity over the final stage.

To perform the experiment, the speckled cylindrical specimen shown in Figure 2.1 is placed at the muzzle of the shock tube and affixed to a custom fabricated strong-back. As shown in Figure 2.2, three piezotronic load-cells were placed behind the specimen and mounted on a specially fabricated fixture. Use of three load-cells in this work assures the accuracy of the force measurements and compensates for any possible misalignment of the loading which might occur during high strain rate experiments. The specimen is held on the loading fixture by the use of lithium grease, which also acts as the lubricant. Further details on the shock tube used in this work can be found elsewhere [4, 23, 27, 28].

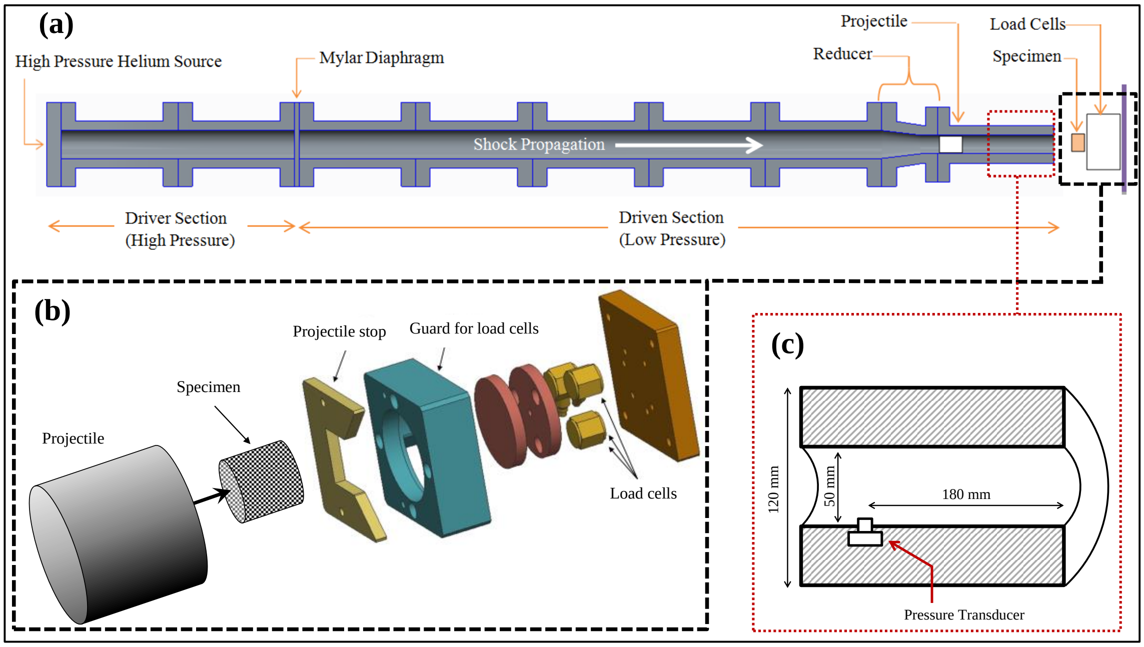

Figure 2.2 (a) The shock tube at its entirety, with the loading fixture shown in (b). The schematic of the shock tube muzzle and the pressure transducer are depicted in (c).

As shown in Figure 2.2, direct impact loading is applied using a projectile placed inside the tube at the beginning of the reducing section. The projectile was made of high strength 7068 aluminum alloy with a diameter 2 mm smaller than the inside diameter of the reducing section. The projectile was fabricated as a cylinder hollowed from one end, to reduce its mass, with an overall length of 72 mm, and a 0.07 kg mass. Prior to performing the experiment, the high pressure driver section and the low pressure driven section are separated by a diaphragm, a 0.18 mm thick stretched polyester film, under the commercial name Mylar. During testing, the driver section is pressurized using helium gas and as the pressure difference between the driver and driven sections reaches a critical value, the polyester film bursts, forming a shock wave that pushes the projectile towards the specimen side. The pressure and the velocity of the shock and the associated strain rate can be manipulated by varying the number and the thickness of diaphragms separating the driven and driver sections. In this work, two different strain rates were successfully applied on the specimen by using one and two sheets of diaphragms. The pressure profile developed inside the shock tube was measured using a piezotronic pressure sensor placed inside the tube near to the muzzle (see Figure 2.2). Maximum internal pressures of 250 kPa and 350 kPa were accordingly measured, by using one and two Mylar sheets, respectively.

Upon the formation of the shock inside the shock tube, the projectile is shot directly at the specimen, imposing a large strain rate magnitude on the deforming material. Stereo-imaging of the specimen was performed using two Photron SA-X2 high speed cameras. Triggering of the cameras was facilitated using the pressure transducer located inside and 180 mm behind the muzzle outlet of the tube (see Figure 2.2). The pressure transducer was connected to the oscilloscope so that the signal from the transducer could be used to trigger the cameras, as the internal pressure increased inside the tube. Repeatability of the results obtained from dynamic tests in this work was assured by testing two specimens for each strain rate conditions.

2.5 IMAGING SETUP AND DIGITAL IMAGE CORRELATION

The Photron SA-X2 cameras used in this work are equipped with 100 mm lenses. Images were acquired at a rate of 10^5 fps at 384×264 pixel^2 full-field resolutions resulting in inter-frame intervals of 10 μs. At 10^5 fps, the camera system used in this work allows the smallest exposure time of 1/996923 s; thus, an exposure time of 1 µs was used here. The load-cell data acquisition rate was synchronized with the imaging rate through a high speed data acquisition system and an oscilloscope.

Images acquired during the specimen deformation period were used as the input to the commercial DIC software Vic-3D® for quantitative 3D digital image correlation analysis. In this software, subset and step sizes of 39 pix and 9 pixel were selected, respectively; and the spatial resolution was calculated as 9.16 pixels/mm. Image correlation in Vic-3D was performed using ‘Normalized Squared Differences’ matching criterion, with optimized 8-tap interpolation, and first order (affine) shape functions. In this software, strains were derived from the full-field displacement using Gaussian filtering with a filter size of 13. Further details of the stereovision camera system parameters are listed in Table 2.1. The experimental setup including the shock tube and the stereovision camera arrangement system used in this work is shown in Figure 2.3.

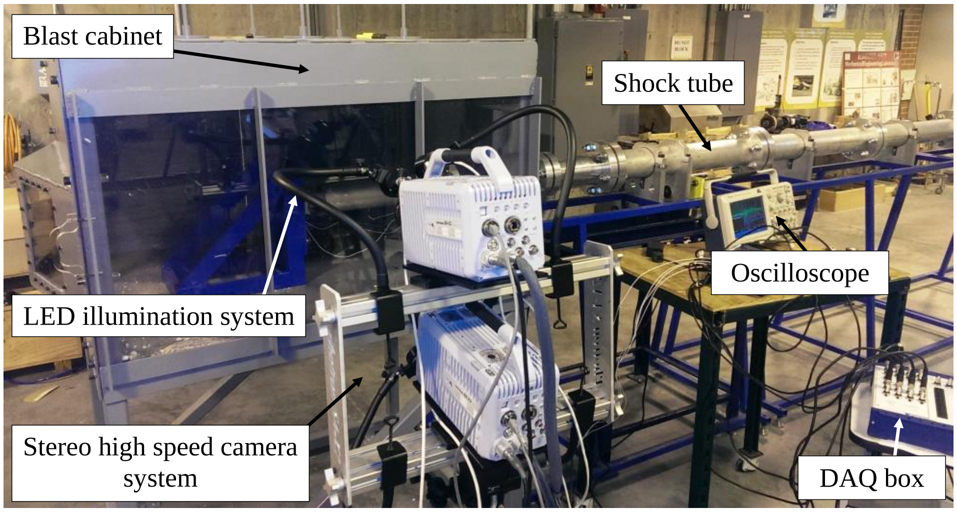

Figure 2.3 (a) The experimental setup including the shock tube and the stereovision camera system used in this work.

Table 2.1 System parameters obtained from calibration of the stereo camera arrangements used in this work

Parameter		Camera 1	Camera 2
Center - x	(pix)	148.7	167.5
Center - y	(pix)	24.2	43.9
Focal length - x	(pix)	5799.5	5708.3
Focal length - y	(pix)	5796.1	5705.3
Skew	(°)	-0.89	-0.48

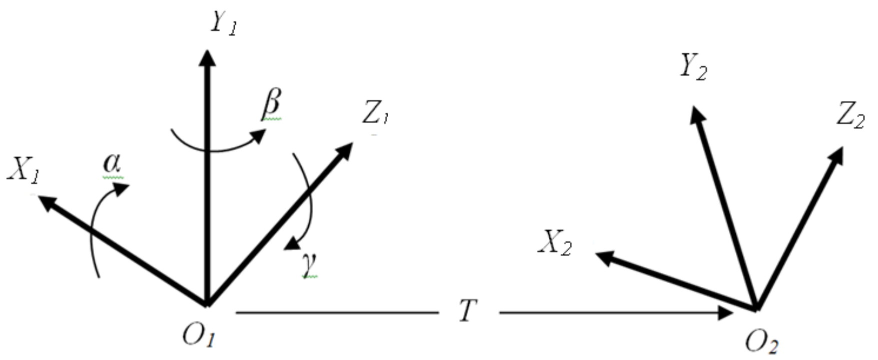

Alpha	(°)	20.6
Beta	(°)	-0.8
Gamma	(°)	-0.6
Tx	(mm)	6.8
Ty	(mm)	223.7
Tz	(mm)	41.9

2.6 MEASUREMENT PERFORMANCE

To obtain baseline data regarding the quality (bias and variability) of the measurements, a set of 7 stationary images are acquired and analyzed before the onset of the impact experiments. Displacement, strain, and full-field acceleration are computed for each image. Average values and standard deviation of the full-field data are calculated and used to establish baseline measurement metrics.

Figure 2.4 shows the standard deviation and the mean obtained for different variables. The mean value of axial displacement for each image is obtained by averaging all axial displacements in each image. The standard deviation for each image is obtained by subtracting the mean value from each measurement and a typical equation for defining standard deviation. A similar process is used for determining the mean and standard deviation in axial strain for each image, where the axial strain at a point is determined using Vic-3D algorithms noted previously. The acceleration results for mean and standard deviation are obtained for each image using a 3-term central finite difference formula with the measured full-field displacement data. The presence of small, non-zero mean values in displacement (Figure 2.4a) is noted. However, since the mean value is within the noise of the measurements, the significance of the slight offset is uncertain. As shown in Figures 3.4b and 2.4c, there is variability in both the acceleration and strain fields, with the mean values well within the standard deviation range. The standard deviation in strain is on the order of 100 με, which is typical for strain measurements in modern digital camera systems. It has been documented that the value of this noise can be significantly reduced by applying appropriate smoothing schemes [29]. However, no data smoothing is performed in the present work, and the results shown hereafter are those obtained directly from image correlation with no smoothing applied. Regarding the noise in the acceleration field, the values shown are consistent with variability in the displacement field and are magnified due to the 10 μs temporal step size used for image acquisition in the experiments.

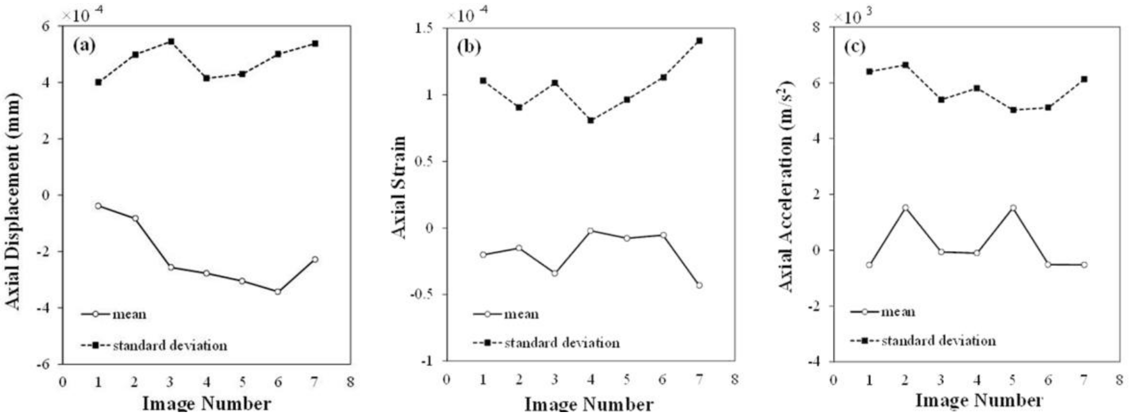

Figure 2.4 Mean and standard deviation of (a) axial displacement, (b) axial strain and (c) axial acceleration.

2.7 MODELING OF MATERIAL COMPRESSIBILITY

The polymeric foam specimens examined in this work are compressible, and hence their density varies when subjected to deformation [30]. To take the material compressibility into account, a simple one-dimensional model was proposed in this work, which facilitates the calculation of material's instantaneous density, as a function of its initial density and the applied strain components.

Let us consider a compressible cylindrical specimen of initial volume Ω_0 and initial density ρ_0, exposed to axial compression from one side. The specimen is then deformed into a cylinder of volume Ω, and density ρ at time t, as schematically shown in Figure 2.5. The temporal rate of change of the specimen volume, $\dot{\Omega}$, can be written as:

$$\frac{\dot{\Omega}}{\Omega} = 2\frac{\dot{r}}{r} + \frac{\dot{h}}{h} \tag{2.1}$$

where $\dot{r}$ and $\dot{h}$ are the temporal rate of change of radius and height of the cylindrical specimen, respectively. Assuming logarithmic strain metrics for both the radial and axial strain components, and the apparent Poisson's ratio as υ, the strain rate equations can be written;

$$\dot{\varepsilon}_r = \frac{\dot{r}}{r} \quad , \quad \dot{\varepsilon}_z = \frac{\dot{h}}{h} \tag{2.2a}$$

$$\dot{\varepsilon}_r = -\upsilon \dot{\varepsilon}_z \tag{2.2b}$$

Thus, Eq. (2.1) can be written in the following form;

$$\frac{\dot{\Omega}}{\Omega} = (1 - 2\upsilon)\ \dot{\varepsilon}_z \tag{2.3}$$

Eq. (2.3) can be further simplified by defining the instantaneous axial strain rate as [31]:

$$\dot{\varepsilon}_z = -\frac{V}{h} \tag{2.4}$$

where V is the magnitude of the velocity of the specimen at the impacted surface and h denotes the instantaneous specimen height, as shown schematically in Figure 2.5. Using Eqs. (2.3) and (2.4), the rate of change of the specimen volume can be rewritten in terms of the Poisson's ratio and the impacted end velocity, as:

$$\frac{\dot{\Omega}}{\Omega} = (2\upsilon - 1)\frac{V}{h} \tag{2.5}$$

Now, by considering the principle of conservation of mass for the compressible cylindrical specimen shown in Figure 2.4, the rate of change in density can be written as:

$$\dot{\rho} = -\left(\frac{\dot{\Omega}}{\Omega}\right)\rho \tag{2.6}$$

Assuming that the density, ρ, varies only along the z-direction and applying a simple mathematical chain rule, Eq. (2.6) can be rewritten as:

$$\frac{d\rho}{dh} \cdot \frac{dh}{dt} = -\left(\frac{\dot{\Omega}}{\Omega}\right)\rho \tag{2.7}$$

where by defining $dh/dt = -V$ and upon rearrangement, the final ordinary differential equation can be obtained as:

$$\frac{d\rho}{\rho} = (2\upsilon - 1)\frac{dh}{h} \tag{2.8}$$

Eq. (2.8) can be integrated to yield:

$$\rho = \rho_0 \left(\frac{h}{H}\right)^{2\upsilon - 1} \tag{2.9}$$

Eq. (2.9) can also be written in terms of the axial strain, $\varepsilon_z = \ln(h/H)$, as:

$$\rho = \rho_0 \left[\exp(\varepsilon_z)\right]^{2\upsilon - 1} \tag{2.10}$$

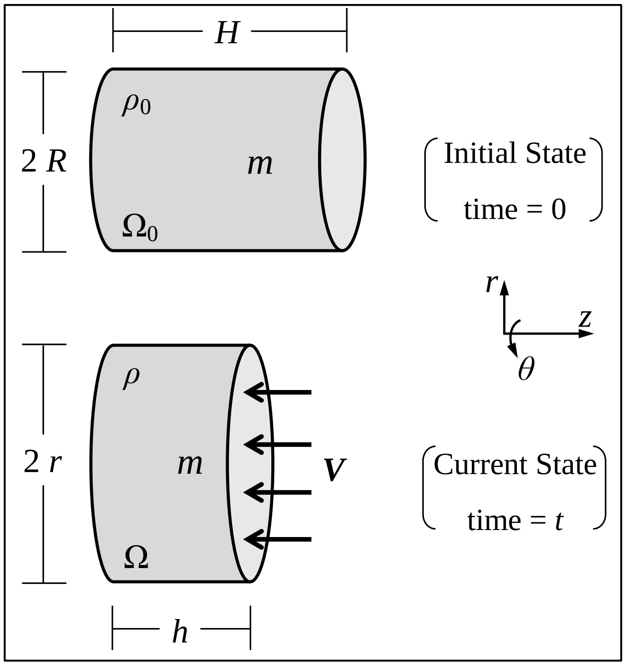

Figure 2.5 Schematic view of a compressible cylindrical specimen subjected to axial loading.

The significance of Eqs. (2.9) and (2.10) is that the variables *h*, ε_z and υ can be experimentally measured using digital image correlation at any given point along the specimen axis. The Poisson's ratio, υ, can be measured for a cylindrical specimen as the ratio between the radial and axial strain components. In this work, to measure the local evolution of υ, a cylindrical coordinate system was first assigned to the initial geometry of the specimen. Then, by tracking the evolution of the radial displacement component during the entire time of deformation, the radial strain component was determined. Note that by implementation of a cylindrical coordinate system, the radial strain component can be measured directly from the growth in the radius of the specimen, at any given time and any location on the surface. This 'growth in radius' will be independent of the amount of out-of-plane motion. Indeed, this is valid assuming that the radial strain values remain constant through the thickness the specimen, and that a circular section in the material remains circle during the deformation. On the other hand, the out-of-plane displacement in a Cartesian coordinate system contains both deformation and rigid body motion components, which cannot be readily separated when surface measurement is conducted. Therefore, if the radial expansion was to be measured from the out-of-plane displacement in a Cartesian system, significant error would have been introduced into the analysis. The change of coordinate system from Cartesian to cylindrical in this work was performed using the built-in 'coordinate' tool in Vic-3D. Accordingly, the Poisson's ratio was calculated at different locations along the axis of the specimen. Finally, it should be noticed that the mathematical expression shown in Eq. (2.10) predicts perfect incompressibility when $\upsilon = 0.5$, i.e. the condition existing in the classical incompressible plasticity.

2.8 DYNAMIC STRESS-STRAIN RESPONSE BY A NON-PARAMETRIC METHOD

In order to include the effects of inertia force and stress in the measurements in this work, a non-parametric analysis was performed in which the inertia stress within the specimen was reconstructed using the full-field deformation response.

Consider a cylindrical specimen, as schematically shown in Figure 2.6, subjected to direct impact loading on its right end, exerted by a projectile. The load-cell is located at the opposite side of the specimen. Let Ω be the current domain of interest. Each point inside the domain is represented by a position vector $\underline{z}=z_1\underline{e}_1+z_2\underline{e}_2+z_3\underline{e}_3$ in the domain. The force applied at any given position along the specimen axis $\underline{z}$ and at time t can be expressed as:

$$\underline{F}(\underline{z},t)=F_z(z_1,t)\underline{e}_1 \tag{2.11}$$

Considering the free body diagram of the sliced section in Figure 2.6 and applying Newton’s law of motion in axial direction, the following equation can be written:

$$F_z(z_1+dz,t)-F_z(z_1,t)=\rho(z_1,t)A(z_1,t)\,dz\,\frac{\partial^2 u_z}{\partial t^2}(z_1,t) \tag{2.12}$$

where $\rho(z_1,t)$ and $A(z_1,t)$ are specimen density and cross sectional area at position z_1 and time t, respectively. $u_z(z_1,t)$ represents the displacement component along the axial direction. Note that the F_z values in Eq. (2.12) are algebraic quantities. Eq. (2.12) can be rewritten in differential from as:

$$\frac{\partial F_z}{\partial z}(z_1,t)=\rho(z_1,t)A(z_1,t)\frac{\partial^2 u_z}{\partial t^2}(z_1,t) \tag{2.13}$$

which upon integration yields:

$$F_z(z_1,t)=F_z(0,t)+\int_{\xi=0}^{\xi=z_1}\rho(\xi,t)A(\xi,t)\frac{\partial^2 u_z}{\partial t^2}(\xi,t)\,d\xi \tag{2.14}$$

Eq. (2.14) was previously proposed by Othman et al. [5] and Aloui et al. [6]. This equation indicates that the force at any position can be reconstructed from the force at position $z = z_1$, i.e. at the location of the load-cells, along with the acceleration and density at position $z = 0$. The acceleration component at any given position along the z-direction can also be calculated from the displacement field obtained from DIC. In this work, a central difference scheme was utilized to numerically calculate the full-field acceleration distribution within the deforming specimen. Accordingly, the acceleration component was calculated as:

$$a_z(z_1,t) = \frac{1}{\Delta t^2}\left[u_z(z_1,t-\Delta t) - 2u_z(z_1,t) + u_z(z_1,t+\Delta t)\right] \tag{2.15}$$

where Δt denotes the time interval between two consecutive images, i.e. Δt =1/(frame rate). Similar to Eq. (2.14), the stress component in z-direction can be recovered as:

$$\sigma_z(z_1,t) = \frac{F_z(0,t)}{A(z_1,t)} + \int_{\xi=0}^{\xi=z_1} \rho(\xi,t)\frac{\partial^2 u_z}{\partial t^2}(\xi,t)\,d\xi \tag{2.16}$$

The stress component $\sigma_z(z_1,t)$ can be reconstructed from the stress magnitude measured at the load-cell side plus the inertia stress shown in integral term in Eq. (2.16).

Note that true stress value at any given position across the domain of interest can be calculated only if the current cross sectional area at the same position is identified. As described in the previous section, the change of the cross section of the cylindrical specimen can be measured directly from DIC. In this case also, a cylindrical coordinate system can be assigned on the initial configuration to facilitate measuring of the current dimensions of the cylindrical specimen at any given position in space and time. By including compressibility of the foam into the analysis, the final closed form equation that can be used to reconstruct the axial stress at any given position across the domain of interest can be written as:

$$\sigma_z(z_1,t) = \frac{F_z(0,t)}{A(z_1,t)} + \int_{\xi=0}^{\xi=z_1} \rho_0 \left[\exp(\varepsilon_z(\xi,t))^{2\upsilon(\xi,t)-1}\right] \frac{\partial^2 u_z}{\partial t^2}(\xi,t)\, d\xi \tag{2.17}$$

Assuming that the deformation of the specimens is only axial, to calculate the stress using the full-field data extracted from DIC and Eq. (2.17), the cylindrical geometry of the specimen is sliced into a finite number of thin sections of thickness *s* along the specimen length. Then, density and acceleration values within each section are calculated by averaging these parameters over the volume of each thin sliced section. Now, the integral term on the right hand side of Eq. (2.16) can be approximated as:

$$\int_{\xi=0}^{\xi=z_1} \rho(\xi,t) \frac{\partial^2 u_z}{\partial t^2}(\xi,t) d\xi \approx \sum_{i=1}^{n} \rho^{(i)} a^{(i)} s^{(i)} \tag{2.18}$$

where $\rho^{(\mathrm{i})}$ and $a^{(\mathrm{i})}$ are the average density and axial acceleration over the *i*th slice., respectively. $s^{(\mathrm{i})}$ represents the slice thickness, and *n* denotes the total number of sliced sections up to the location of z_1 (see Figure 2.7). In this work, the entire region of interest was sectioned into 24 thin slices of about 1 mm thick, each containing 36 data points. Thus, the averaging has been conducted on a population of 36 data points in each slice.

It should be emphasized that the compressibility model proposed in this work, i.e. Eq. (2.10), assumes homogeneous deformation condition. However, Eq. (2.10) can be used in the case of heterogeneous deformation condition, assuming that each individual slice undergoes a rather homogeneous deformation.

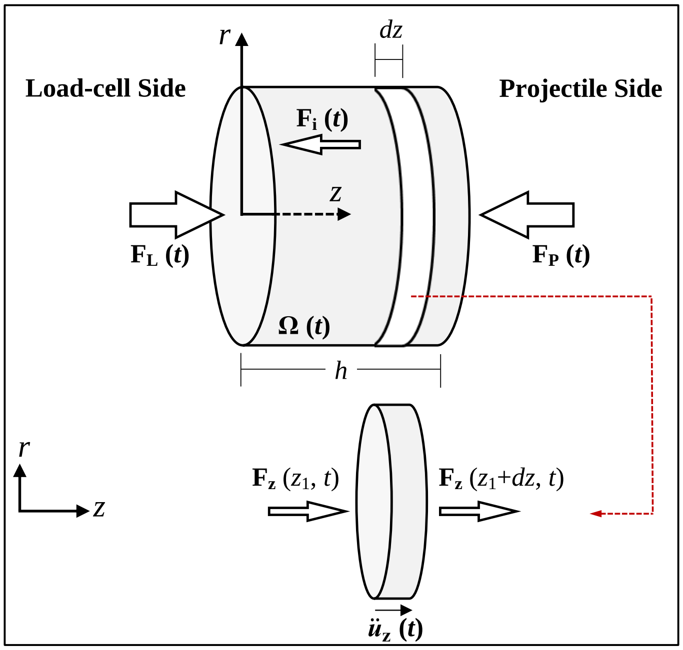

Figure 2.6 Schematic of a cylindrical specimen subjected to direct impact. The dynamic load is applied on the specimen from the projectile side.

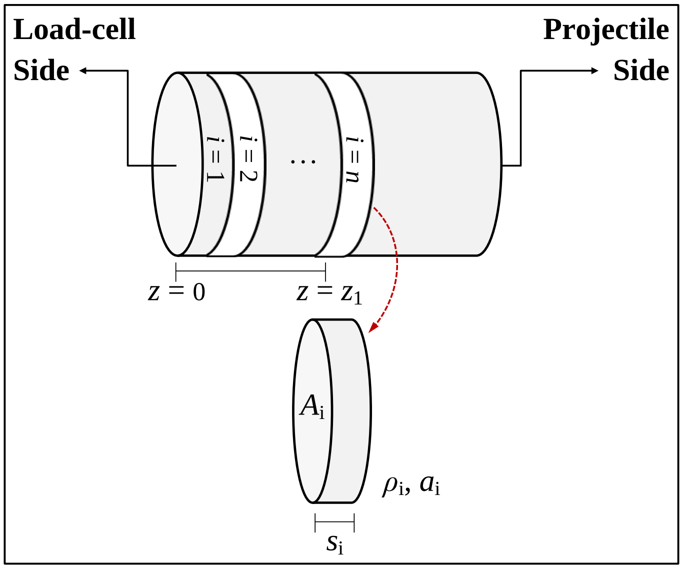

Figure 2.7 Schematic geometry of the specimen sliced into a finite number of thinner segments, used to calculate the inertia force and stress applied at each point along the specimen axis.

2.9 RESULTS AND DISCUSSION

Figure 2.8 shows the force measured at the load-cell side of the specimen for two independent experiments performed using one Mylar sheet. Consistent results shown here confirm the repeatability of the experimental results in this work.

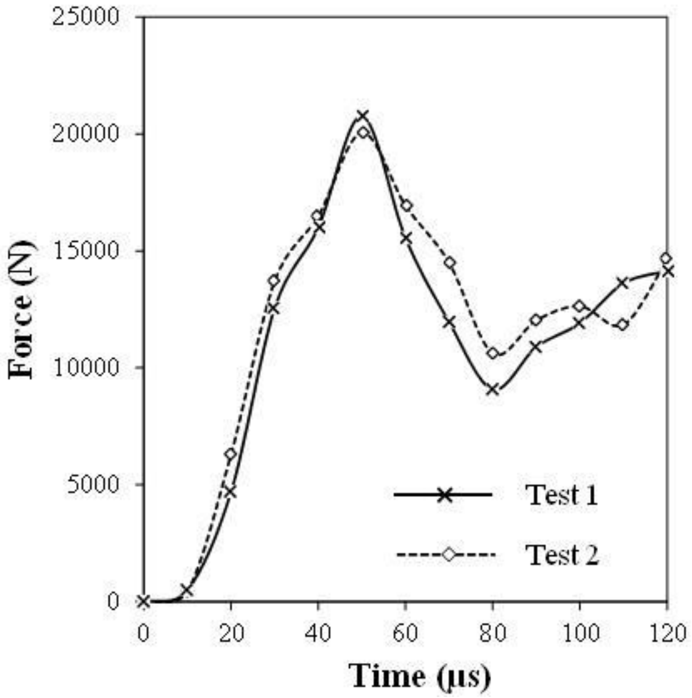

Figure 2.8 Load-cell response for two independent experiments performed using one Mylar sheet.

The velocity of the projectile can be varied by changing the thickness and/or the number of diaphragms separating the driver and driven sections of the shock tube. Projectile velocity in this work was calculated by differentiating the projectile displacement with respect to time. Projectile displacement was measured by tracking the motion of a single pixel, located at the tip of the projectile, in time. Thus, the projectile velocity measurements in this work are of pixel accuracy level. Displacement of the tip of the projectile with respect to time is shown in Figure 2.9. The projectile velocity was shown to remain constant well after incidence with the specimen. In addition, experimental data indicate that the average projectile velocity increased by 35% when the number of Mylar diaphragms was increased from one to two.

Two different strain rates were applied on the specimens in this work, associated with one and two Mylar sheets used to separate the driver and the driven sections of the shock tube. To calculate the average strain rate applied to the specimen, the axial strain magnitudes over the entire domain of interest were averaged and plotted as a function of deformation time, as shown in Figure 2.10. The slopes of the best linear fits were then considered as the average strain rate in each case. The average strain rates obtained through this procedure are 1437 s^{-1} and 2458 s^{-1} corresponding to one and two Mylar sheets, respectively. The error bars indicate standard deviation of the full-field strain data, which can be considered as a measure of the inhomogeneity of the strain field at any given time during deformation. Considering the strain history curves shown in Figure 2.10, the level of inhomogeneity of axial strain is observed to be higher in higher strain rate condition. Furthermore, the strain inhomogeneity is found to be higher at earlier stages of deformation, i.e. the time during which equilibrium has not yet achieved. The heterogeneous distribution of strain in earlier stages of deformation yields in the strain rates to be highly heterogeneous, as well. In materials with strong rate sensitivity, such as the one examined in this work, the heterogeneous strain rate field might result in a spatial variation of stress-strain response over the gage area.

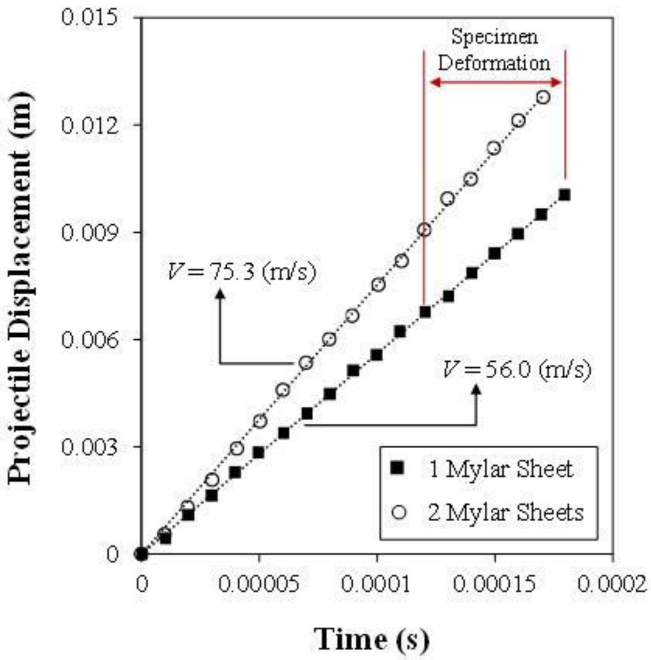

Figure 2.9 Variation of the projectile displacement with time. Increasing the number of plastic diaphragms from one to two has resulted in a 35% increase in the velocity of the projectile.

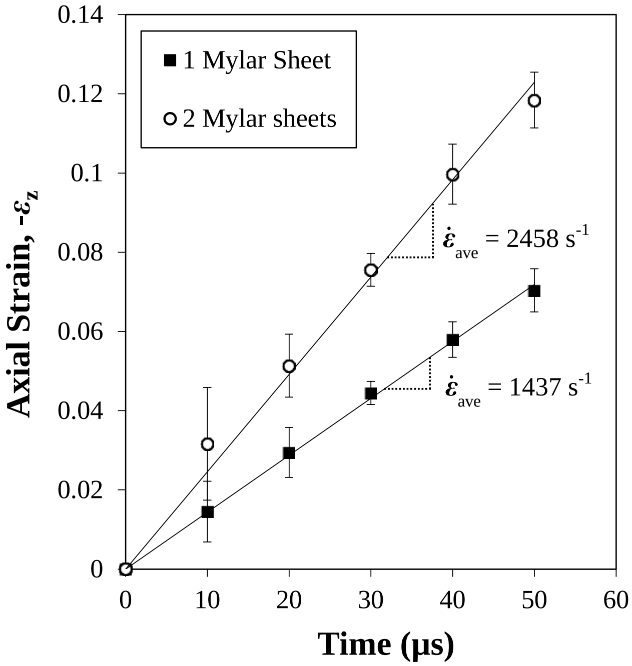

Figure 2.10 Evolution of the average axial strain applied on the specimen as a functions of time, for two different number of Mylar sheets.

Figure 2.11 shows the variation of average axial and radial strains per slice, at different positions along the specimen axis and at various times. Strain heterogeneity along the specimen axis is clearly observed in both sets of curves. It is also seen that at earlier deformation times, both axial and radial strains take significantly larger values at the impacted side of the specimen ($\bar{z}=1$); while, at longer durations, this behavior is reversed and the load-cell side ($\bar{z}=0$) undergoes larger strains. In addition, the radial strain heterogeneity seems higher compared with the axial strain component. This might be due to the frictional state and boundary conditions at specimen ends which partially restrain the lateral expansion of the specimen within areas closer to specimen ends.

Using the obtained radial and axial strain distributions, evolution of the Poisson's ratio in the region of interest was also determined. Contours showing the evolution of Poisson's ratio for the specimen deformed under the higher strain rate conditions have been depicted in Figure 2.12. The evolution of υ at three different locations along the specimen axis has also been plotted in Figure 2.13, for both strain rate conditions. The calculated Poisson's ratios indicate maximum values at t = 20 μs for both strain rate conditions. This could be associated with the boundary condition and strain heterogeneity at early stage of loading. During early deformation stage, the specimen is relatively free to deform laterally. As the loading progress the friction and boundary conditions at the specimen ends could restrain the radial deformation to some extent. Therefore, the rate of change of lateral strain with respect to that of axial strain significantly increases during the first 20 μs after the impact, thus resulting in larger Poisson's ratios at t = 20 μs. In addition, larger Poisson's ratio values were obtained for the specimen deformed under lower strain rate conditions, indicating that the foam specimens examined in this work experience a larger compressibility at higher strain rate (see Eq. (2.10)). It should be emphasized here that no conclusive information can be extracted on the rate sensitivity of the Poisson’s ratio of the specimens in this work. The evolution of Poisson’s ratio for specimens deformed under different strain rates was considered only to facilitate the application of the proposed compressibility model.

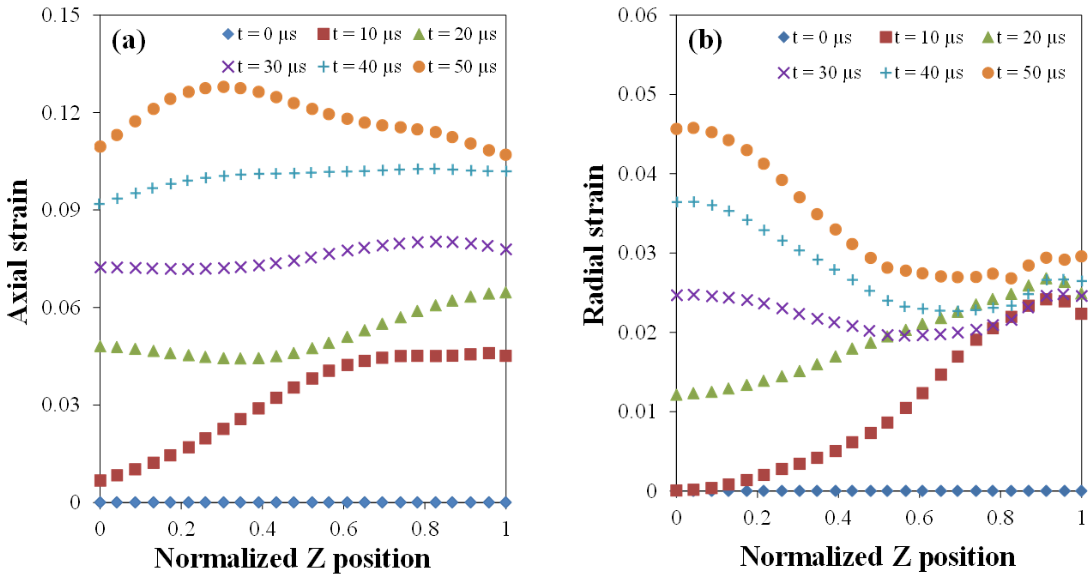

Figure 2.11 Variation of average (a) axial and (b) radial strains per slice, at different locations and times. $\bar{z}=0$ indicates the load-cell side.

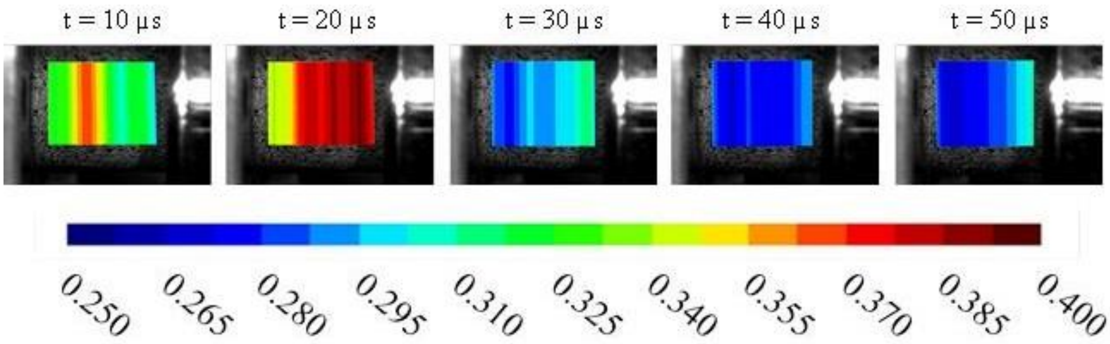

Figure 2.12 Full-field distribution of Poisson’s ratio, υ, for the specimen subjected to direct impact with two Mylar sheets.

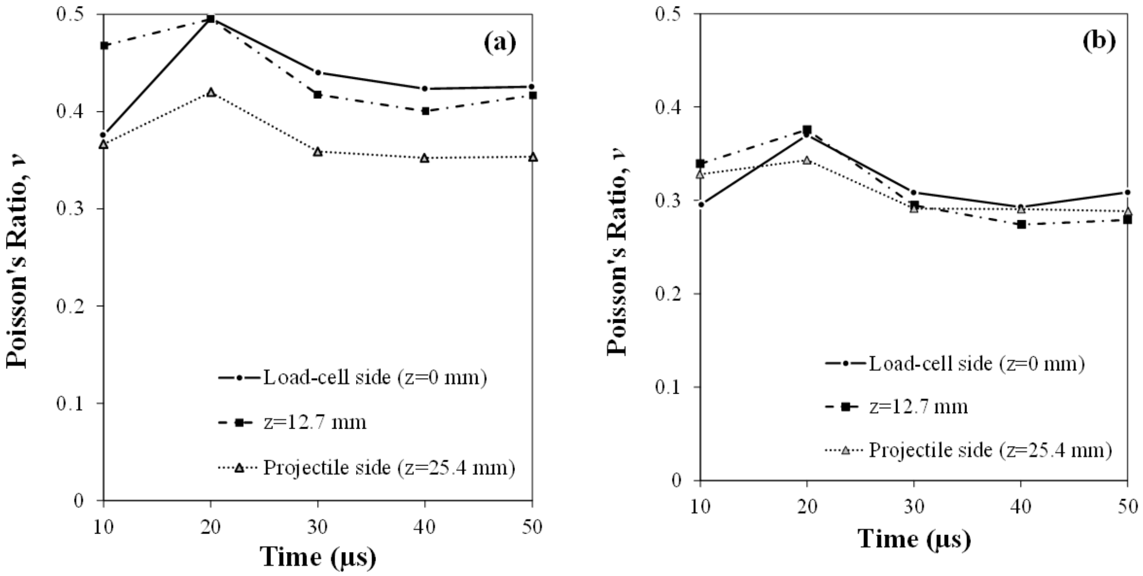

Figure 2.13 Local Poisson's ratio, υ, of the specimens extracted from different positions along the axis of foam specimens deformed at (a) 1437 s^{-1} and (b) 2458 s^{-1} strain rates.

The local change of density of the specimens at different strain rate conditions can be determined once the evolution of the Poisson ratio, υ, is obtained. Figure 2.14 illustrates the typical form obtained for the local change of density of the specimens at three different locations along the specimen axis. For the case of lower strain rate condition, the foam specimen shows less compressibility with a negligible (~2%) change of density (see Figure 2.14a). However, the density of the specimen changes more noticeably under higher strain rate conditions (>5%), as υ deviates from a perfect incompressible condition, i.e. υ = 0.5. Considering these results, it is important to include the material change of density in the calculation of inertia forces and stresses, to increase the accuracy of the predictions. Note that the change of density calculated for materials considered in this work are relatively small. However, the proposed model can be used for any compressible solid, regardless of the degree of compressibility

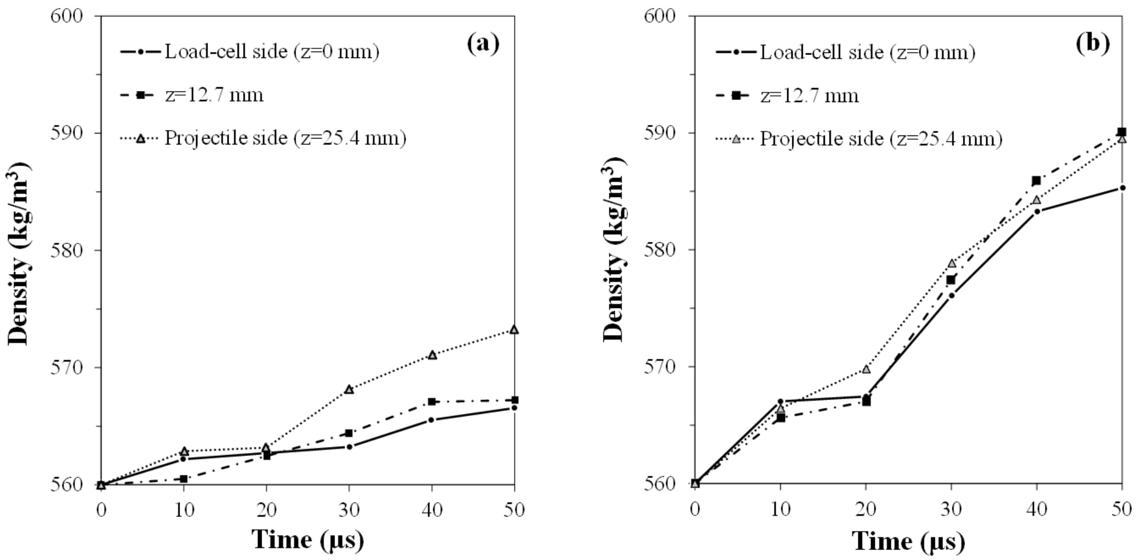

Figure 2.14 Variation of local density as a function of deformation time, extracted from different positions along the axis of foam specimens deformed at (a) 1437 s^{-1} and (b) 2458 s^{-1} strain rates.

Full-field acceleration distribution was calculated based on the procedure described in earlier sections. Full-field axial displacement and acceleration maps at each time step are shown in Figure 2.15 for the specimen subjected to higher strain rate conditions. Figure 2.15a shows a rather circumferentially-homogeneous distribution of the axial displacement. Relatively uniform distribution of acceleration in hoop direction is also evident in Figure 2.15b. However, both displacement and acceleration contour maps indicate strong axial gradients. This is shown in the highly nonhomogeneous distribution of acceleration along the axis of the specimen, particularly in the earlier stages of deformation, i.e. $0 < t < 20$ μs (see Figure 2.15b). The axial acceleration then becomes smaller in magnitude and more homogeneous at longer durations, as shown in Figure 2.16, where the axial acceleration component was averaged over the entire domain of interest and plotted at each deformation time step. Error bars in Figure 2.16 indicate standard deviation of the full-field acceleration data. For both strain rate conditions, a sudden change in the magnitude of the average acceleration takes place after 10 μs of loading. Though, the limitation of the temporal resolution (10 μs) of the experiment makes it difficult to track the trend of the acceleration, it clear that the acceleration decreases as a function of time as shown in Figure 2.16.

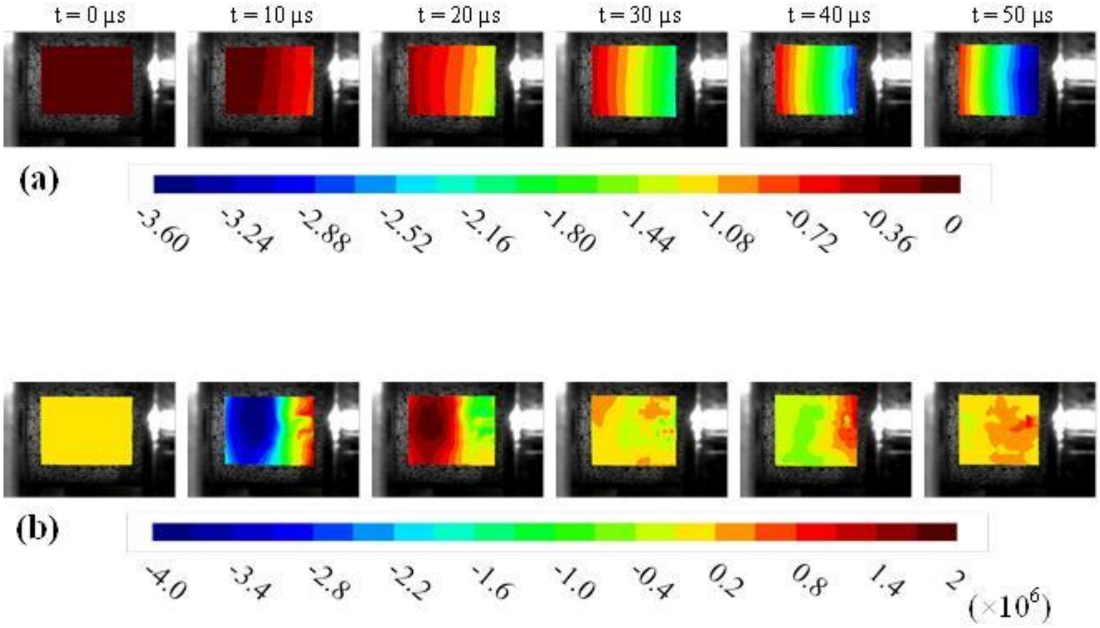

Figure 2.15 Full-field distributions of (a) axial displacement (mm) and (b) axial acceleration (m/s^2) for the specimen subjected to higher strain rate conditions.

The large value of acceleration obtained in early stages of deformation results in a significant increase of inertia force and inertia stress (see Eqs. (2.14) to (2.17)) at earlier deformation times, as also reported previously in [5]. Note that the accuracy of the acceleration field highly depends on the temporal resolution of the measurements, i.e. the frame rate. A low frame rate can filter out the calculated acceleration, resulting in the inertia stresses to be smeared out; whereas a high framing rate may amplify noise in the acceleration curves. Due to limitation of the temporal resolution of our camera, parametric studies on the framing rate and acceleration noise level have not been conducted. The accuracy of the acceleration fields determined in this work may have deteriorated due to relatively low framing rate of the available camera system. However, the concept of the study of concurrent influences of inertia and compressibility remain valid as long as the methodology detailed in this work is followed.

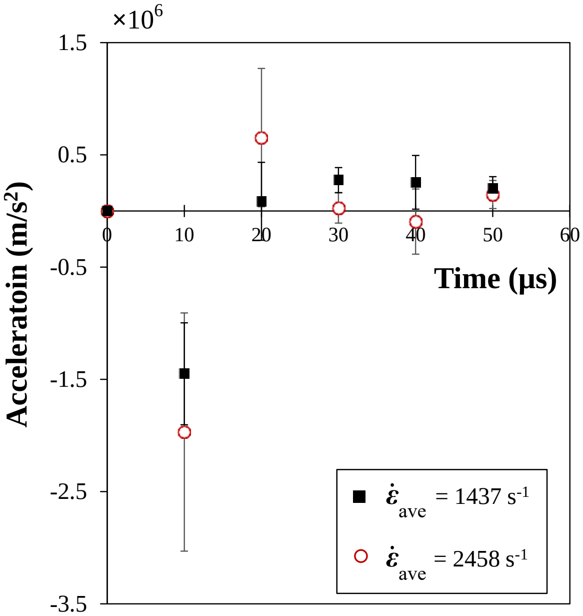

Figure 2.16 Variation of the axial acceleration averaged over the entire domain of interest with respect to time.

Having obtained all the required parameters, the values of force and stress can be reconstructed at any given position along the specimen axis, following the procedure detailed earlier. The force applied on the load-cell side of the specimen can be directly measured from the load-cells inserted behind the specimen. However, the force applied on the other side, i.e. the projectile side, is required to be reconstructed using the load measured on the load-cell side along with the acceleration and density fields obtained earlier. The forces acting on two sides of the foam specimens are plotted in Figure 2.17.

In both strain rate conditions, the load measured on the load-cell side exhibits a very slight rate of change during the first 10 μs of the deformation. This can be attributed to the low wave propagation speed in the specimen. Note that due to the low impedance of the foam specimens examined here, there would be an elapsed time between the instant at which the projectile hits the specimen and the time at which the compressive wave reaches the other end of the specimen, i.e. the location of the load-cells. Therefore, the load-cells are not capable of recording the load exerted on the specimen during the early stages of deformation. During this early time period, the force applied on the projectile side of the specimen is significantly larger, resulting in significant deformation within the specimen, particularly within the regions close to the projectile (see Figure 2.11). This non-equilibrium state gradually diminishes after t = 20 μs, resulting in the load magnitudes on the load-cell and projectile sides of the specimen to become more equilibrated.

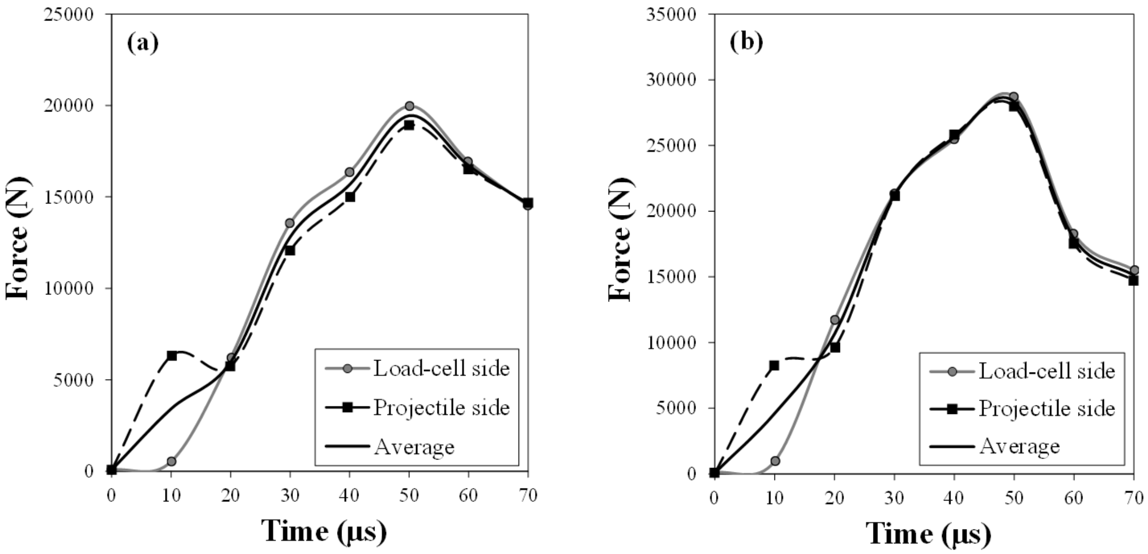

Figure 2.17 Forces applied on the load-cell and projectile sides of the specimen for specimens deformed under (a) 1437 s^{-1} and (b) 2458 s^{-1} strain rate.

The non-equilibrium state of deformation that occurs during the early stages of impact can be studied through the stress-strain response of the specimen. Full-field axial strain and stress contour maps for the specimen subjected to 2458 s^{-1} strain rate are plotted in Figure 2.18. In this case also, the strain maps were obtained by slicing the specimen geometry into 24 thinner sections and averaging the strain values over each and every sliced section. The full-field strain data utilized for this purpose were those directly measured from DIC. Using the previously obtained full-field acceleration and applying Eq. (2.18), the stress distribution was also obtained along the axis of the specimen. The stress-strain responses of the specimens are very similar to those described previously for the load history. The full-field contour maps shown in Figure 2.18 exhibit a highly non-homogeneous distribution of strain and stress during the first 20 µs of the deformation. For t > 20µs, the level of inhomogeneity in the deformation is substantially reduced and the specimen approaches equilibrium in the deformation state.

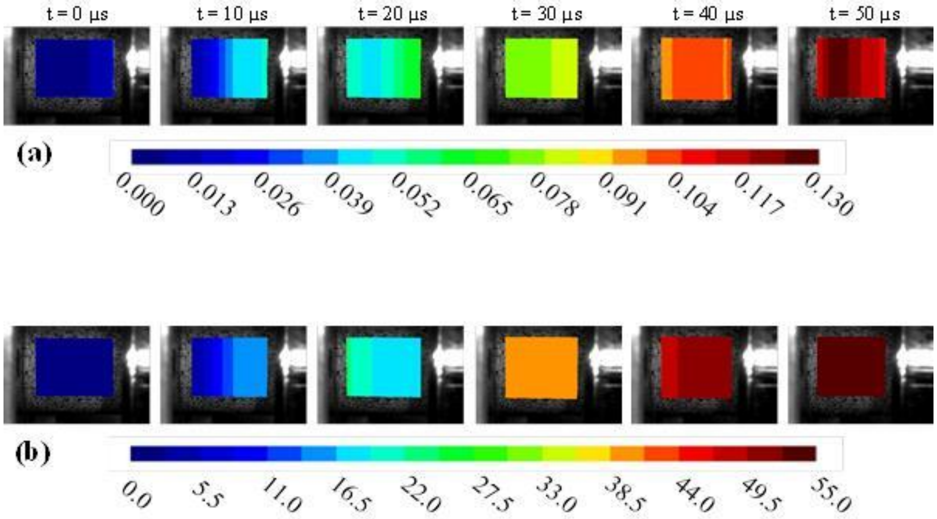

Figure 2.18 Full-field distributions of (a) axial strain and (b) axial stress (MPa) components for the specimen subjected to 2458 s^{-1} strain rate. Note that the strains and stresses are compressive in nature, but the values reported in here are the absolute values.

The significance of using the methodology outlined above is that the stress and strain histories within the material at any given position along its axis can be calculated and studied, even when “quasi-static equilibrium” conditions typically employed are not present. For instance, the evolution of strains and stresses extracted from different locations along the specimen axis are plotted in Figures 2.19 and 2.20, respectively. Similar to the load curves, remarkable differences between the local curves for both local strain and local stress responses shown in Figures 2.19 and 2.20 are evident when $t < 20\mu s$. Considering the local stress curves shown in Figure 2.20, one can notice that the large variation in local stress and local strain lasts for about 25 µs, the time required for the wave to propagate through the specimen. All local stress curves are then expected to collapse to the same curve, as shown in Figures 2.20a and 2.20b, until the failure of the specimen. However, there exists a systematic offset between the curves even after $t = 25$ µs, and this can be attributed to the spurious acceleration behavior shown and discussed earlier in Figure 2.16. Note that the low temporal resolution of the measurements in this work results in interframe times of the order of the wave propagation time. This means that the acceleration, at least in the early stages of deformation, might have been underestimated. The low accuracy of the acceleration measurements can generate a systematic error on the stress-strain curves, as well. One way to address this issue would be to simulate the measurements using, for instance, the procedure proposed in [32, 33]. This is beyond the scope of the present work, but must be accounted for in highly accurate analyses of the low impedance materials.

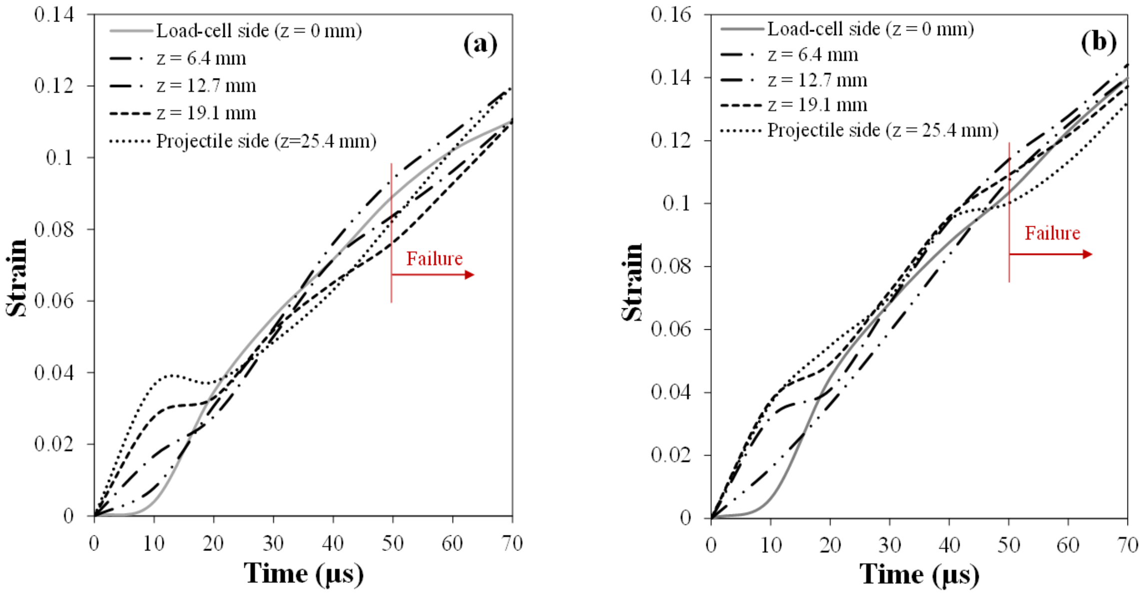

Figure 2.19 Local strain evolutions extracted from different positions along the specimen axis for the foam specimens deformed at (a) 1437 s^{-1} and (b) 2458 s^{-1} strain rates.

Next, using the strain-time and stress-time curves obtained and shown earlier in Figures 2.19 and 2.20, local stress-strain curves were determined. Local stress-strain curves for both strain rate conditions have been illustrated in Figure 2.21, where good agreement between each set of curves is indicated. Finally, the local stress-strain curves obtained at different positions along the specimen axis were averaged and the resultant average curves were compared with the stress-strain response conventionally determined using the specimen-end force measurement. Note that in the conventional methodology, the strain was obtained by averaging the axial strain magnitudes, obtained directly from DIC, over the entire field of view. Consequently, only one strain value at each point of time is obtained in this method. Figure 2.22 compares the stress-strain curves using two methods, i.e. non-parametric analysis and the conventional method. It is clearly observed that by using the conventional methodology substantial error can be imposed on the results, making this method ineffective for the case of low impedance polymeric foams.

In particular, the highest discrepancy between the curves is evident at earlier stages of deformation, as discussed in detail earlier.

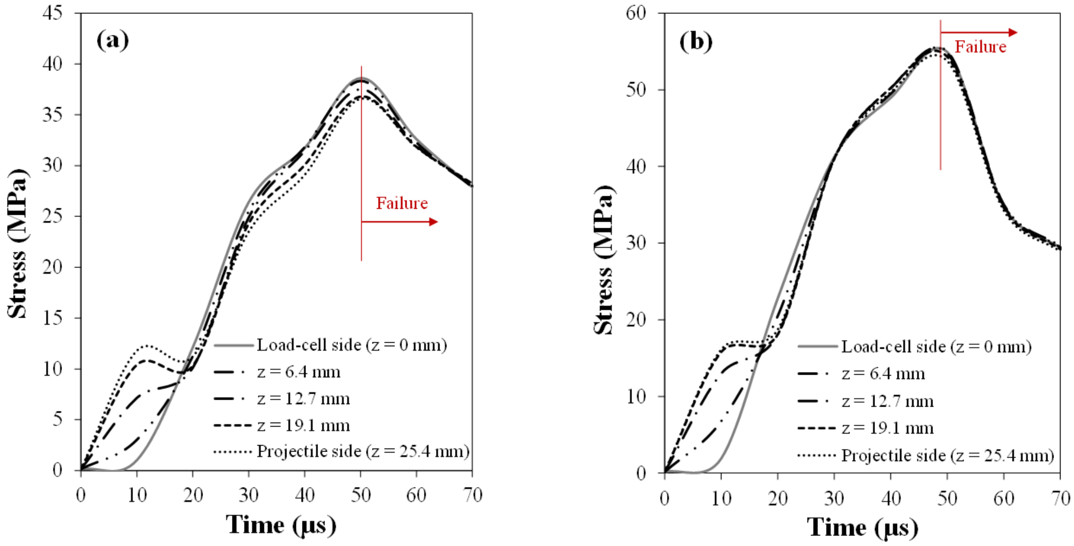

Figure 2.20 Evolution of local stress at different positions along the specimen axis for the foam specimens deformed at (a) 1437 s^{-1} and (b) 2458 s^{-1} strain rates.

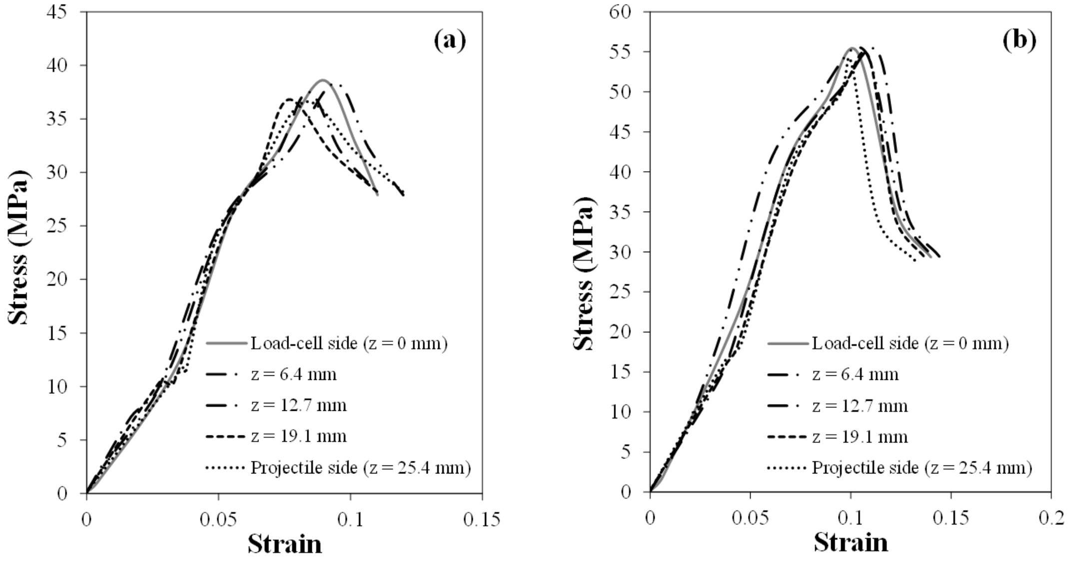

Figure 2.21 Local stress-strain curves obtained at different positions along the specimen axis for the foam specimens deformed at (a) 1437 s^{-1} and (b) 2458 s^{-1} strain rates.

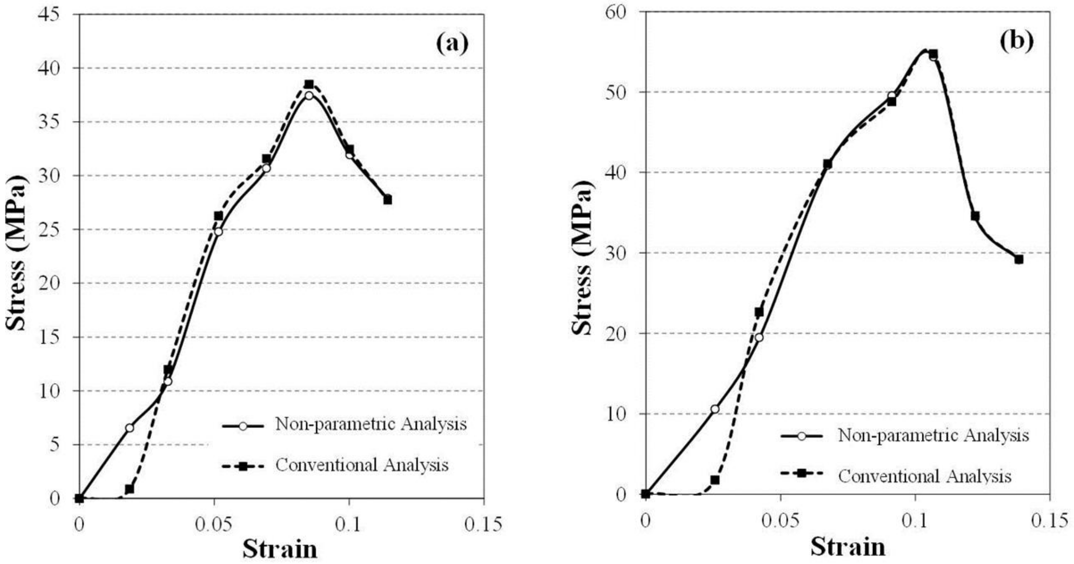

Figure 2.22 Global stress-strain curves obtained using two different methods for foam specimens deformed at (a) 1437 s^{-1} and (b) 2458 s^{-1} strain rates.

Finally, it is worth noting that the analysis performed in this work allows the measurement of the elastic modulus of viscoelastic materials at high strain rate conditions. Accordingly, the elastic modulus of the examined foam was estimated as 352 MPa and 411 MPa at 1437 s^{-1} and 2458 s^{-1} strain rates, respectively. Indeed, due to the low temporal resolution of the measurements in the present work, these values are estimates only. Clearly, the elastic properties of the examined material could have been estimated more accurately, in case higher resolution measurements were conducted. However, the authors believe that using the methodology described in this work, while taking advantage of ultra high speed photography, measurement of the elasto-viscoplastic properties of low-impedance materials can be facilitated.

2.10 CONCLUSIONS

The dynamic stress-strain response of closed-cell rigid polyurethane foam was investigated using high speed photography with 3D digital image correlation. Owing to the low wave propagation speed of the examined foam specimens, a highly non-homogeneous state of deformation was observed during impact loading, a condition that requires the inclusion of inertia stresses in the analysis. The change in density, inertia forces and stresses were first calculated using the full-field strain and acceleration distributions. By superimposing the locally developed inertia stresses to the stress magnitudes measured at specimen end, the full-field distribution of axial stress developed within the material was calculated. Considering the results obtained in this work, the following remarks should be noted:

- It has been well established in the literature, and was clearly demonstrated in the present work, that in the case of low impedance materials, conventional boundary measurements can introduce substantial error into the analysis.
- The method described in the present work took advantage of full-field 3D digital image correlation measurements throughout the transient loading process to include the effects of compressibility and inertia forces and to overcome the limitations associated with conventional boundary measurements. The main limitation in the present work was the temporal resolution of the DIC measurements. This issue can be resolved by using ultra high speed cameras commercially available today.
- Attempts were made to include the concurrent influences of material compressibility and inertia effect in the analyses. Although the material examined

here shows minimal change of density, the analysis can be applied to any low-impedance compressible solid, regardless of the degree of compressibility.

- The authors believe that following the procedure detailed in this work, it would be possible to carry out high strain rate experiments on low impedance and/or soft materials and extract accurate stress-strain relations, a concept that continues to be of great interest in the experimental mechanics' community.
- Clearly, the effort in this work was to demonstrate the applicability of the utilized method of analysis. The authors believe that using the methodology described in the present work, along with more powerful full-field measurement techniques and more advanced dynamic experiment apparatuses, the rate dependent elastic properties of materials, regardless of their high or low impedance characteristics, can be obtained. This would be basically achieved following the improvement of ultra-high speed imaging techniques in the near future.

2.11 LIST OF REFERNECES

[1] Field JE, Walley SM, Proud WG, Goldrein HT, Siviour CR. Review of experimental techniques for high rate deformation and shock studies. International Journal of Impact Engineering 2004; 30: 725-775.

[2] Hopkinson B. A method of measuring the pressure produced in the detonation of high explosives or by the impact of bullets. Philosophical Transactions of the Royal Society of London 1914; 213: 437-456.

[3] Song B, Chen W. Dynamic stress equilibrium in split Hopkinson pressure bar tests on soft materials. Experimental Mechanics 2004; 44: 300-312.

[4] Mallon S, Kidane A, Lu WY. Full-field deformation observation of polymer foam subjected to shock loading. In: Song B, Casem D, Kimberley J (Editors), Dynamic behavior of materials – Volume 1, Proceedings of the 2014 Annual Conference on Experimental and Applied Mechanics, Springer, 2015, pp 83-89. DOI 10.1007/978-3-319-06995-1_14

[5] Othman R, Aloui S, Poitou A. Identification of non-homogeneous stress fields in dynamic experiments with a non-parametric method. Polymer Testing 2010; 29: 616-623.

[6] Aloui S, Othman R, Poitou A, Guegan P, El-Borgi S. Non-parametric identification of the non-homogeneous stress in high strain-rate uni-axial experiments. Mechanical Research Communications 2008; 35: 392-397.

[7] Zhang X, Zhang H. Optimal design of functionally graded foam material under impact loading. International Journal of Mechanical Sciences 2013; 68: 199-211.

[8] Avalle M, Belingardi G, Montanini R. Characterization of polymeric structural foams under compressive impact loading by means of energy-absorption diagram. International Journal of Impact Engineering 2001; 25: 445-472.

[9] Ouellet S, Cronin DS, Moulton J, Petel EO. High rate characterization of polymeric closed-cell foams: Challenges related to size effects. In: Chalivendra V, Song B, Casem D (Editors), Dynamic behavior of materials – Volume 1, Proceedings of the 2012 Annual Conference on Experimental and Applied Mechanics, Springer, 2013, pp 21-28. DOI 10.1007/978-1-4614-4238-7_4

[10] Petel OE, Ouellet S, Frost DL, Higgins AJ. Shock Hugoniot measurements in foam. Journal of Physics: Conference Series 2014; 500: 1-6.

[11] Viot P, Beani F, Lataillade JL. Polymeric foam behavior under dynamic compressive loading. Journal of Materials Science 2005; 40: 5829-5837.

[12] Flores-Johnson EA, Li QM. Low velocity impact on polymeric foams. Journal of Cellular Plastics 2011; 47: 45-63.

[13] Linul E, Marsavina L, Voiconi T, Sadowski T. Study of factors influencing the mechanical properties of polyurethane foams under dynamic compression. Journal of Physics: Conference Series 2013; 451: 1-6.

[14] Ouellet S, Cronin D, Worswick M. Compressive response of polymeric foams under quasi-static, medium and high strain rate conditions. Polymer Testing 2006; 25: 731-743.

[15] Whisler D, Kim H. Experimental and simulated high strain dynamic loading of polyurethane foam. Polymer Testing 2015; 41: 219-230.

[16] Liu J, Saletti D, Pattofatto S, Zhao H. Impact testing of polymer foam using Hopkinson bars and digital image analysis. Polymer Testing 2014; 36: 101-109.

[17] Oullet S, Cronin D, Worswick M. Compressive response of polymeric foams under quasi-static, medium and high strain rate conditions. Polymer Testing 2006; 25: 731-743.

[18] Chen R, Huang S, Xia K, Lu F. A modified Hopkinson bar system for testing ultra-soft materials under intermediate strain rates. In: DYMAT-International Conference on the Mechanical and Physical Behaviour of Materials under Dynamic Loading, vol. 1, pp. 389-394. EDP Sciences, 2009. DOI: 10.1051/dymat/2009055

[19] M.A Sutton, J.J Orteu, H.W Schrier. Image correlation for shape, motion and deformation measurements. Springer. NY. 2009

[20] Pierron F, Zhu H, Siviour C. Beyond Hopkinson's bar. Philosophical Transactions of the Royal Society A 2014; 372: 20130195.

[21] Gilat A, Schmidt TE, Walker AL. Full field measurement in compression and tensile split Hopkinson bar experiments. Experimental Mechanics 2009; 49: 291-302.

[22] Koohbor B, Mallon S, Kidane A, Sutton MA. A DIC-based study of in-plane mechanical response and fracture of orthotropic carbon fiber reinforced composites. Composites Part B-Eng 2014; 66: 388-399.

[23] Mallon S, Koohbor B, Kidane A, Sutton MA. Fracture behavior of prestressed composites subjected to shock loading: A DIC-based study. Experimental Mechanics 2015; 55: 211-225.

[24] Pierron F, Forquin P. Ultra-high-speed full-field deformation measurements on concrete spalling specimens and stiffness identification with the virtual fields method. Strain 2012; 48: 388-405.

[25] Moulart R, Pierron F, Hallett SR, Wisnom MR. Full-field strain measurement and identification of composites moduli at high strain rate with the virtual fields methods. Experimental Mechanics 2011; 51: 509-536.

[26] Lu WY. Mechanical characterization of rigid polyurethane foams. Sandia Report 2014: SADN2014-20708.

[27] Mallon S, Koohbor B, Kidane A. Fracture of pre-stressed woven glass fiber composite exposed to shock loading. In: Song B, Casem D, Kimberley J (Editors), Dynamic behavior of materials – Volume 1, Proceedings of the 2014 Annual Conference on Experimental and Applied Mechanics, Springer, 2015, pp 213-219. DOI 10.1007/978-3-319-06995-1_32

[28] Koohbor B, Mallon S, Kidane A, Lu WY. The deformation and failure response of closed-cell PMDI foams subjected to dynamic impact loading. Polymer Testing 2015; 44: 112-124.

[29] Pierron F, Sutton MA, Tiwari V. Ultra high speed DIC and virtual fields method analysis of a three point bending impact test on an aluminum bar. Experimental Mechanics 2011; 51: 537-563.

[30] L.J Gibson, M.F Ashby. Cellular solids: Structure and properties. 2nd ed. Oxford. 1997

[31] Samanta SK. Dynamic deformation of aluminum and copper at elevated temperatures. Journal of Mechanics and Physics of Solids 1971; 19: 117.

[32] Lava P, Cooreman S, Coppieters S, De Strycker M, Debruyne D. Assessment of measuring errors in DIC using deformation fields generated by plastic FEA. Optics and Lasers in Engineering 2009; 47: 747-753.

[33] Rossi M, Lava P, Pierron F, Debruyne D, Sasso M. Effect of DIC resolution, noise and interpolation error on identification results with the VFM. Strain 2015; 51: 206-222.

CHAPTER 3

EFFECT OF SPECIMEN SIZE, COMPRESSIBILITY AND INERTIA ON THE RESPONSE OF RIGID POLYMER FOAMS SUBJECTED TO HIGH VELOCITY DIRECT IMPACT LOADING [2]

---

[2] Koohbor B, Kidane A, Lu W. Submitted to *International Journal of Impact Engineering*, 2016.

3.1 ABSTRACT

The influences of specimen length-to-diameter ratio, material compressibility, and inertia on direct impact response of high density closed-cell polymeric foam are investigated. High speed photography and stereovision digital image correlation are conducted to measure the full-field deformation response of the material subjected to direct impact. Inertia stress developed in the specimen is calculated from the acceleration distribution obtained from full-field measurements. Total axial stress magnitude along the axis of the specimen is then reconstructed from inertia and boundary-measured stresses. It is clearly shown that there is an appreciable degree of spatial variability in strains, strain rates and stresses developed in the impacted foam specimens, whereas the degree of such axial variability is more significant at higher length-to-diameter ratios. The study is further extended to take advantage of such spatial variability to identify the rate sensitivity of the examined material over a wide range of strain rates from 1000 s^{-1} to 5000 s^{-1}. The approach proposed here is shown to facilitate the identification of viscoplastic constitutive response of low impedance materials using a minimum number of tests.

3.2 INTRODUCTION

Rigid polymeric foams have gained extensive attention in several engineering applications that require excellent energy absorption with structural stability and significant weight reduction. Rigid polymer foams are widely used in applications such as cushioning, impact and crash mitigation, packaging, sandwich structures, etc., many of which entail high strain rate loading conditions [1]. Therefore, characterization of the mechanical response of foams under dynamic loading conditions has been an interesting subject of study for decades [2]. In this regard, several models have so far been proposed to characterize the phenomenological constitutive behavior of polymeric foams under large strain and various strain rate conditions [3-5].

From an experimental perspective, there are major challenges encountered during the study of deformation response of polymeric foams at high strain rate loading conditions [6]. The first and probably most important challenge is associated with the delayed stress equilibrium, which is due to the low mechanical impedance nature of these materials. There have been several solutions proposed to minimize the effect of such belated equilibrium conditions. For instance, application of polymeric bars [2, 7, 8] or hollow metallic transmission bar [9] in the split Hopkinson pressure bar (SHPB) experiments have been proposed with the purpose of reducing the impedance mismatch between the specimen and the bars, and hence to acquire more accurate transmitted signals. However, application of viscoelastic bars raises other challenges associated with wave propagation attenuation and dispersion due to the material rheological properties and the radial inertia stresses developed in the bars [10]. Different methods have been proposed and successfully practiced to correct the strain signals and restore the actual strain exerted at the interface of the specimen and the bars [11-15]. Pulse shaping technique has been established to provide an alternative solution in dynamic testing of low impedance materials. Application of pulse shaper has been established to ensure nearly constant strain rates, as well as the presence of dynamically equilibrated stress in the specimen [16, 17].

A more general solution to minimize the effects of non-equilibrium stress state in dynamic testing of low impedance materials is reducing the length of the sample. In general, wave reverberation period is significantly reduced in short specimens, resulting in a faster stress equilibration within the gauge area [18, 19]. In this regard, in the case of polymeric foams and similar cellular structures there is an additional challenge due to the representative volume element (RVE) size of the specimen, which requires a minimum number of cells to be present along the specimen length, in order to capture the continuum scale response of the material [6, 20, 21]; therefore limiting the minimum thickness of the tested specimen. None of the proposed solutions discussed above are capable of taking the local deformation, inertia and compressibility into account from an experimental perspective. Note that there are numerical simulations available in the literature that accurately describe the effects due to the aforementioned challenges on low impedance cellular materials, see e.g. [6]. However, from an experimental testing standpoint, there are still certain imitations that necessitate the development of alternative solutions to compensate for above-mentioned restriction.

Recent advances in the areas of high speed photography and full-field measurements have facilitated the study of deformation and failure of different materials in a wide range of time and length scales by accounting for the local deformation information [22-26]. In this regard, extensive attention has been drawn towards the application of virtual fields method and non-parametric approaches in dynamic deformation analysis of low impedance materials [27-31]. For instance, a non-parametric approach was proposed by Othman et al. [29] by which the full-field stress-strain response of low impedance synthetic rubber specimens was retrieved. This approach is based on the direct calculation of local stress magnitude using the inertia stress computed from acceleration field, and the boundary measured stress. This non-parametric method was successfully implemented by the authors of the present work to characterize dynamic deformation behavior of compressible polymeric foams under direct impact and at strain rates of up to 2600 s^{-1} [30, 31].

The main objective in this paper is to extend the previous works further by investigating the concurrent effects of specimen aspect ratio and the associated inertia effects and compressibility on the mechanical response of polymeric foams subjected to direct impact loading. Specimens with two different length-to-diameter ratios are subjected to direct impact loading using a modified shock tube apparatus. Deformation of the specimen is measured in-situ using high speed photography and digital image correlation. Using a non-parametric analysis along with displacement and acceleration fields acquired from image correlation, local stress-strain curves along specimen axis are extracted. It is observed that the transient deformation state creates a high variability in the local strain rate response over the length of the specimen. Local stress-strain curves are extracted at several positions along the specimen axis, each position with a different strain rate history. Attempts are made to utilize the entire set of constitutive data to extract useful stress-strain responses for the material over a wide range of strain rate conditions using a minimum number of impact tests. This was originally achieved by Avril et al. [32] to identify elasto-visco-plastic constitutive response using a single test at quasi-static loading conditions. Accordingly, the present work attempts to investigate the feasibility of extracting meaningful rate-dependent constitutive models from a single experiment carried out at very high strain rate conditions. The method is validated by comparing the results obtained from the proposed approach with those obtained from conventional SHPB tests.

3.3 MATERIAL AND SPECIMEN GEOMETRY

The material examined in this work is a rigid closed-cell polyurethane foam supplied by Sandia National Laboratories, under the commercial name TufFoam35. Nominal density of the as-received stock was measured as 560 kg/m^3 (35 pcf). Cellular structure of the foam is presented in Figure 3.1a, indicating average pore dimensions of 150 µm and 120 µm cell-wall thickness. Longitudinal wave speed of the examined foam, c_l, was calculated as 1180 m/s, using the initial density and compressive elastic modulus (780±20 MPa) measured under quasi-static (10^{-2} s^{-1}) conditions. Compressive elastic modulus of the material was determined as the initial slope of the quasi-static stress-strain curves averaged from three independent measurements.

Cylindrical specimens with two different length-to-diameter ratios are extracted from the as-received billets, the dimensions of which are shown in Figure 3.1b. Specimens are extracted from a single billet using a CNC waterjet, with a relatively smooth lateral surface finish and a ±0.1 mm dimensional variability. For image correlation purposes, a high contrast speckle pattern is applied on the lateral surface of each specimen. The speckle pattern consists of random black and white particles applied using conventional airbrush. Average speckle size is 100 µm.

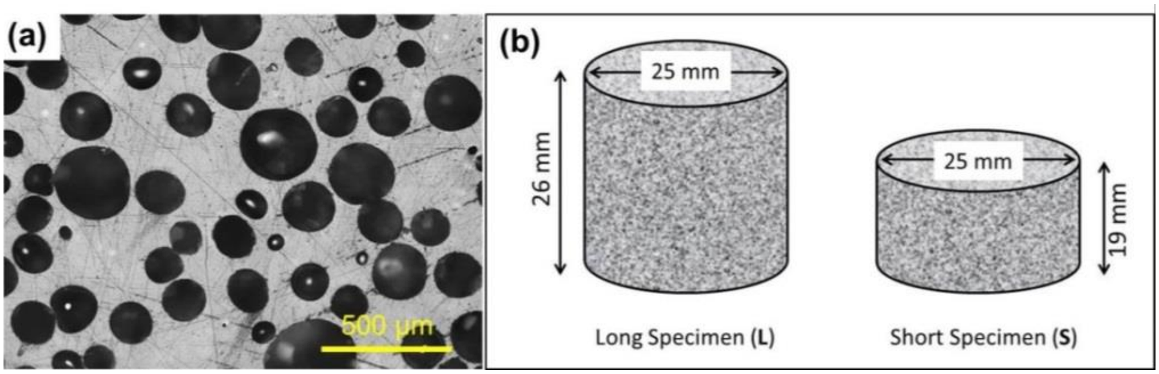

Figure 3.1 (a) Cellular structure of the foam examined in this work. (b) Cylindrical specimens with different initial dimensions used for direct impact experiments.

3.4 IMPACT LOADING

A modified shock tube apparatus is utilized to apply controlled direct impact on the specimens in the present work. Details on the design features of our shock tube can be found elsewhere [24, 30]. The shock tube is schematically shown in Figure 3.2a. Driver and driven sections of the tube are separated by stretched plastic diaphragms, under the commercial name “Mylar” sheets. The speckled specimen is fixed at the muzzle of the tube, inserted on a custom made load fixture. The specimen is held on the load fixture by the use of lithium grease, which also serves as the lubricant to diminish the effects due to friction. The same lubricant material is also applied on the impacted side of the specimen to reduce the effects of frictional stresses on the impacted end of the specimen, as well. Further details on the load fixture utilized in this work can be found in [30, 31]. The applied dynamic load is measured on the back side of the specimen using a piezoelectric load-cell, as shown in Figure 3.2b. The load-cell used in this work is 88.8 kN capacity PCB piezotronics® load-cell with 56 mV/kN sensitivity, designed primarily to measure compressive and impact forces. A polyimide film tap covering the cap surface of the load-cell reduces the effect of high frequency ringing associated with metal-to-metal contact.

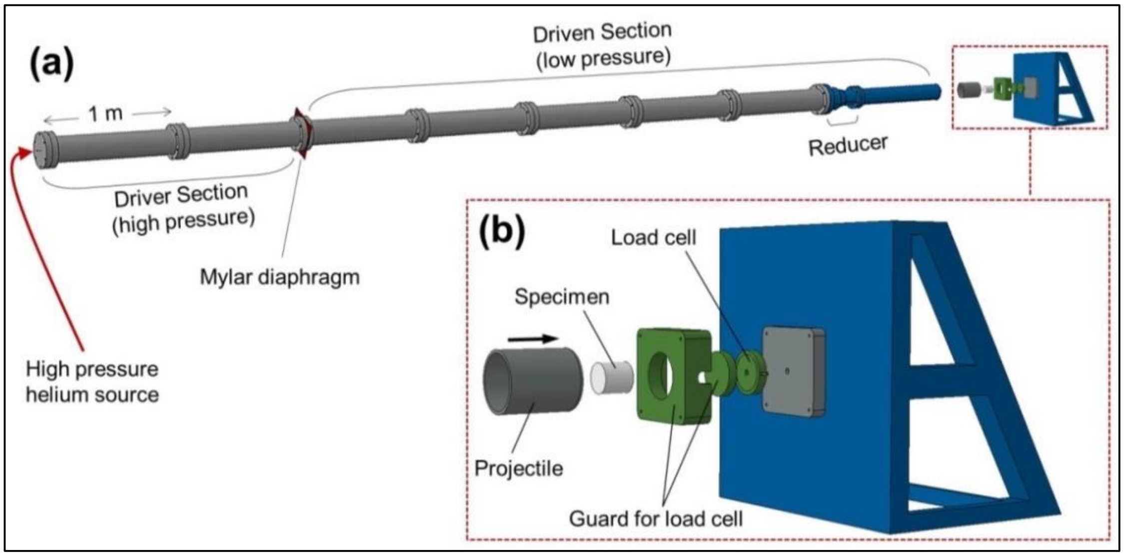

Figure 3.2 (a) Schematic of the shock tube in its entirety, with a magnified view of the load fixture shown in (b).

To increase the momentum transferred to the specimen and achieve higher strain rates, a high strength 70 gr aluminum projectile is directly shot at the specimen. The velocity of the projectile at the instant of impact can be manipulated by varying the thickness of the Mylar diaphragms [31]. Nominal strain rate applied on the specimen in dynamic compression can be calculated as [33]:

$$\dot{\varepsilon}_{nom} = \frac{v}{L_0} \tag{3.1}$$

where v and L_0 represent the impactor velocity and initial specimen length, respectively. In the present work, to facilitate the study of the effect of specimen aspect ratio, impactor velocities are selected such that the resulting $\dot{\varepsilon}_{nom}$ will be consistent for both specimen geometries. Therefore, the impactor velocities selected for direct impact experiments are

162 m/s and 123 m/s for L_0=26 mm (long) and L_0=19 mm (short) specimens, respectively (see Figure 3.1).

3.5 HIGH SPEED IMAGING AND DIGITAL IMAGE CORRELATION

High speed stereo imaging in conjunction with 3D digital image correlation is used to characterize the full-field dynamic deformation response of specimens. The stereo camera system consists of two Photron Fastcam SA-X2 cameras each equipped with a 100 mm macro lens. 256×152 pixel^2 images are acquired at a rate of 2×10^5 fps, resulting in inter-frame intervals of 5 μs. The magnification factor is approximately 5.26 pixel/mm. Image acquisition rate is synchronized with the rate of load-cell data collection through a high speed data acquisition system and an oscilloscope. High intensity white LED lights are employed as the illumination source. Stereo-camera system is calibrated using standard calibration plates prior to the onset of impact experiments. More details on the experimental setup, stereo camera system features and the resolution of the measurements can be found in [31].

Stereo images acquired during the deformation time are analyzed in the image correlation software Vic-3D (Correlated Solutions, Inc.). Subset and step sizes of 19 pixel and 1 pixel, respectively, are used for the correlation process. Full-field strain distribution was determined using Gaussian strain filtering with a filter size of 13. Temporal smoothing of the displacement data was conducted using 2nd order polynomial with 10 μs time filters.

3.6 DATA ANALYSIS

The local stress as a function of length and time is extracted by accounting for inertia using Eq. (3.2), developed from general dynamic equilibrium equation [31].

$$\sigma(z,t)=\sigma(0,t)+\int_{\xi=0}^{\xi=z}\rho(\xi,t)a(\xi,t)d\xi \tag{3.2}$$

where $z=0$ is the location on which force can be measured, i.e. location of the load-cell. $\rho(\xi,t)$ is local density and $a(\xi,t)$ is axial acceleration at a given time, *t*, and given position, ξ.

The integral on the right hand-side of Eq. (3.2) represents the inertia stress, which itself is a function of the spatial variations of axial acceleration and mass density. The fundamental idea here is to evaluate the variation of density and acceleration in time and space, and use these parameters to determine the distribution of inertia stress in the material. This inertia stress can then be superimposed with the boundary measured stress, i.e. $\sigma(0,t)$, to facilitate the calculation of the total axial stress.

In cases where dynamic stress analysis of incompressible materials (e.g. metals) is to be studied, mass density will remain constant and hence can be simply taken out of the integral. However, for the case of cellular materials, such as the one considered in this work, the density changes with the applied strain. To compensate for the change of density, the analytical model shown in Eq. (3.3) is considered:

$$\rho(z,t)=\rho_0\left[\exp(\varepsilon_z(z,t))\right]^{2\upsilon(z,t)-1} \tag{3.3}$$

The compressibility model shown in Eq. (3.3) is proposed based on the principle of mass conservation and allows for the calculation of the local mass density, $\rho(z,t)$, at any given time, *t*, and location, *z*, along the specimen length, as a function of initial density, ρ_0, local axial compressive strain, $\varepsilon_z(z,t)$, and local Poisson's ratio of the material, $\upsilon(z,t)$. Details on the derivation of the proposed model are beyond the scope of this work, but can be found elsewhere [31].

Once the acceleration and density at any time and location along the specimen length are known, the inertia term can be evaluated. The integral term on the right hand-side of Eq. (3.2) must be evaluated over the entire area of interest. To estimate this integral, the cylindrical geometry of the specimen is first sliced into several thinner sections. The number of these thin sections depends on the number of measurement points in the length direction, which itself is a function of subset size and step size used in the image correlation process. In the present work, short and long specimens are sliced into 80 and 110 thin sections, respectively. The thickness of each section, is ~0.22 mm (see Figure 3.3).

Density and acceleration values within each thin section are calculated by averaging the entire population of measurement points inside each section. In this way, a more circumferentially-homogeneous distribution of each parameter is obtained (see Figure 3.4). Next, the inertia stress integral in Eq. (3.2) is approximated as:

$$\int_{z=0}^{z=L} \rho(z,t) a_z(z,t) dz \approx \sum_{i=1}^{n} \rho_{(i)} a_{(i)} s_{(i)} \tag{3.4}$$

where, $\rho_{(i)}$ and $a_{(i)}$ represent the average values of density and axial acceleration in section i. $s_{(i)}$ is the thickness of section i, as depicted in Figure 3.3. n denotes the number of thin sections counted from left (Load-cell) side of Figure 3.3 up to the location of interest.

Having obtained the inertia stress as a function of time, the local total stress value can be determined by superimposing the boundary-measured stress (measured at the load-cell side) with the inertia stress evaluated from Eq. (3. 4). Local axial strain can also be readily extracted from the digital image correlation analysis. Note that the strain rate might vary spatially across the length of the specimen. Therefore, the local stress-strain responses obtained using the above procedure represent the local material response at variable strain rates.

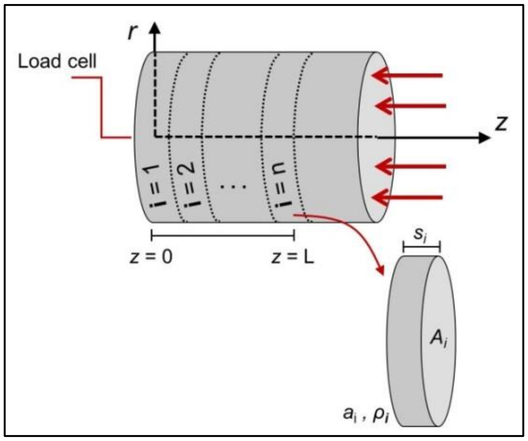

Figure 3.3 Cylindrical specimen sliced into a finite number of thinner sections, used to calculate the inertia stress applied at each point along the specimen axis.

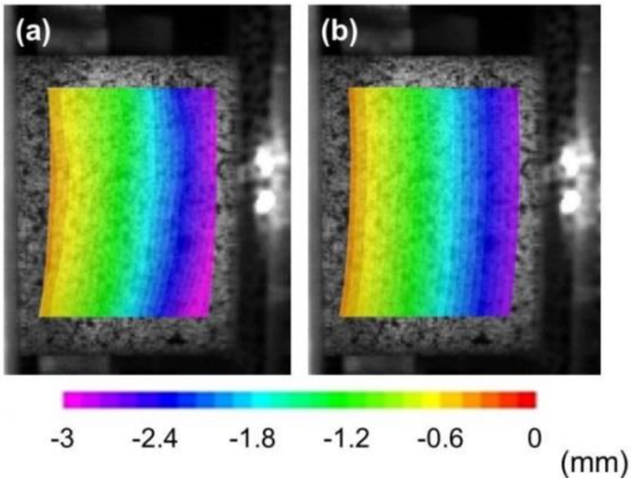

Figure 3.4 Typical full-field distribution of axial displacement, (a) as obtained via DIC and (b) after sectioning and averaging over each thinner section.

3.7 DYNAMIC DEFORMATION RESPONSE AND STRESS EQUILIBRIUM

Figure 3.5 shows the deformation sequence for both specimens at different times after the impact. The geometry of specimen after the impact indicates a mushroom shape formation at the impacted side, similar to observations made by Wang et al. [34]. Initiating from the impact side, surface failure followed by crushing are observed for short and long specimens at t = 55 μs and t = 40 μs, respectively. Therefore, the whole analysis is conducted over the first 55 μs for the short specimen, and 40 μs for the long specimen. Videos showing the deformation and failure of the specimens are available as supplementary materials.

Based on the longitudinal elastic wave speed calculated for the foam material examined here (c_l =1180 m/s), the time for a single stress wave traverse along the specimen axis, i.e. specimen characteristic time, is calculated as 16 μs for the short specimen, and 22 μs for the long specimen. It is well-established that at least three consecutive stress wave reverberations are required for stress equilibration [35]. Considering the characteristic times calculated for the specimens in this work, a minimum time of 48 μs will be required to achieve equilibrium for the short specimen. The equilibrium condition is expected to establish after a 66 μs delay time after the impact, for the long specimen. Note that the long specimen fails well before stress equilibration, while failure in short specimen takes place few microseconds after equilibrium. Interestingly, for both cases the transient duration is comparable to the entire duration of the test, indicating that the influence of inertial loading must be carefully studied during the entire course of deformation. One particular idea in the current work is to investigate different cases where (1) failure time is comparable to the stress equilibration time; (2) failure takes place before the establishment of quasi-static equilibrium. In such conditions, conventional determination of the material's constitutive response based only on boundary measurements is quite inadequate. This idea was justified by the use of short and long specimens.

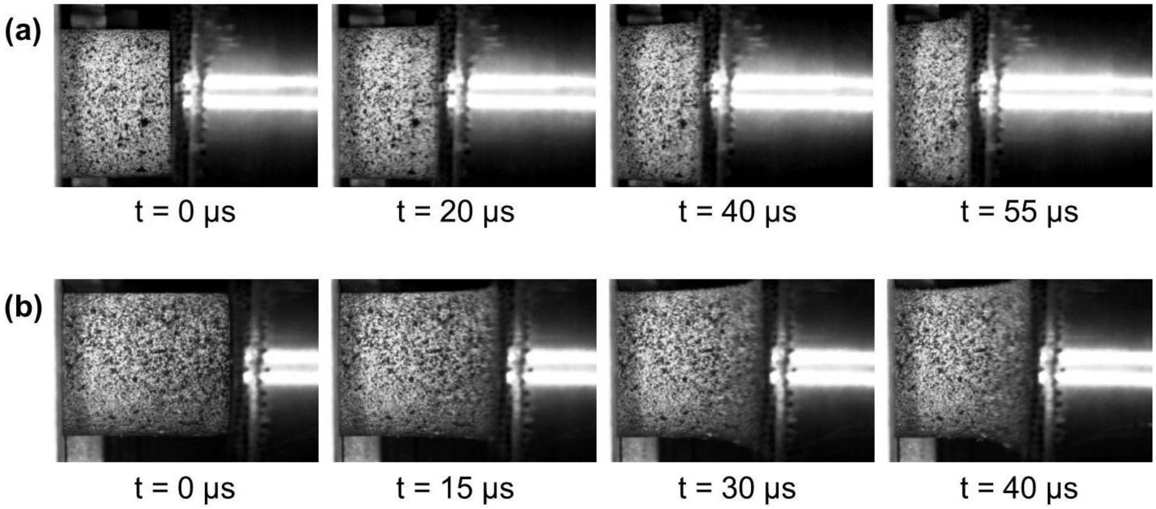

Figure 3.5 Deformation sequence at different times after the impact for (a) short and (b) long specimen. The reference time (t = 0 μs) denotes the time of first contact.

3.8 FULL-FIELD STRAIN

To investigate the deformation homogeneity in the specimens, the first step is the study of full-field strain distributions. Figure 3.6 shows full-field axial strain maps obtained from DIC. As shown in Figure 3.6 local strains of up to 20%, mainly in the middle sections, are developed in both specimens before failure. In addition, strong spatial gradients in axial strain along the specimen length are observed for both geometries, whereas the degree of such spatial variability is lower for the short specimen. To explain these significant strain gradients, note that the applied impact produces two distinct waves: (1) an elastic wave traveling at a speed of 1180 m/s; (2) a plastic wave moving at a slower speed. The plastic wave traverses over the length of the specimen, reducing its velocity to zero while plastically deforming the material. The stress developed behind the plastic wave deforms the material axially and laterally, and forms the mushroom configuration at the impacted side of the specimen, as shown earlier in Figure 3.5 [36]. Furthermore, the highest strain magnitudes are also developed at the location of the plastic wave front.

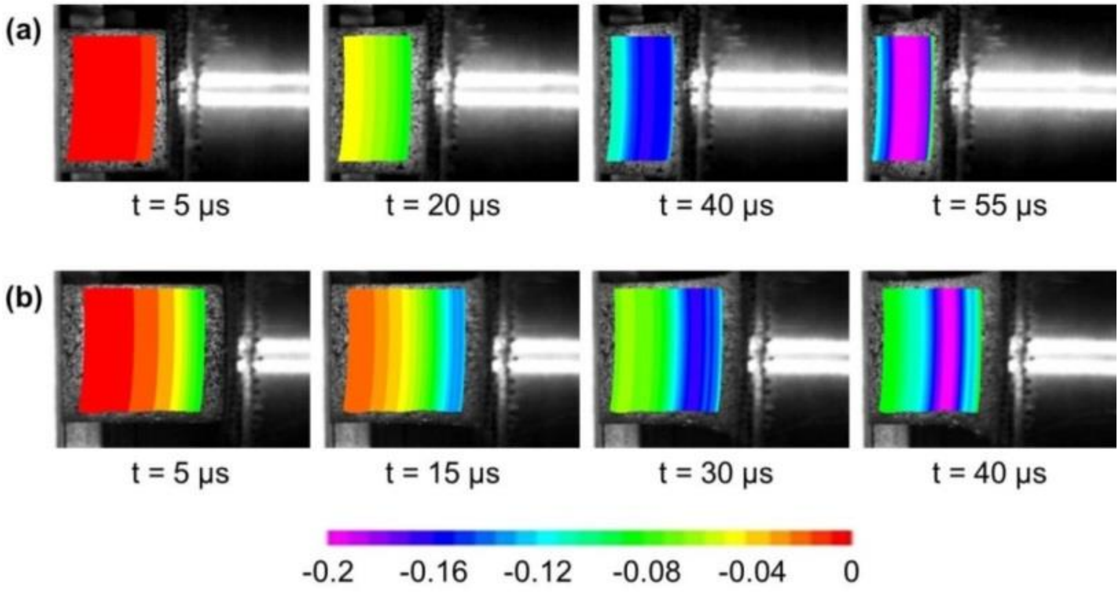

Figure 3.6 Full-field axial strain for (a) short specimen and (b) long specimen.

Similar non-uniform distribution of strain was also observed in the case of radial strain component. Figure 3.7 illustrates the variation of radial strain with time, extracted from five representative locations along the specimen axis. In both specimens, maximum radial strains of up to 10% are developed at the impacted side. Minimum values of radial strains are also indicated to be developed at the load-cell side. Comparing the two sets of curves shown in Figure 3.7 clearly indicates that the radial strain is distributed more inhomogeneously in the long specimen. This can be attributed to the higher impactor velocity used for the case of long specimen geometry. Note that as the contact is first established between the projectile and the specimen, waves (elastic and plastic waves) are created and travel through the specimen, changing their structure from uniaxial strain to a structure more closely associated with the uniaxial stress state [37]. This might be the reason behind the change of slope of the curves in Figures 3.7b and 3.7c at earlier deformation times (15< t < 20 μs) for both specimens. As the waves structure changes to the uniaxial stress, radial motion will no longer be constrained and the waves will have radial components as well as the axial ones. This change in the structure of the waves in the material results in a radial stress relief with the consequent large deformation of the material in radial direction. The magnitude of this stress relief rate is essentially a function of the impact velocity [36]. At higher impact velocities, the stress release takes place at a faster pace, giving rise to a faster radial expansion at the impacted side of the specimen, as observed in Figure 3.7c.

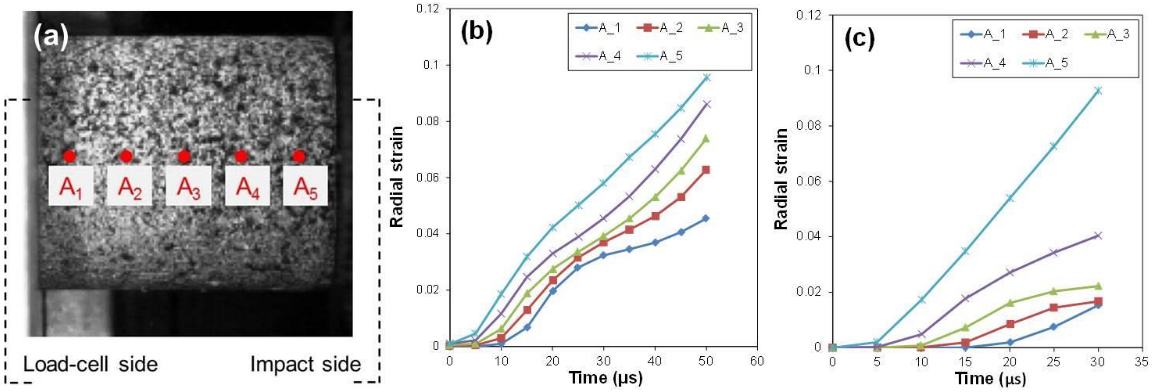

Figure 3.7 Variation of radial strain components extracted from five representative points shown in (a), for (b) short and (c) long specimen.

3.9 POISSON'S RATIO AND COMPRESSIBILITY

Evaluation of local Poisson's ratio is essential for calculation of the material compressibility in this work (see Eq. (3.3)). Local values of Poisson's ratio can be estimated using the full-field axial and radial strain data as:

$$\upsilon(z,t) = -\frac{d\varepsilon_r(z,t)}{d\varepsilon_z(z,t)} \approx -\left(\frac{\varepsilon_r(z,t+\Delta t)-\varepsilon_r(z,t)}{\varepsilon_z(z,t+\Delta t)-\varepsilon_z(z,t)}\right) \tag{3.5}$$

where ε_r and ε_z are the radial and axial strain components, respectively; and Δt is the inter-frame time. Figure 3.8 illustrates the variation of Poisson's ratio with time, for both specimen geometries.

The Poisson's ratio values depicted in Figure 3.8 are simply the average of all local values over load-cell and projectile halves of the specimen. No particular trend is observed in the values determined for Poisson's ratios in this work. For both short and long specimens, the average Poisson's ratio values are higher over the regions closer to the impacted side. This observation is consistent with the fact that both specimens undergo relatively higher radial expansion on their impacted side. In addition, the Poisson's ratio values obtained for the long specimen geometry are generally lower than those of the short specimen. It should be emphasized here that that the objective of this work is not to draw any conclusive information on the Poisson's effect and its possible rate sensitivity for the utilized foam material; rather, the evolution of Poisson's ratio under direct impact loading condition is taken into account only with the purpose of facilitating the calculation of material compressibility using Eq. (3.3).

Next, change of mass density over the entire area of interest is calculated using Eq. (3.3) and based on the average Poisson's ratios determined earlier. Figure 3.9 depicts the variation of normalized density in time, for the same five locations shown earlier in

Figure 3.7a. Considering the density curves in Figure 3.9, the following remarks are highlighted:

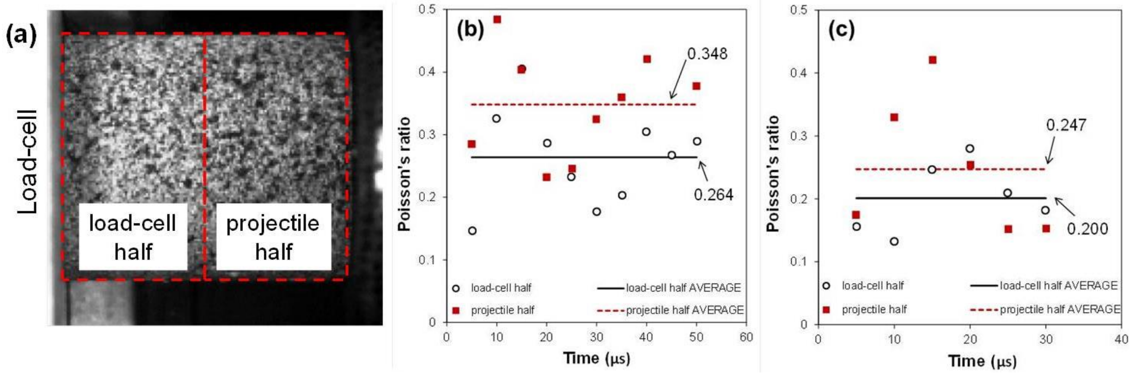

Figure 3.8 Variation of Poisson's ratio with time extracted from the load-cell half and projectile half shown in (a), for (b) short and (c) long specimen.

1) Local density increase of up to 11% is observed in both specimens.

2) There is a considerable delay in the rise time of curves extracted from A_1 and A_5 in both specimens. The delay times are approximately 8 μs and 14 μs for short and long specimens, respectively. These delays are due to the elapsed time for the stress wave to traverse the length of the specimen from impacted side to the load-cell side. Similar response was also observed earlier in Figure 3.7.

3) Consistent with the full-field strain response, both specimens show appreciable spatial variation in density, whereas such spatial variability is more prominent in the long specimen. The short specimen shows maximum compressibility on its mid-length locations (A_2 and A_3). This is because (i) the highest axial strains are developed within middle sections of this specimen (see Figure 3.6a); (ii) lower Poisson's ratios are measured on the areas closer to the load-cell side of the specimen.

4) Although higher Poisson's ratio values are obtained over the projectile side in the long specimen, substantially higher local densities are determined on its impacted side. This is due to significantly larger axial plastic strains evidenced previously in Figure 3.6b.

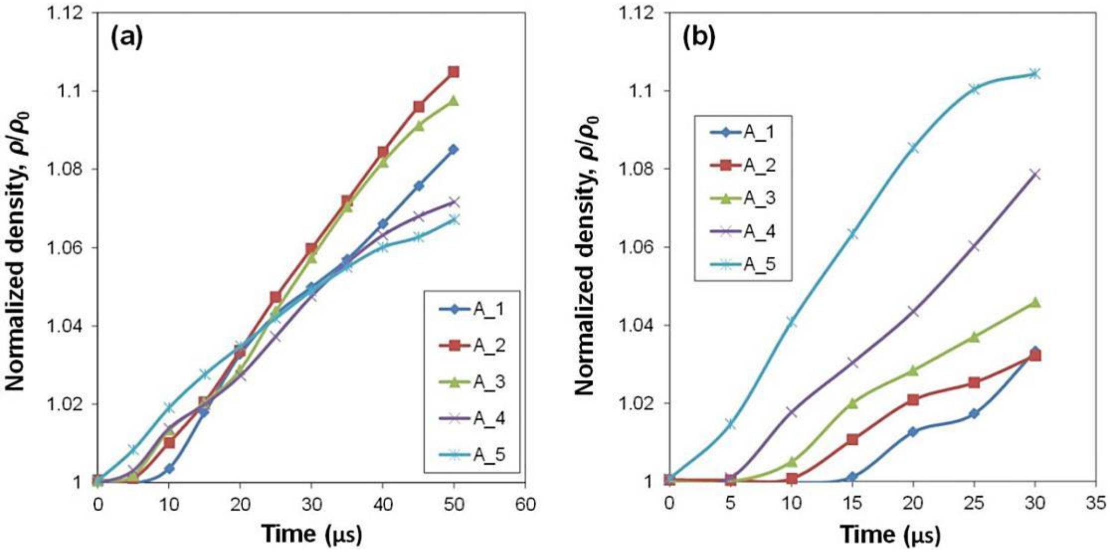

Figure 3.9 Variation of normalized density, ρ/ρ_0 , in time for (a) short and (b) long specimen, extracted for the representative locations indicated in Figure 3.7a. (ρ_0 = 560 kg/m^3)

3.10 STRAIN RATE AND ACCELERATION

Distributions of temporal derivatives –strain rate and acceleration– are determined over the gauge area using the DIC displacement and strain data and by applying a central difference scheme:

$$\dot{\varepsilon}_{ij}(t) = \frac{\varepsilon_{ij}(t+\Delta t) - \varepsilon_{ij}(t-\Delta t)}{2\Delta t} \tag{3.6a}$$

$$a_i(t) = \frac{u_i(t+\Delta t) - 2u_i(t) + u_i(t-\Delta t)}{\Delta t^2} \tag{3.6b}$$

where u_i and ε_{ij} denote the components of the displacement and strain, respectively. a_i and $\dot{\varepsilon}_{ij}$ represent acceleration and strain rate, respectively. Δt is inter-frame time (= 5 μs).

Variation of axial strain rate along the specimen axis has been plotted in Figure 3.10. Distribution of axial strain rate in the short specimen is such that at $t < 30$ μs, the highest strain rate values are measured at the impacted side of the specimen. At $t > 30$ μs, the highest strain rate regions move towards the middle section of the specimen. Similar behavior is observed in the long specimen, as well. This behavior can be attributed to the plastic wave traverse along the specimen axis. As the plastic wave passes along the specimen from the impacted side, it reduces its velocity to zero, while plastically deforming the portion of the specimen left behind [36].

It is clearly indicated that at any given time during the deformation stage, there is a substantial variation in local strain rate values within the gauge area. Up to 4000 s^{-1} spatial variation in strain rate is observed in the specimens in this work, whereas such spatial variation is more prominent in the long specimen. This high variation in strain rate –along with the strong rate sensitivity of the examined material– can actually be turned into an advantage, since the ultimate goal here is to identify a rate-dependent constitutive law for the examined foam using a minimum number of dynamic experiments. More discussion on this subject can be found in the following sections.

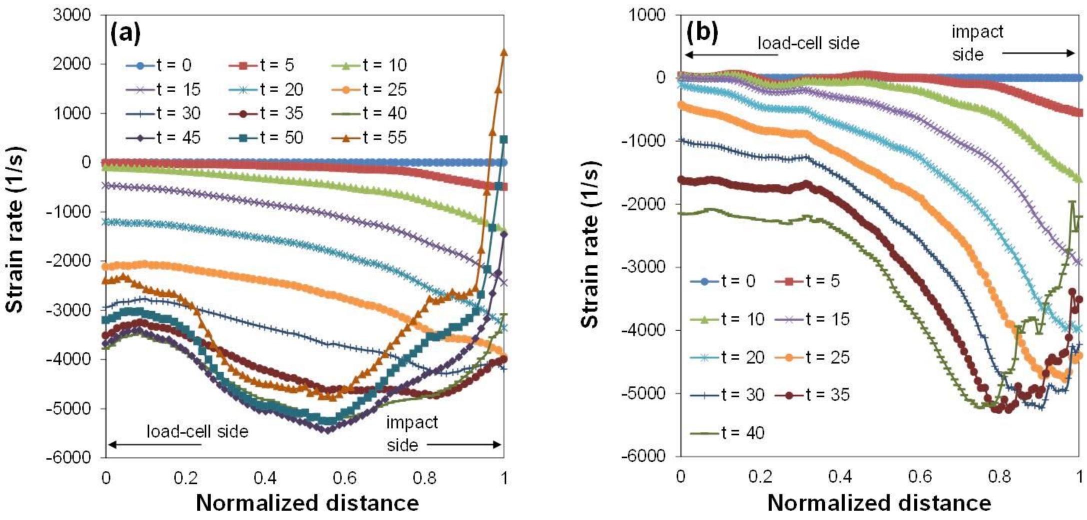

Figure 3.10 Variation of axial strain rate along the specimen axis for (a) short and (b) long specimens.

Figure 3.11 shows the variation of axial acceleration extracted from five locations along the specimen axis. Acceleration curves in Figure 3.11 show strong length-wise gradients. In both specimen geometries, the axial acceleration curves show a significant drop during the first 25-30 μs after the impact. The large magnitudes of acceleration calculated in early stages of impact attribute to the development of significant inertia stresses. After an early rapid increase in the magnitude of inertia stress, the acceleration is expected to be damped over a time duration that is roughly equal to 3 reverberations of the elastic stress wave. This is previously studied and confirmed in [31], where lower impact velocities were used to deform a similar material. In the current work, owing to the substantially higher impact velocities and the resultant applied strain rate, the long specimen fails before acceleration damping. In the short specimen, although deformation time is longer than that of the long specimen, complete damping does not take place and as a result, the effects of inertia stresses are significant and need to be included in the full-field stress analysis.

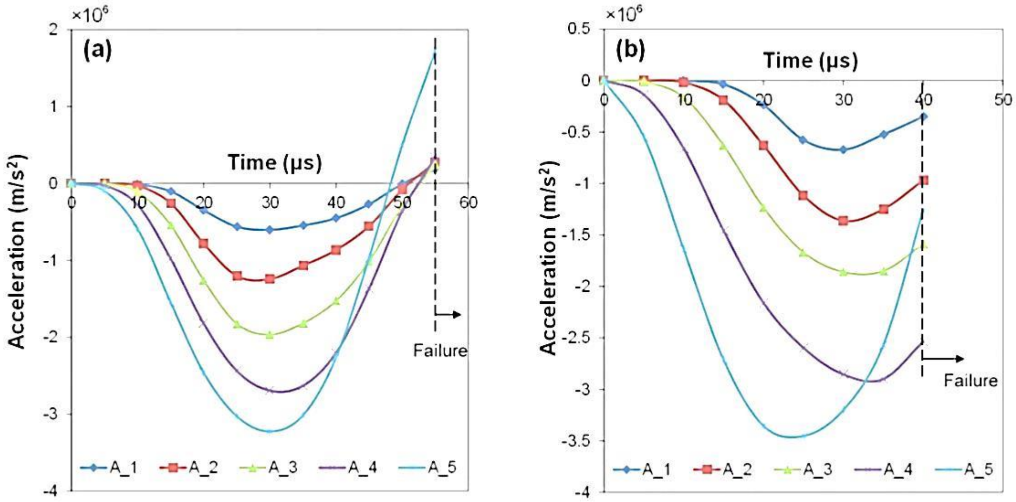

Figure 3.11 Variation of axial acceleration with time for (a) short and (b) long specimen, extracted for the representative locations indicated in Figure 3.7a.

3.11 INERTIA STRESS AND FULL-FIELD AXIAL STRESS

Having obtained density and acceleration fields, inertia stress distribution over the entire area of interest can be evaluated for both specimens using Eqs. (3.2)-(3.4). Figure 3.12 illustrates the evolution of inertia stresses along the axis of each specimen at different times prior to failure. Axial inertia stress developed in the specimen is clearly indicated to have the highest magnitude at the impacted side at any given time. In addition, higher values of inertia stress are measured in the long specimen, due to the higher impact velocity and the resultant higher axial accelerations.

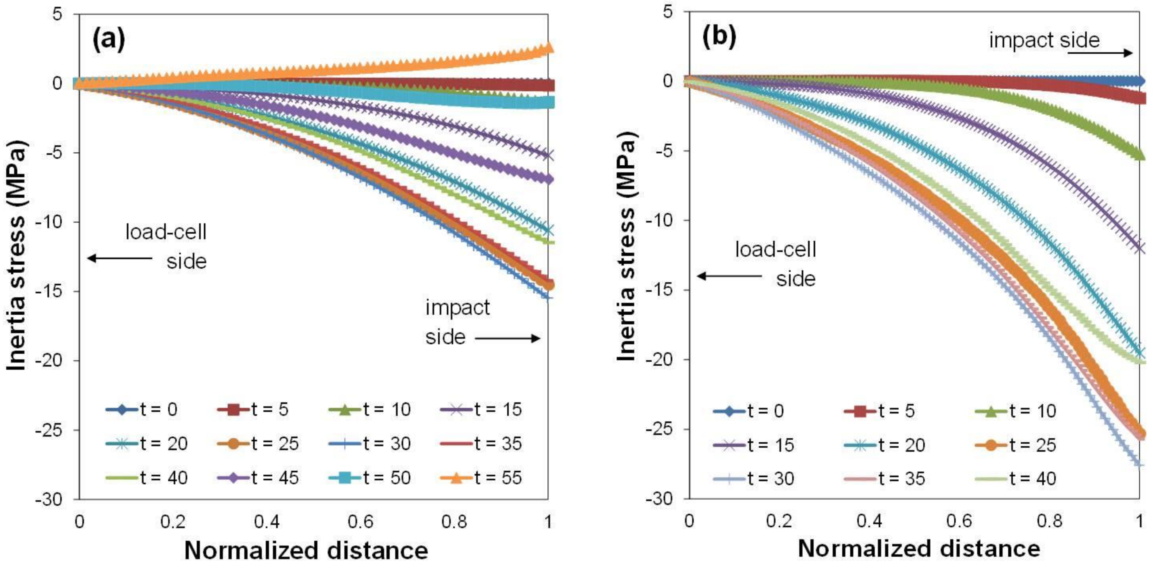

Figure 3.12 Variation of inertia stress along the specimen axis for (a) short and (b) long specimens.

Variation of total axial stress along the specimen axis is obtained next by superimposing the inertia stress with the boundary measured stress (see Eq. (3.2)). The true stress value at the boundary, i.e. load-cell side, is evaluated as the ratio between the reaction force measured by the load-cell and the current cross sectional area at load-cell side of the specimen. Current cross sectional area is determined using the measurement of specimen profile facilitated by transforming the original Cartesian coordinate system into a polar coordinate system. This approach has been explained in more details in [31]. Evolution of true stress at the load-cell side of the specimens is shown in Figure 3.13. Note that the boundary measured stress is compressive, but has been plotted in positive values in this figure, for convenience. Both curves in Figure 3.13 show progressive increase in stress until failure, and continue to rise even after the specimens fail. As mentioned earlier, specimen failure in this work is referred to the observation of visible surface cracks mostly formed on regions closer to the impacted side of each specimen, followed by total crushing. At the instant of failure, although the integrity of the specimen is lost, the stress wave can still propagate through the undamaged parts of the specimen. This attributes to the steady increase of the boundary measured force for at least 40 μs after the failure.

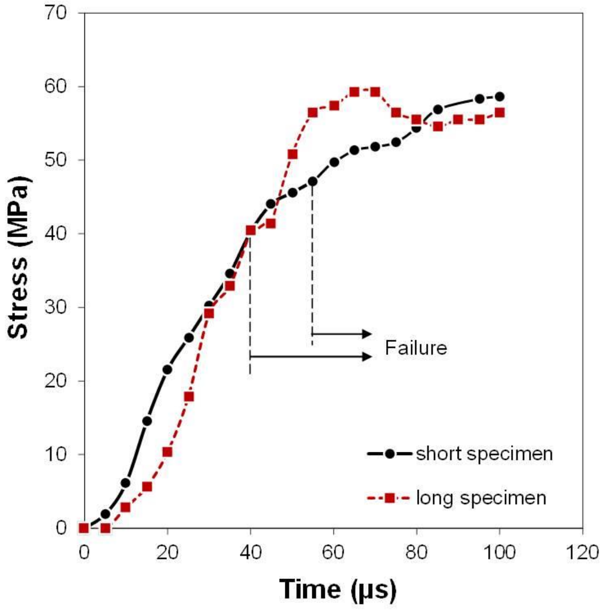

Figure 3.13 Variation of true stress measured at the boundary for short and long specimens.

Variation of total, i.e. inertia plus boundary measured, axial stress along the specimen axis is plotted in Figure 3.14 for short and long specimens. It should be noted that:

1) Total axial stress values indicate considerable length-wise variability, the degree of which is higher for the long specimen.

2) Magnitude of the total axial stress is larger at the impact side of the specimen, for the entire deformation time in the long specimen, as well as the first 45 μs after the impact in the short specimen.

3) At t > 45 μs, upon the reversion of the axial acceleration in the short specimen, the inertia stress changes sign. This was evidenced earlier in Figures 3.11 and 3.12. The sign change gives rise to the development of tensile inertia stresses at the impacted side of the specimen, decreasing the magnitude of the previously developed compressive stresses and consequently lowering the spatial variation of stress along the specimen axis. Predominance of tensile inertia stresses over the areas closer to the impacted side of the specimen is indicated to promote tensile strain rates at t > 45 μs in the short specimen, as depicted earlier in Figure 3.10a.

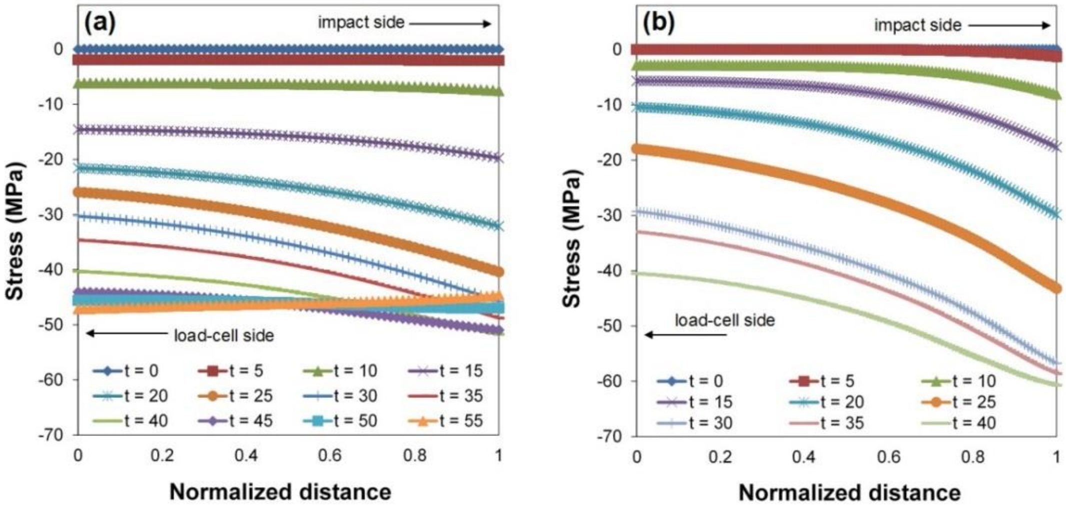

Figure 3.14 Variation of total axial stress along the specimen axis for (a) short and (b) long specimens at different times after the impact.

3.12 IDENTIFICATION OF INELASTIC CONSTITUTIVE RESPONSE

Figure 3.15 shows the variation of strain, strain rate and total stress in time for both specimens. Note that all variables shown in Figure 3.15 are compressive, however for convenience they are all plotted as positive quantities hereafter. The trends indicated for total stress are very similar to those observed in [31]. The only differences between the present result with those reported earlier are: (1) quasi-static equilibrium is not achieved before the specimen failure in this work; thus the stress-time curves do not tend to fully converge. This is particularly evident in stress-time curves obtained for the long specimen; (2) Due to the temporal filtering of the displacement data in the present work, no sudden increase is observed in the stress-time curves extracted from the impacted side; rather there exists a smoother rise in the value of total stress at earlier stages of deformation. In cases where no temporal smoothing is carried out, there will be a more abrupt increase of stress value on the locations more closely associated with the impacted side of the specimen [31].

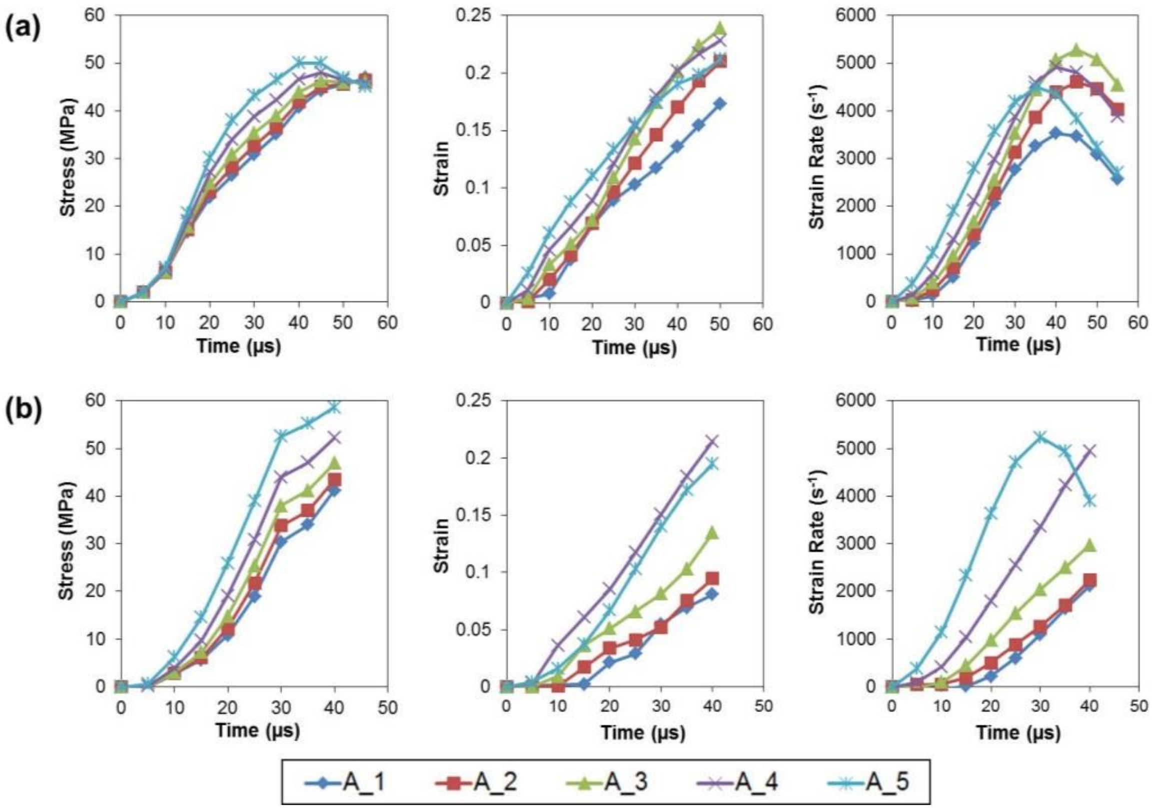

Figure 3.15 Variation of total stress, strain and strain rate with time for (a) short and (b) long specimens extracted from the representative points indicated in Figure 3.7a.

Having obtained the full-field strain, strain rate and stress distributions in time and over the entire gauge area, local stress-strain response of the material can be extracted at any given location within the area of interest. Accordingly, the local stress-strain curves extracted from three locations over the specimen axis are plotted in Figure 3.16 along with their associated strain rate curves. It is clearly observed that although stress-strain curves can be acquired locally, no meaningful material response may be inferred from these local curves. This is because the local curves are not plotted at constant strain rates; not to mention that the issue becomes more challenging in the case of long specimen with higher spatial and temporal strain rate variabilities. High spatial variability of strain also attributes to the peculiar local stress-strain curves plotted in Figure 3.16. This issue seems to be deteriorated for the longer specimen, containing higher strain inhomogeneity along its axis. Last but not least, strain and stress states vary in length of the specimen, changing from uniaxial strain state on the locations closer to the load-cell side to uniaxial stress state created behind the plastic wave front, over the locations closer to the impacted side. In this work we are only considering the axial stress-strain response of the material, regardless of the contribution of the lateral stresses and/or strains. Therefore, the discrepancies observed in Figure 3.16 were actually not far from expectation.

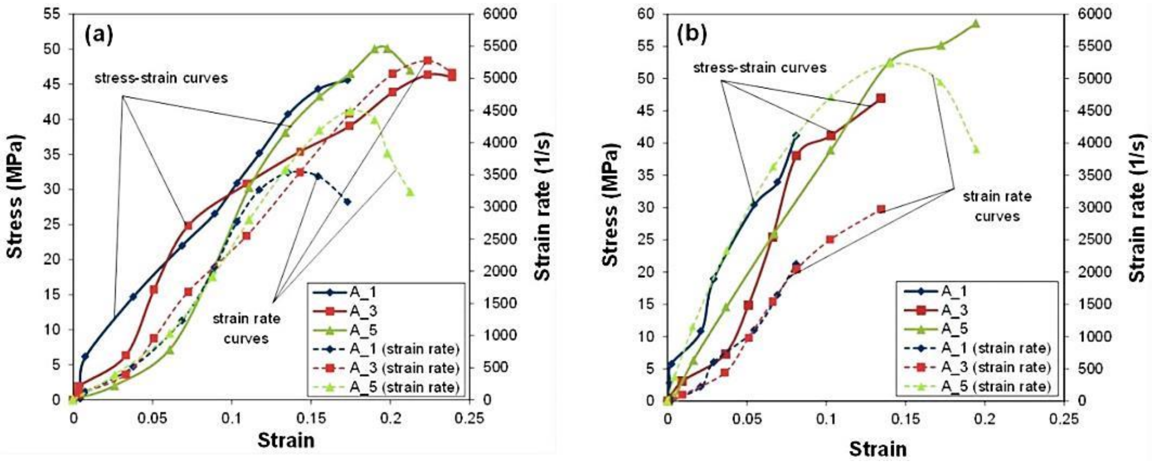

Figure 3.16 Local stress-strain curves in (a) short and (b) long specimen, extracted for the representative locations indicated in Figure 3.7a.

To resolve the above-mentioned challenges and provide more meaningful constitutive information by obtaining stress-strain curves at constant strain rate conditions, the following mathematical approach is proposed:

1. Construct a full-grid material data set with known local strain, strain rate and stress data calculated within the gauge area. Note that the larger the number of data points in the grid, the more accurate the final results will be. In this work, the full-grid data set is constructed by combining the entire collection of stress-strain-strain rate data acquired for both short and long specimens.

2. Prescribing the target values for strain and strain rate, use a scattered-data interpolation scheme to estimate the local stress. In the present work, a triangulation-based cubic interpolation with C^2 continuity is used for this purpose. The interpolation is performed in the software MATLAB®, using an in-house written code.

3. Reconstruct stress-strain curves at a constant strain rate by repeating step 2.

Following this procedure and using the entire collection of data points from both specimen geometries, constitutive curve of the material at constant strain rate of 1000 s^{-1}

is first acquired over a strain range of 0.05 to 0.125, and set as the reference curve. Due to the limited strain data obtained within the strain rate range of 2000-5000 s^{-1}, the curves corresponding to $\dot{\varepsilon}_0 > 1000$ s^{-1} could not be directly reconstructed over the desired strain range of 0.05 to 0.125. Therefore, setting the stress-strain curve interpolated for $\dot{\varepsilon}_0 = 1000$ s^{-1} as the reference, and taking advantage of a rate dependent constitutive model, stress-strain curves at $\dot{\varepsilon} > 1000$ s^{-1} were identified for the examined foam. A simple rate-dependent constitutive model proposed by Nagy et al. [38] was considered for this purpose. The constitutive model suggested by Nagy et al. [38] is expressed as:

$$\sigma(\varepsilon) = \sigma_0(\varepsilon)\left(\frac{\dot{\varepsilon}}{\dot{\varepsilon}_0}\right)^{m(\varepsilon)} \tag{3.7}$$

where $m(\varepsilon)$ is strain rate sensitivity exponent of the material, assumed to be strain dependent [38]. The reference stress, $\dot{\varepsilon}_0$, in this work is taken to be the flow stress of the material at $\dot{\varepsilon}_0 = 1000$ s^{-1}. Strain rate sensitivity of the material $m(\varepsilon)$ is determined using the reference curve (i.e. constitutive curve at $\dot{\varepsilon}_0 = 1000$ s^{-1}) and used to reconstruct stress-strain curves at $\dot{\varepsilon} > 1000$ s^{-1}.

Figure 3.17a shows the variation of normalized stress vs. normalized strain rate at different strain magnitudes. The slope of the best linear fit for each curve is determined as the strain rate sensitivity. It is clearly observed that m values calculated in the strain range of 1000 s^{-1} to 5000 s^{-1} indicate strong strain dependence. Figure 3.17b illustrates the variation of m as a function of applied strain, with its best fitting curve. The trends observed for the strain-dependence of m are similar to those previously documented in [38], confirming that the strain rate sensitivity increases at larger strains.

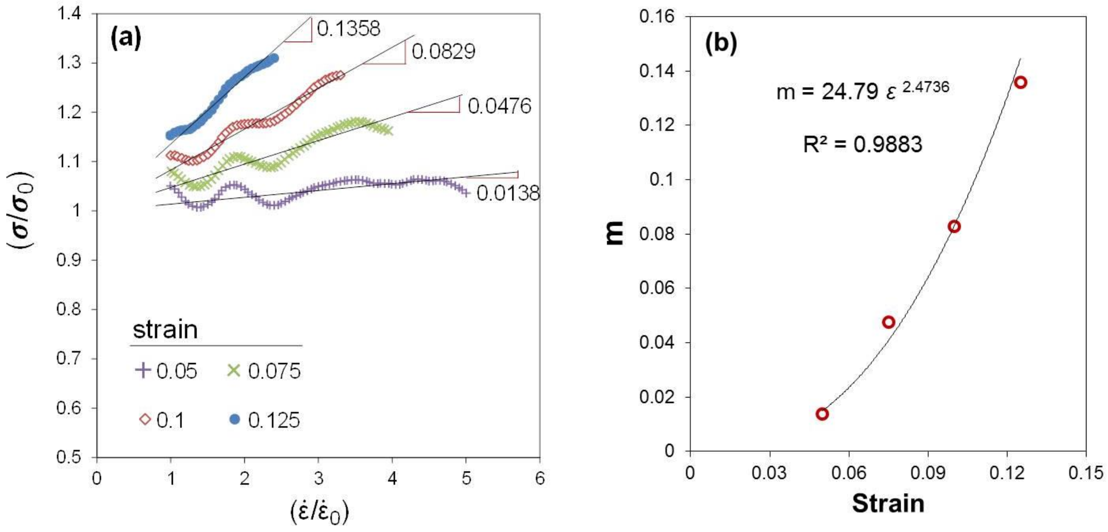

Figure 3.17 Variations of (a) normalized stress vs. normalized strain rate at various strain magnitudes, and (b) strain rate sensitivity exponent, *m*, with strain over a range of $0.05 < \varepsilon < 0.125$ and $1000 < \dot{\varepsilon} < 5000$ s^{-1}.

Figure 3.18a illustrates the reconstructed flow curves at constant strain rates in the range of 1000 s^{-1} to 5000 s^{-1}, confirming the more significant influence of strain rate on the constitutive response of the material at higher strain values. One may argue that the data used to reconstruct the stress-strain curves do not necessarily contain the same density information, since each specimen shows variable compressibility along its axis. In this regard, note that the spatial and temporal variation of material density is already incorporated into the analysis from the beginning, by the application of a compressibility model described earlier in Eq. (3.3).

To further investigate the effect of strain rate on the constitutive behavior of the examined foam, stress values determined from the analytical approach are plotted as function of strain rate in Figure 3.18b. Figure 3.18b allows for a consistent comparison of strain rate effect on the stress response well beyond the elastic deformation regime and prior to failure. The trend observed in Figure 3.18b indicates that beyond 1000 s^{-1}, the foam exhibits a rapid increase in rate sensitivity. This observation is very similar to the previously documented data on various polymeric foam specimens [39, 40] and attributes to the critical strain rate hypothesis proposed for cellular structures [41].

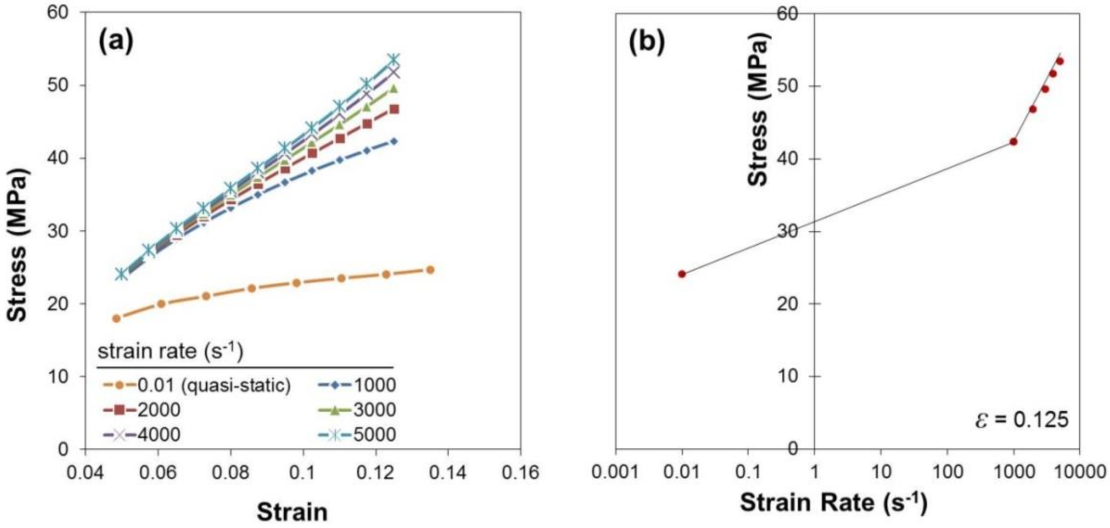

Figure 3.18 (a) Stress-strain curves plotted for quasi-static and dynamic conditions. (b) Variation of stress with applied strain rate at a constant strain of 0.125.

Finally, in order to validate the results obtained from this work, a comparison was made between the stress-strain response of the examined foam measured from conventional SHPB testing and the results acquired in this work. For this purpose, a conventional SHPB apparatus with details provided in [42] was employed. Smaller cubic specimens of 14×14×14 mm^3 were used in SHPB tests to enforce more uniform deformation. Typical stress-strain and strain rate response obtained from SHPB tests on the specimen is shown in Figure 3.19a. Note that the strain rate applied on the specimen in the SHPB test shows more temporal uniformity before failure. The average strain rate applied on the specimen over a strain range of 0.05-0.125 is determined as 1500 s^{-1} in the SHPB experiment. Using this average strain rate along with the results of the proposed analytical approach, the constitutive response of the material was predicted. Figure 3.19b compares the constitutive response obtained from experimental SHPB and the model prediction. Note that the results obtained from the approach proposed in this work predict the non-linear stress-strain curve of the examined foam with >90 % accuracy.

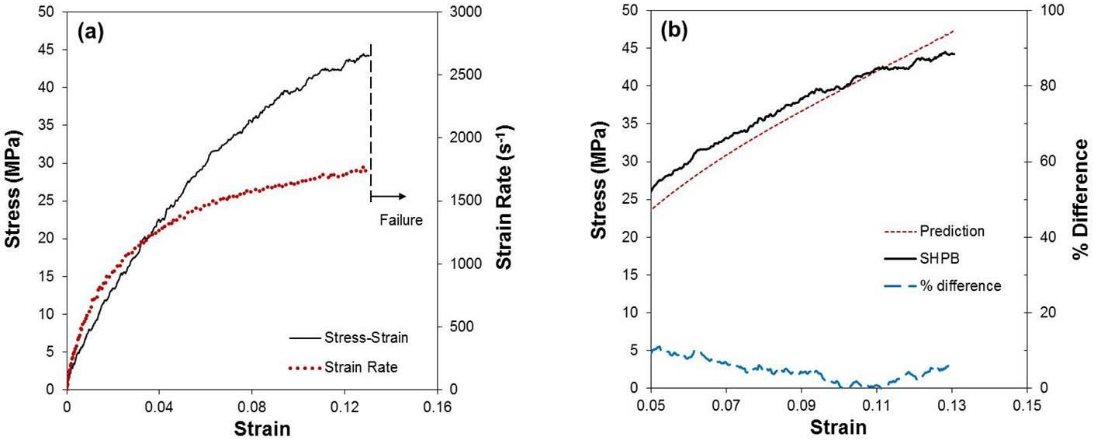

Figure 3.19 (a) Constitutive response of the examined foam obtained from conventional SHPB. (b) Comparison between the experimentally obtained and predicted stress-strain curves.

Last but not least, the approach described in this work can be considered as a novel methodology for extracting a large collection of data from a minimum number of testings. This method of analysis does not depend on any specific specimen geometry, nor does it require the use of any pulse shaping mechanism, since the effect of inertia loading is already embedded in the analysis. Clearly, this was the first attempt to demonstrate the feasibility of the application of the procedure detailed in this work. There are indeed several factors that can improve the results of the proposed approach. The most important factor is the application of more advanced cameras with enhanced temporal and spatial resolutions which allow for the acquisition of a larger number of higher resolution images at significantly shorter interframe times.

The parameter identification method presented in this work is still in its early phases, and certainly needs more improvement. One specific aspect which in our opinion can significantly improve the quality of the results of such approach is the use of more advanced mathematical tools to identify the trends hidden within the scattered data obtained from the non-parametric analysis. Simple scattered data interpolation was employed for this purpose in the present work. Attempts are currently being made to take advantage of more powerful mathematical tools, particularly neural networks [43], to further improve the results obtained from similar experiments.

3.13 CONCLUSIONS

A recently proposed non-parametric analysis was conducted to study the influence of specimen length-to-diameter ratio on constitutive response of polymeric foams under direct impact. The study was facilitated by the use of high speed stereovision photography in conjunction with 3D digital image correlation. Full-field stress distribution in the specimen was reconstructed by superimposing the boundary-measured stress with the calculated inertia stresses. Results obtained in this work clearly indicate that the effects of inertia are more significant in specimens with higher length-to-diameter ratios; however, taking advantage of the utilized non-parametric analysis, consistent constitutive behaviors can be obtained regardless of the specimen aspect ratio. One particular remark highlighted in the current study was that the approach implemented here facilitates the accurate characterization of the impact response of low impedance cellular polymers in conditions where stress equilibration does not take place before failure. Results obtained for the long specimen in this work are typical of such conditions, i.e. where the specimen failure occurs well before the establishment of quasi-static equilibrium.

Additionally, it was confirmed that the low impedance characteristic of the foam specimens can give rise to appreciable spatial variability in strain, strain rate and stress. In particular, temporal and spatial variations of strain rate elevate the complexities encountered in analyzing the constitutive response of the material. Spatial and temporal variabilities of strain rate were turned into an advantage, by conducting an analytical approach to identify the rate-dependent constitutive response of the material. It was finally proposed that that the method implemented in the present research can facilitate the identification of the viscoplastic constitutive laws over a wide range of strain rates, using minimum number of experimental testings.

3.14 LIST OF REFERENCES

[1] Gibson LJ, Ashby MF. Cellular solids: Structure and properties. 2nd ed. Oxford. 1997.

[2] Zhao H. Testing of polymeric foams at high and medium strain rates. Polymer Testing 1997; 16: 507-516.

[3] Liu Q, Subhash G, Gao XL. A parametric study on crushability of open-cell structural polymeric foams. Journal of Porous Materials 2005; 12: 233-248.

[4] Liu Q, Subhash G. A phenomenological constitutive model for foams under large deformations. Polymer Engineering and Science 2004; 44(3): 463-473.

[5] Subhash G, Liu Q. Crushability maps for structural polymeric foams in uniaxial loading under rigid confinement. Experimental Mechanics 2004; 44(3): 289-294.

[6] Pal S, Maiti S, Subhash G. Effect of microscopic deformation mechanisms on the dynamic response of soft cellular materials. Mechanics of Materials 2010; 42: 118-133.

[7] Yunoshev AS, Sil'vestrov VV. Development of the polymeric split Hopkinson bar technique. Journal of Applied Mechanics and Technical Physics 2001; 42(3): 558-564.

[8] Casem DT, Fourney WL, Chang P. A polymeric split Hopkinson pressure bar instrumented with velocity gages. Experimental Mechanics 2003; 43(4): 420-427.

[9] Chen W, Zhang B, Forrestal MJ. A split Hopkinson bar technique for low-impedance materials. Experimental Mechanics 1999; 39(2): 81-85.

[10] Bacon C. An experimental method for considering dispersion and attenuation in a viscoelastic Hopkinson bar. Experimental Mechanics 1998; 38(4): 242-249.

[11] Wang L, Labibes K, Azari A, Pluvinage G. Generalization of split Hopkinson bar technique to use viscoelastic bars. International Journal of Impact Engineering 1994; 15(5): 669-686.

[12] Zhao H, Gary G, Klepaczko JR. On the use of a viscoelastic split Hopkinson pressure bar. International Journal of Impact Engineering 1997; 19(4): 319-330.

[13] Sharma A, Shukla A, Prosser RA. Mechanical characterization of soft materials using high speed photography and split Hopkinson pressure bar technique. Journal of Materials Science 2002; 37(5): 1005-1017.

[14] Casem DT, Fourney W, Chang P. Wave separation in viscoelastic pressure bars using single-point measurements of strain and velocity. Polymer Testing 2003; 22(2): 155-164.

[15] Subhash G, Liu Q, Gao X. Quasistatic and high strain rate uniaxial compressive response of polymeric structural foams. International Journal of Impact Engineering 2006; 32(7): 1113-1126.

[16] Chen W, Lu F, Winfree N. High strain rate compressive behavior of a rigid polyurethane foam with various densities. Experimental Mechanics 2002; 42(1): 65-73.

[17] Song B, Chen W, Frew DJ. Dynamic compressive response and failure behavior of an epoxy syntactic foam. Journal of Composite Materials 2004; 38(11): 915-936.

[18] Gama BA, Lopatnikov SL, Gillespie JW. Hopkinson bar experimental technique: A critical review. Applied Mechanics Reviews 2004; 57(4): 223-250.

[19] Ouellet S, Cronin DS, Moulton J, Petel EO. High rate characterization of polymeric closed-cell foams: Challenges related to size effects. In: Chalivendra V, Song B, Casem D (Editors), Dynamic behavior of materials – Volume 1, Proceedings of the 2012 Annual Conference on Experimental and Applied Mechanics, Springer, 2013, pp 21-28. DOI 10.1007/978-1-4614-4238-7_4

[20] Kanaun S, Tkachenko O. Representative volume element and effective elastic properties of open cell foam materials with random microstructures. Journal of Mechanics of Materials and Structures. 2007; 2(7): 1607-1628.

[21] Alsayednoor J, Harrison P, Guo Z. Large strain compressive response of 2-D periodic representative volume element for random foam microstructures. Mechanics of Materials 2013; 66: 7-20.

[22] Liu J, Saletti D, Pattofatto S, Zhao H. Impact testing of polymer foam using Hopkinson bars and digital image analysis. Polymer Testing 2014; 36: 101-109.

[23] Sutton MA, Orteu JJ, Schreier HW. Image correlation for shape, motion and deformation measurements. Springer. NY. 2009

[24] Mallon S, Koohbor B, Kidane A, Sutton MA. Fracture behavior of prestressed composites subjected to shock loading: A DIC-based study. Experimental Mechanics 2015; 55: 211-225.

[25] Gilat A, Schmidt TE, Walker AL. Full field measurement in compression and tensile split Hopkinson bar experiments. Experimental Mechanics 2009; 49: 291-302.

[26] Pierron F, Zhu H, Siviour C. Beyond Hopkinson's bar. Philosophical Transactions of the Royal Society A 2014; 372: 20130195.

[27] Moulart R, Pierron F, Hallett SR, Wisnom MR. Full-field strain measurement and identification of composite moduli at high strain rate with the virtual fields method. Experimental Mechanics 2011; 51: 509-536.

[28] Yoon S, Giannakopoulos I, Siviour CR. Application of the virtual fields method to the uniaxial behavior of rubbers at medium strain rates. International Journal of Solids and Structures 2015; 69-70: 553-568.

[29] Othman R, Aloui S, Poitou A. Identification of non-homogeneous stress fields in dynamic experiments with a non-parametric method. Polymer Testing 2010; 29: 616-623.

[30] Koohbor B, Mallon S, Kidane A, Lu WY. The deformation and failure response of closed-cell PMDI foams subjected to dynamic impact loading. Polymer Testing 2015; 44: 112-124.

[31] Koohbor B, Kidane A, Lu WY, Sutton MA. Investigation of the dynamic stress-strain response of compressible polymeric foam using a non-parametric analysis. International Journal of Impact Engineering 2016; 91: 170-182.

[32] Avril S, Pierron F, Sutton M, Yan J. Identification of elasto-visco-plastic parameters and characterization of Lüders behavior using digital image correlation and the virtual fields method. Mechanics of Materials 2008; 40: 729-742.

[33] Samanta SK. Dynamic deformation of aluminum and copper at elevated temperatures. Journal of Mechanics and Physics of Solids 1971; 19: 117.

[34] Wang L, Ding Y, Yang L. Experimental investigation on dynamic constitutive behavior of aluminum foams by new inverse methods from wave propagation measurements. International Journal of Impact Engineering 2013; 62: 48-59.

[35] Davies EDH, Hunter SC. The dynamic compression testing of solids by the method of the split Hopkinson pressure bar. Journal of Mechanics and Physics of Solids 1963; 11(3): 155-179.

[36] Nicholas T, Recht RF. Introduction to impact phenomena. In: High Velocity Impact Dynamics, Edited by Zukas JA. 1990, John Wiley & Sons, 1990.

[37] Taylor G. The use of flat-ended projectiles for determining dynamic yield stress – I. Theoretical considerations. Philosophical Transactions of the Royal Society A 1948; 194: 289-299.

[38] Nagy A, Ko WL, Lindholm US. Mechanical behavior of foamed materials under dynamic compression. Journal of Cellular Plastics 1974; 10(3): 127-134.

[39] Ouellet S, Cronin D, Worswick M. Compressive response of polymeric foams under quasi-static, medium and high strain rate conditions. Polymer Testing 2006; 25: 731-743.

[40] Bouix R, Viot, Lataillade JL. Polypropylene foam behavior under dynamic loadings: Strain rate, density and microstructure effects. International Journal of Impact Engineering 2009; 36: 329-342.

[41] Tan PJ, Reid SR, Harrigan JJ. On the dynamic mechanical properties of open-cell metal foams – A re-assessment of the 'simple-shock theory'. International Journal of Solids and Structures 2012; 49: 2744-2753.

[42] Ravindran S, Tessema A, Kidane A. Local deformation and failure mechanisms of polymer bonded energetic materials subjected to high strain rate loading. Journal of Dynamic Behavior of Materials 2016; 2: 146-156.

[43] Bobbili R, Madhu V, Gogia AK. Neural network modeling to evaluate the dynamic flow stress of high strength armor steels under high strain rate compression. Defence Technology 2014; 10: 334-342.

CHAPTER 4

CHARACTERIZING THE CONSTITUTIVE RESPONSE AND ENERGY ABSORPTION OF RIGID POLYMERIC FOAMS SUBJECTED TO INTERMEDIATE-VELOCITY IMPACT [3]

---

[3] Koohbor B, Kidane A, Lu W. *Polymer Testing* 2016; 54: 48-58.
doi:10.1016/j.polymertesting.2016.06.023
Reused here with permission of publisher.

4.1 ABSTRACT

As an optimum energy-absorbing material system, polymeric foams are needed to dissipate the kinetic energy of an impact, while maintaining the impact force transferred to the protected object at a low level. Therefore, it is crucial to accurately characterize the load bearing and energy dissipation performance of foams at high strain rate loading conditions. There are certain challenges faced in the accurate measurement of the deformation response of foams due to their low mechanical impedance properties. In the present work, a non-parametric method is successfully implemented to enable the accurate assessment of the compressive constitutive response of rigid polymeric foams subjected to impact loading conditions. The method is based on stereovision high speed photography in conjunction with 3D digital image correlation, and allows for accurate evaluation of inertia stresses developed within the specimen during deformation time. Full-field distributions of stress, strain and strain rate are used to extract the local constitutive response of the material at any given location along the specimen axis. In addition, the effective energy absorbed by the material is calculated. Finally, results obtained from the proposed non-parametric analysis are compared with data obtained from conventional test procedures.

4.2 INTRODUCTION

Owing to their superior energy absorption and acoustic characteristics, rigid polymeric foams are widely used in the aerospace and automotive industries. In addition to energy dissipation performance, advanced polymeric foams are also gaining attention in structural components, as well as the core material for strengthening hollow structures while maintaining the overall structural weight at low levels [1-3]. The enhanced energy dissipation properties of polymer foams are mainly due to their low mechanical impedance, whereas such low impedance is itself a direct result of the porous structure of these materials. Although the low impedance behavior makes polymeric foam the material of choice in applications where dynamic loading conditions are dominant, it makes characterization of the dynamic behavior of foams more challenging compared with solid non-porous structures. The main challenge is due to the relatively low elastic wave speed in these materials which results in a delayed state of stress equilibrium during loading [4]. There have been solutions proposed to compensate for the belated state of equilibrium in dynamic loading conditions, most of which are only applicable in studies utilizing split Hopkinson pressure bars (SHPB). Application of hollow and/or polymeric bars to reduce the impedance mismatch between bars and specimen [5-7], and pulse shaping techniques [8, 9] are the most common solutions proposed to tackle the challenges in dynamic testing of foams in SHPB.

There have been several studies focusing on experimental characterization of direct impact response of polymeric foams [10-12]. In direct impact loading, none of the above-mentioned solutions are applicable since the basis of the experimental approach is on the direct measurement of the applied impact force. A more general solution to compensate for the non-equilibrium stress condition in direct impact experiments is the use of short specimens [13]. The main benefit in using short specimens in direct impact studies is due to the significant reduction of the elastic wave reverberation time in order to achieve the quasi-static equilibrium in a shorter time. However, in the case of cellular materials, there exists a lower bound on the dimensions of the specimen subjected to impact testing due to the representative volume element (RVE) size required to maintain the continuum response of the material [14-16].

The challenges listed above call for a more general approach that (a) is independent of the specimen dimensions; (b) facilitates accurate assessment of the dynamic deformation response of the foam even where non-equilibrium stress conditions are present. Recent advances in high speed photography and full-field measurements have provided a path for more accurate study of the dynamic deformation of low impedance materials. In particular, recent advances in inverse identification of the constitutive response of materials have been established to be promising approaches providing accurate assessment of the high strain rate deformation response. The basic idea in the area of inverse identification from full-field measurement is the use of kinematics of the deformation (displacement and strain) to inversely identify the loads/stresses imposed on the object. The virtual fields method (VFM) is an example of such inverse analyses gaining extensive popularity in the experimental mechanics community [17].

For the specific case of impact loading of low impedance materials, direct identification of the constitutive response based on full-field measurements was proposed by Othman et al. [18], in which the contribution of inertia was also included in the analysis by computing the full-field acceleration developed in the impacted specimen. The same approach was implemented to study the direct impact response of various polymer foams at strain rates of up to 2500 s^{-1} [19, 20]. Our objective in the present work is to extend the previous idea by adopting the same non-parametric analysis to study the energy absorption characteristics of closed-cell polymeric foams subjected to intermediate-velocity direct impact. The term “intermediate-velocity” indicates that the impactor velocity is sufficiently high so that a static analysis may not be justified. In this range, the initial inertia forces are of considerable magnitude [21]. On the other hand, the impactor velocity is not high enough to significantly increase the influence of elastic wave and shock wave propagations in the material, therefore the term “intermediate-velocity” is adopted. The novel contribution in the present study is the consideration of dynamic deformation of the foam during loading and unloading in the analysis. Accordingly, impact experiments were designed in a way that a relatively large magnitude of plastic strain (>20%) is imposed on the specimens without causing total failure. Full-field displacement is used to determine the distribution of acceleration over the entire length of the specimen. Inertia stresses are computed from the acceleration, and then superimposed with the boundary-measured stress to determine the total axial stress magnitudes. A complete stress-strain hysteresis loop is acquired, enabling the study of energy dissipation characteristics of the utilized material.

4.3 MATERIAL AND SPECIMEN GEOMETRY

High density closed-cell polyurethane foam under the commercial name TufFoam35 was examined in this work [22]. Nominal bulk density of the as-received foam was measured in-house as 560 kg/m^3 (35 pcf). Bulk density determinations were based on the measurement of mass per unit volume of the as-received foam billets. Cellular structure of the material is presented in Figure 4.1, exhibiting circular cells with a 150 μm average diameter and 150 μm cell-wall thickness. Elastic modulus of the foam at quasi-static conditions was measured in-house as 780 MPa. Cylindrical specimens of 28.8 mm in length and 25.3 mm in diameter were extracted from the as-received foam billet by the use of a hole saw. The application of hole saw results in a smooth lateral surface finish with ±0.1 mm dimensional accuracy. For image correlation purposes, a high contrast speckle pattern comprised of a black substrate with 80 μm white particles was applied on the lateral surface of the specimen. Speckling was carried out using normal flat spray paints.

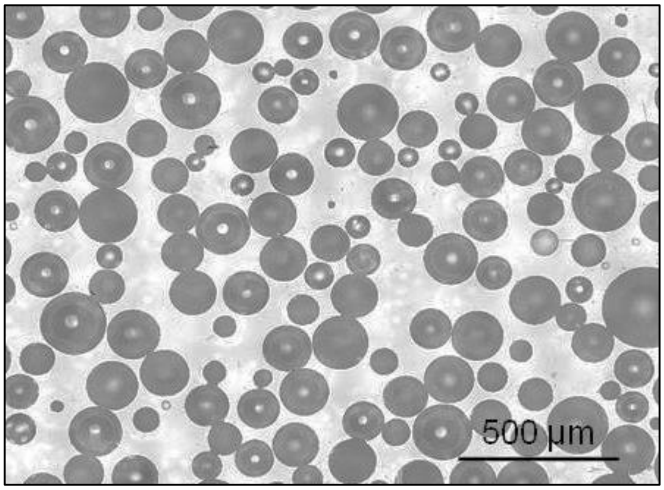

Figure 4.1 Cellular structure of the examined foam.

4.4 DIRECT IMPACT EXPERIMENTS

Controlled direct impact was applied to the specimen using a shock tube apparatus. Details on the design aspects of the shock tube are beyond the scope of this work, but can be found elsewhere [19, 23]. The schematic representation of the utilized shock tube is depicted in Figure 4.2. The speckled specimen was inserted on a custom fabricated fixture close to the muzzle of the shock tube. The custom fixture incorporates a piezoelectric load-cell, facilitating measurement of the reaction force at the rear side of the specimen. The load-cell used in this work was an 88.8 kN capacity PCB piezotronics® load-cell, designed primarily for impact force measurements. The specimen was placed in its position on the fixture with the use of lithium grease, which also serves as a lubricant to diminish the effect of friction.

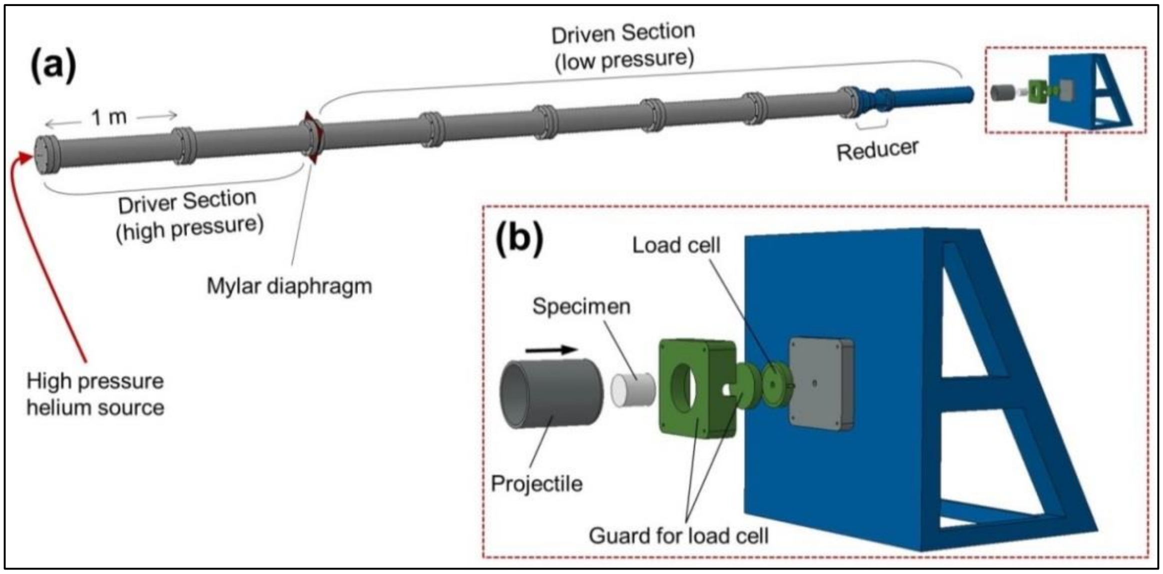

Figure 4.2 Schematic of the shock tube in its entirety, with a magnified view of the load fixture depicted in (b).

To increase the momentum transfer to the specimen and achieve higher strain rates, a 0.07 kg aluminum projectile was placed inside the tube and shot directly at the foam. Velocity of the projectile at the tube exit can be manipulated by varying the number and/or thickness of the plastic diaphragms used to separate the driver and the driven sections of the shock tube (see Figure 4.2). In the present work, projectile velocity of 40.4 m/s was achieved by using a plastic diaphragm with 0.1 mm total thickness. The uncertainty level in the projectile velocity in this work is ±5%, corresponding to ±2 m/s. Impactor velocity was measured upon the exit of the aluminum projectile from the muzzle of the tube, just before the establishment of the impact. More details on the projectile velocity measurement can be found in [20]. The projectile velocity regarded here falls well within the range of intermediate velocity impact for the case of the foam studied in this work. Impact experiments were designed in such a way that the material will deform up to a global strain at which surface cracks are visibly formed on the lateral surface of the specimen. Reproducibility of the results was confirmed by conducting at least three independent experiments following the exact same experimental procedure. Once the repeatability was confirmed, results of the best experiment were extracted and presented in this work.

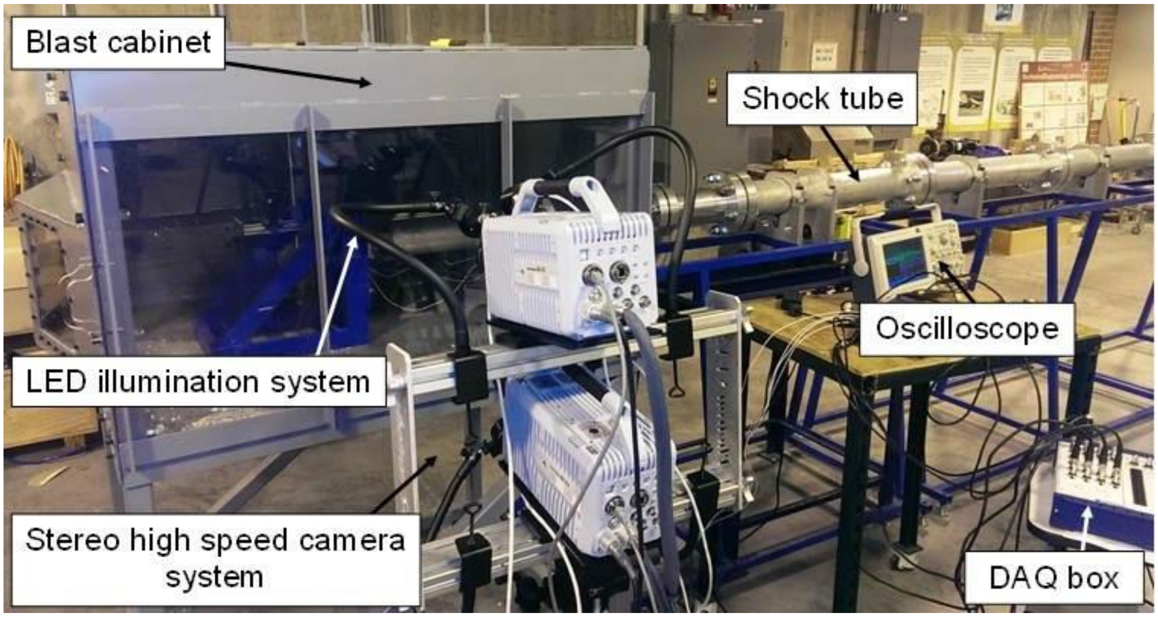

Figure 4.3 Experimental setup showing the shock tube and the stereovision camera system.

4.5 HIGH SPEED IMAGING AND DIGITAL IMAGE CORRELATION

High speed stereovision imaging in conjunction with digital image correlation was used in order to analyze and quantify the deformation of the impacted specimens. The imaging setup was composed of a pair of high speed Photron SA-X2 cameras each equipped with a 100 mm macro lens. The cameras were mounted vertically in a custom made fixture, acquiring images from the lateral surface of the impacted foam specimen, as seen in Figure 4.3. Cameras were triggered by the use of the signal sent from the oscilloscope attached to the load-cell. Connection of the cameras to the oscilloscope in this work facilitates synchronization of the load-cell data collection with the image acquisition rate. Stereo images were collected at a rate of 150,000 frames per second at full-field resolution of 256×216 pixel^2. Images acquired during deformation stage were processed and analyzed in the image correlation software Vic-3D (Correlated Solutions, Inc.). Details of the image correlation process are listed in Table 4.1.

The default Cartesian coordinate system of the measurements in Vic-3D was switched to the cylindrical coordinate systems using the built-in coordinate tool in the software Vic-3D. Distribution of the full-field displacement and strain was computed in this software. Temporal derivatives were computed from full-field displacement and strains using simple central difference scheme as:

$$\dot{\varepsilon}_{ij}(t)=\frac{\varepsilon_{ij}(t+\Delta t)-\varepsilon_{ij}(t-\Delta t)}{2\Delta t} \tag{4.1}$$

$$v_i(t)=\frac{u_i(t+\Delta t)-u_i(t-\Delta t)}{2\Delta t} \tag{4.2}$$

$$a_i(t)=\frac{u_i(t+\Delta t)-2u_i(t)+u_i(t-\Delta t)}{\Delta t^2} \tag{4.3}$$

where u_i and ε_{ij} denote the components of the displacement and strain, respectively. Parameters $\dot{\varepsilon}_{ij}$, v_i and a_i represent strain rate, velocity and acceleration, respectively. Δt is the interframe time (= 6.67 μs).

Table 4.1 Image acquisition and correlation parameters used in the present study

Camera system	Photron SA-X2 (×2)
Frame rate	150,000 fps
Interframe time	6.67 μs
Exposure time	293 ns
Image resolution	256×216 pixel^2
Pixel-to-length ratio	7.75 pixel/mm
Full-field measurement technique	3D DIC (Vic-3D)
Subset	21×21 pixel^2
Step	1 pixel
Strain filtering (filter size)	Gaussian (15)
Temporal smoothing	None
Matching criterion	Normalized squared differences
Interpolation	Optimized 8-tap interpolation
Shape function	Affine
Strain resolution	480 με
Acceleration resolution	2×10^3 m.s^{-2}

4.6 DATA ANALYSIS

The objective in this work is to take the effect of inertia loading during dynamic deformation of the foam specimen into account. This goal is achieved through the application of the non-parametric analysis introduced in [18-20]. In this approach, the inertia stress is calculated from the full-field data obtained from DIC. The first step in this approach is to consider the general dynamic stress equilibrium, expressed as:

$$\sigma(z,t) = \sigma^{boundary} + \sigma^{inertia} \tag{4.4}$$

where:

$$\sigma^{boundary} = \sigma(0,t) \quad \text{and} \quad \sigma^{inertia} = \int_{\xi=0}^{\xi=z} \rho(\xi,t) a(\xi,t) d\xi \tag{4.5}$$

Eq. (4.4) is a direct solution of the equation of stress equilibrium in the absence of body forces and shear stresses, and states that the value of the axial stress, σ, at location z and time t can be evaluated using the stress measured at specimen end, i.e. $z = 0$, plus the inertia stress [18-20]. The inertia stress is expressed by the integral term in Eq. (4.5) as a function of the spatial variation of density, ρ, and axial acceleration, a. This inertia stress can be evaluated from the full-field data. Using the full-field distribution of acceleration and density, the integral term in Eq. (4. 5) can be approximated by a simple summation as:

$$\int_{z=0}^{z=L} \rho(z,t) a_z(z,t) dz \approx \sum_{i=1}^{n} \rho_{(i)} a_{(i)} s_{(i)} \tag{4.6}$$

where, $\rho_{(i)}$ and $a_{(i)}$ represent the average values of density and axial acceleration in section i. The term $s_{(i)}$ denotes the thickness of section i, as illustrated in Figure 4.4. Variation of material density in time and space is included in this approach by using a recently proposed model [20] that enables the calculation of local instantaneous density as a function of initial density, ρ_0, local Poisson's ratio, $v(z, t)$, and local axial strain value, $\varepsilon(z,t)$, expressed as:

$$\rho(z,t) = \rho_0 \left[\exp(\varepsilon(z,t))\right]^{2\upsilon(z,t)-1} \tag{4.7}$$

Having obtained the variations of axial acceleration and material density in time and space, inertia stress at any desired location along the length and at any given time can be evaluated using Eq. (4.6). Superimposing this inertia stress with the boundary measured stress, local axial stress along the specimen length can be determined from Eq. (4.4). The stress values calculated from Eq. (4.4) are synchronized with the axial strain values, as the load data collection and image acquisition are initiated at the same instant and carried out at the same rate; therefore, local stress-strain curves at any given position along specimen length can be extracted.

Specific energy (energy per unit volume) can be determined from the area below the global stress-strain curve. To evaluate the specific energy consumed by the foam specimen in this work, average stress-strain curves are considered first. Spatially averaged stress and strain values are calculated as:

$$\overline{\sigma(t)} = \frac{\int_0^{L(t)} \sigma(z,t)dz}{L(t)} \tag{4.8}$$

$$\overline{\varepsilon(t)} = \frac{\int_0^{L(t)} \varepsilon(z,t)dz}{L(t)} \tag{4.9}$$

where $\overline{\sigma(t)}$ and $\overline{\varepsilon(t)}$ are the spatially-averaged axial stress and axial strain, respectively. In case of the application of full-field data, spatial averaging can be carried out using simple numerical integration. Having obtained synchronized values for $\overline{\sigma(t)}$ and $\overline{\varepsilon(t)}$, average stress-strain curve of the specimen can be generated by plotting $\overline{\sigma}$ versus $\overline{\varepsilon}$. Finally, the specific energy of the specimen, *W*, can be determined as:

$$W = \int_0^{\bar{\varepsilon}} \bar{\sigma} d\bar{\varepsilon} \tag{4.10}$$

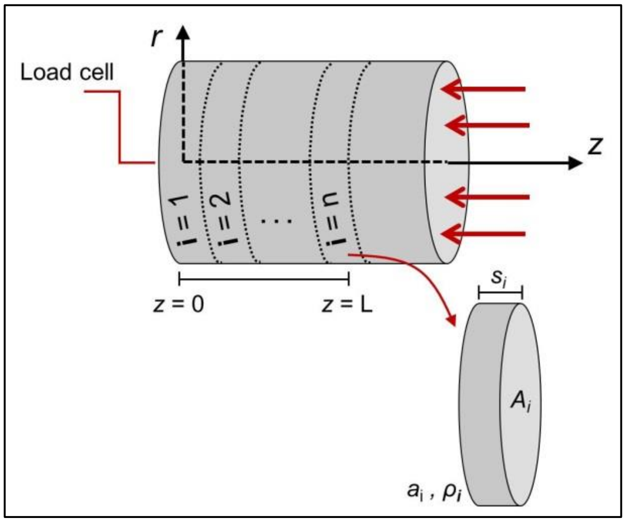

Figure 4.4 Cylindrical specimen sliced into a finite number of thinner sections, used to calculate the inertia stress applied at each point along the specimen axis.

4.7 NOMINAL STRESS-STRAIN CURVE

Figure 4.5 shows 20 gray level images recorded during loading and unloading of the specimen. Physical dimensions of each individual grey-scale image in Figure 4.5 are approximately 33×28 mm^2, covering the entire length of the specimen. The reference time t=0 μs indicates the instant at which the contact between specimen and the projectile is established. It is shown that the specimen is loaded in compression during the first 400 μs after the impact. Unloading of the specimen occurs after t≈400 μs, as clearly indicated in Figure 4.5 by the gradual movement of the projectile to the right side.

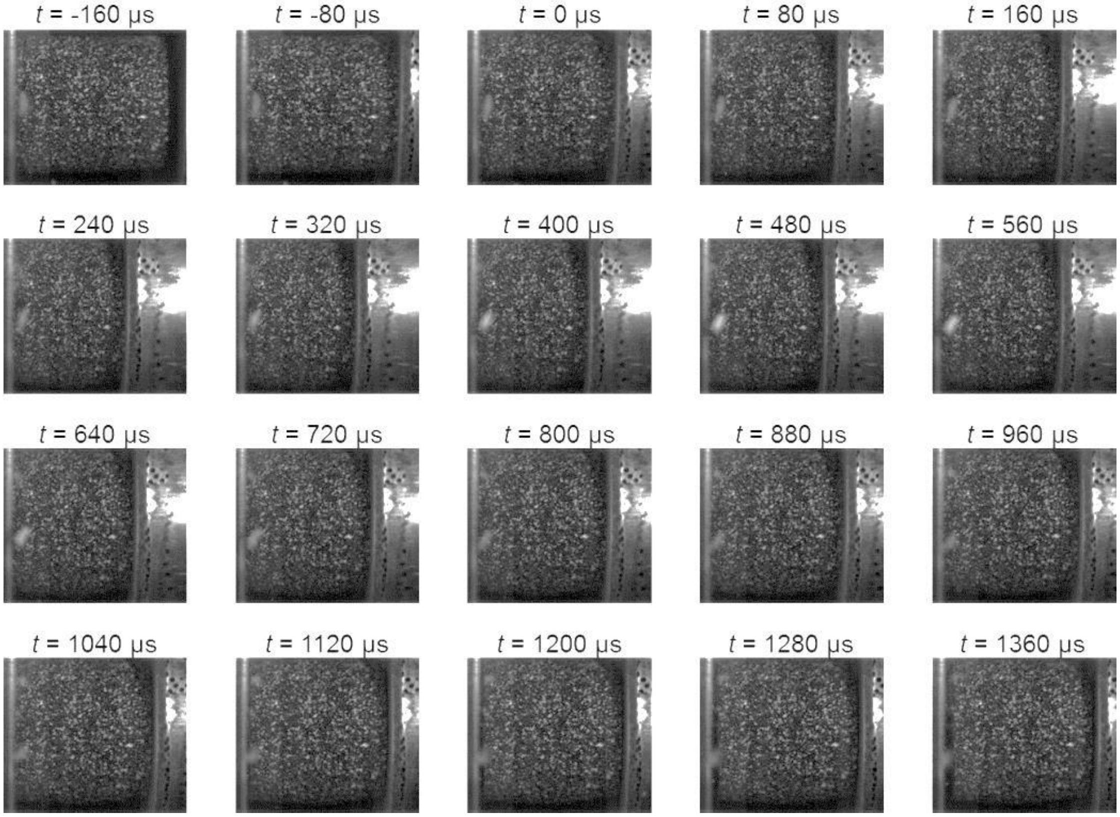

Figure 4.5 Gray level images. t = 0 µs indicates the moment of impact.

Variation of specimen length with time was calculated from the displacement of the impacted side. Figure 4.6 depicts the variation of specimen length, along with the boundary-measured reaction force. Note that the reaction force is compressive, but is plotted in Figure 4.6 as a positive quantity for convenience. Also for convenience, the term “reaction force” is replaced by the “boundary-measured force” hereafter. Variation of the specimen length shows a progressive decrease in the first 65 images recorded after the impact, reaching a minimum at t≈433.34 µs. On unloading, the specimen length starts to increase again to reach a final value of 26.6 mm after complete unloading. The boundary-measured force also indicates a sharp rise in the first 30 µs after the impact, and remains relatively constant for a duration of ~420 µs, followed by a gradual decrease during the unloading stage. Using the boundary measured force and displacement, engineering (nominal) stress-strain curve was extracted and is plotted in Figure 4.7. The engineering stress here is simply determined by dividing the boundary-measured force by the original cross sectional area. Engineering strain was calculated as the ratio of the change in specimen length (ΔL) and the original length (L_0). Note that the engineering stress-strain curve here is regarded as the conventional approach, since the calculation of true stress requires the determination of instantaneous cross sectional area, a concept that may not be accurately achieved in case of compressible closed-cell foams with considerable radial expansion. In this regard, in the case of compressible cellular solids such the one studied in this work, volume constancy is not a valid assumption and, therefore, the true stress values cannot be directly calculated using the correlation between the instantaneous length and cross sectional area.

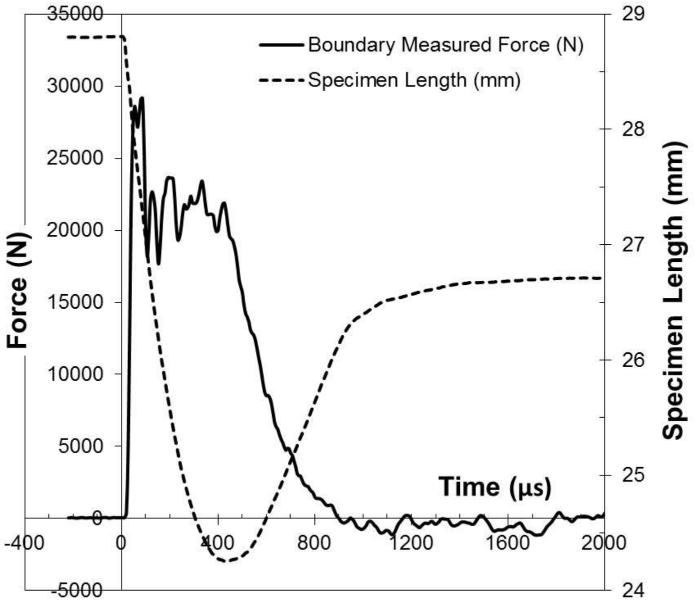

Figure 4.6 Variation of boundary-measured force and specimen length in time.

The nominal stress-strain curve in Figure 4.7 indicates a noticeable plateau at the beginning of the curve. The small plateau seen here is attributed to the delayed state of stress equilibrium at the early stages of deformation [19]. In this transient duration, there has not been sufficient time for the stress wave to traverse the entire length of the specimen and reach the load-cell side; however, the deformation has already initiated from the impacted side. Consequently, deformation occurs in the specimen before the force can be recorded by the load-cell. Except the small plateau observed at early deformation time, engineering stress-strain curve plotted for the impacted specimen is typical of the constitutive response documented for closed-cell foams under compression [11]. The curve exhibits three distinct regions. At small nominal strains (<3%) the material exhibits linear elastic response. Gradual collapse of the cell structure at larger nominal strains progresses at relatively constant nominal stress, indicating a stress plateau over an engineering strain range of 6% to 15%. During the unloading phase, the stress decreases non-linearly with the strain, resulting in a progressively decreased slope. Finally, a residual permanent nominal strain of ~9% is retained in the specimen after complete unloading. The lower apparent slope during unloading is attributed to cellular scale damage and the formation of cracks in the specimen. Figure 4.8 illustrates the photograph of the vertically-sectioned deformed specimen, evidencing the formation of small visible cracks inside the impacted specimen. Note that the material examined in this work does not exhibit any significant densification stage in its nominal stress-strain curve.

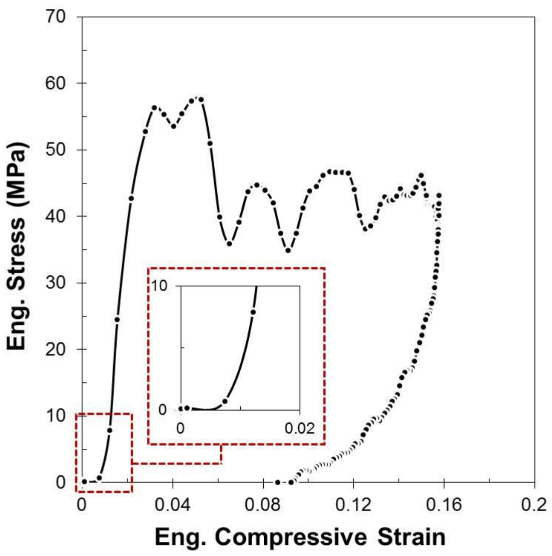

Figure 4.7 Engineering (nominal) stress-strain curve during loading and unloading, calculated from boundary-measured force and specimen length.

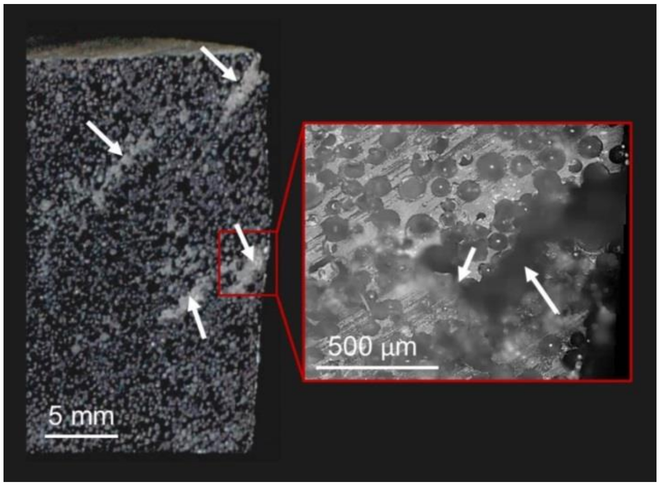

Figure 4.8 Photograph showing the vertical section of the specimen after deformation. Arrows mark visible cracks.

4.8 DEFORMATION ANALYSIS BASED ON FULL-FIELD MEASUREMENTS

Full-field distribution of axial displacement during the loading time is shown in Figure 4.9. The area over which full-field results are shown covers >85% of the entire domain of interest (speckle pattern). Contour maps in Figure 4.9 show relatively uniform axial displacement distribution in the hoop direction, indicating insignificant shear deformation during the impact tests in this work. Accordingly, the analysis was proceeded based on the formulations proposed for the uniaxial stress state.

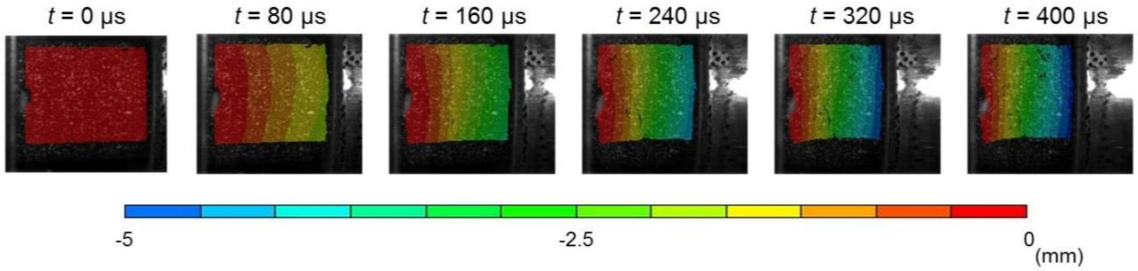

Figure 4.9 Contour maps showing the full-field distribution of axial displacement at selected times after the impact. t=0 μs indicates the instant of impact.

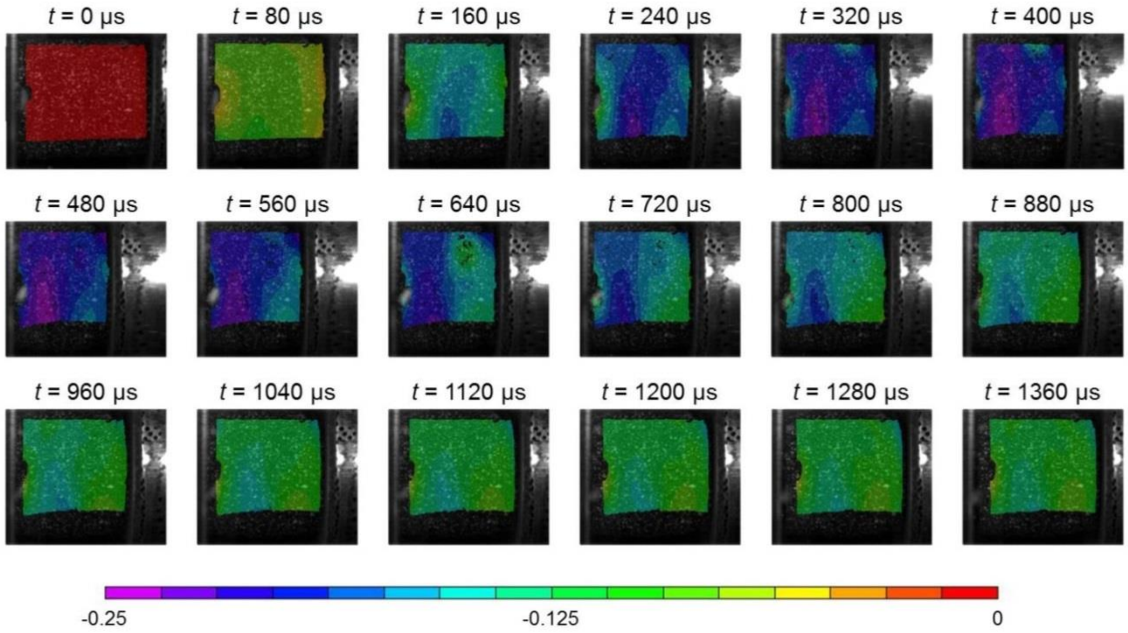

Figure 4.10 Contour maps showing the full-field distribution of axial strain at selected times after the impact.

Distribution of axial strain over the entire area of interest is shown in Figure 4.10. Strain maps in Figure 4.10 exhibit the formation of relatively uniform axial strain value in the hoop direction. On the other hand, the axial strain varies along the specimen length, clearly showing high strain region formed over the middle sections of the specimen. The presence of high strain domains in the middle length of the specimen is due to boundary effects. Friction at specimen ends can partially restrain the lateral expansion of the specimen in the vicinity of the two ends, resulting in larger deformation concentration at middle sections. This statement is supported by observing radial strain maps in Figure 4.11, where larger radial strains are shown to have developed in the middle length of the specimen.

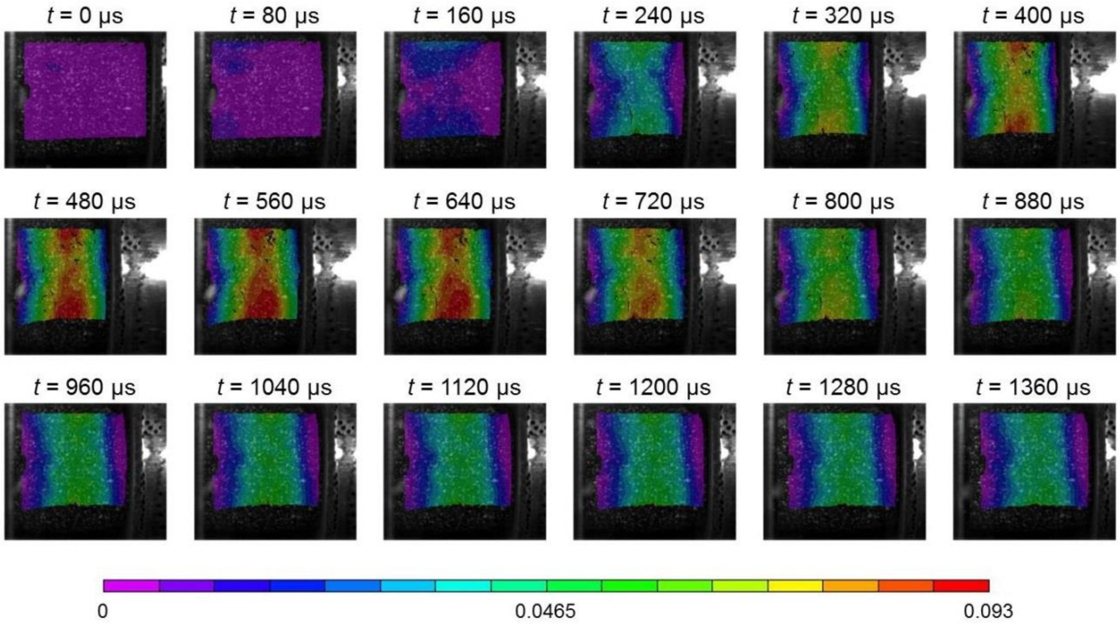

Figure 4.11 Contour maps showing the full-field distribution of radial strain at selected times after the impact.

Axial strain rate applied on the specimen was determined by differentiating the spatially-averaged axial strain values with respect to time. Figure 4.12 shows the variation of axial strain rate with time. A maximum average compressive strain rate of 1000 s^{-1} was applied to the specimen at the time of peak load. The strain rate curve then shows a gradual decrease and changes sign at t=400 μs. This sign change is due to the reversion of acceleration and is discussed in detail later in this section. The strain rate remains zero after t=1100 μs, i.e. the instant of complete unloading. Note that the error bars in Figure 4.12 indicate the standard deviation of the entire population of strain rate data within the area of interest. This standard deviation here may be used as measure for the spatial variability of axial strain rate, confirming a maximum 150 s^{-1} spatial variation in the axial strain rate values along the specimen axis during the loading stage, i.e. 0<t<400 μs.

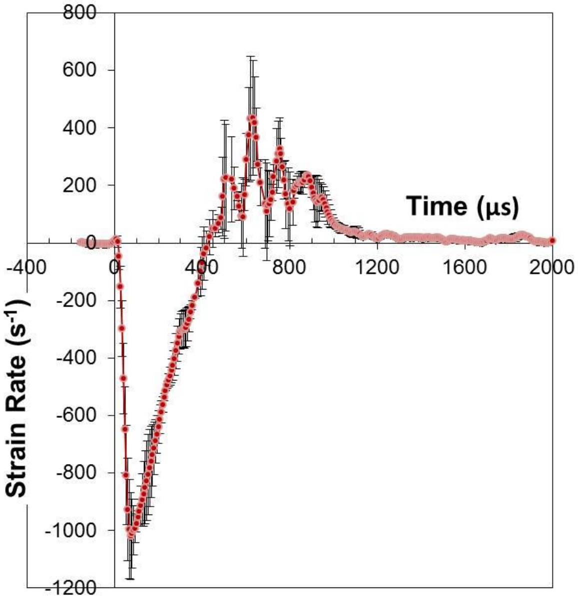

Figure 4.12 Variation of strain rate in time. Error bars indicate the spatial variability of strain rate.

Using the local evolutions of axial and radial strains, the apparent Poisson's ratios at various locations along specimen axis was estimated following the procedure detailed in [19]. Figure 4.13 shows the variation of local radial strain with axial strain extracted from five representative sections along the specimen axis. It is clearly seen that the Poisson's effect varies considerably along specimen length, indicating different apparent Poisson's ratios. Poisson's ratios extracted from different sections are detailed in Table 4.2. As expected, higher Poisson's ratios are obtained at sections located mostly on the middle length of the specimen. On the other hand, the Poisson's ratio values shown in Table 4.2 are all less than 0.5. This confirms that the material undergoes partial bulk compression resulting in an increase in density. This compressible response observed here makes the conventional calculation of true stress-strain response of the material challenging. The challenge here will be due to the impractical use of the concept of volume constancy in establishment of a correlation between the specimen length and its cross sectional area.

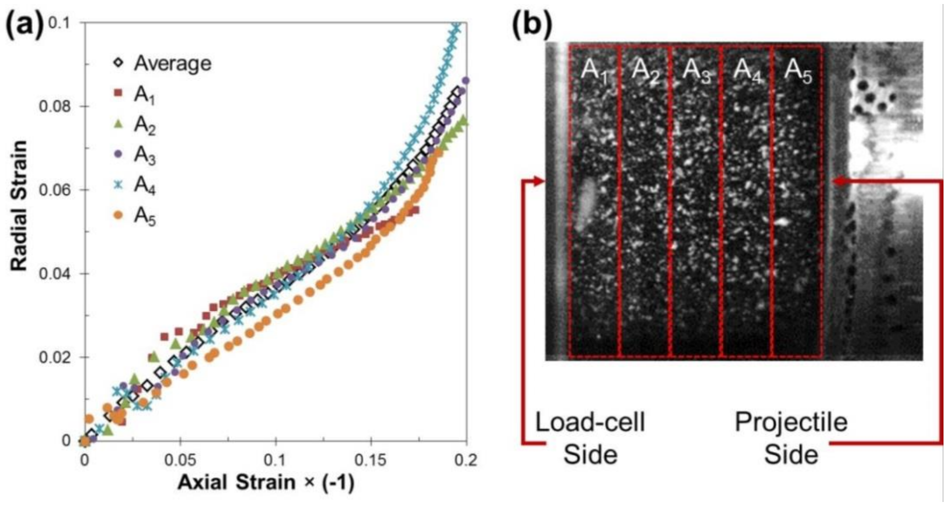

Figure 4.13 (a) Variation of local radial strain with axial strain extracted from five representative sections shown in (b).

Table 4.2 Poisson's ratios extracted from different sections shown in Figure 4.13b

Section	A_1	A_2	A_3	A_4	A_5	Average
Poisson's ratio	0.358	0.382	0.426	0.407	0.329	0.386

Variation of density with time was determined using Eq. (4.7). Figure 4.14 depicts the variation of local density at various locations along the specimen axis. All curves indicate an initial increase associated with the loading stage, followed by a drop as the result of unloading and deformation recovery. The density curves reach a plateau after $t \approx 1100$ µs. Maximum local change of density occurs on A_1 and A_5, i.e. the representative sections located near to specimen ends. This is due to the relatively smaller lateral expansions that occurred within areas more closely associated with the specimen boundary, on which lower Poisson's ratios were also observed (see Table 4.2). On the other hand, a relatively smaller change of density is indicated on sections A_3 and A_4, where higher radial expansions were determined (see Figure 4.11). The average density as a function of time was determined for the material, showing a maximum of ~5% increase in density at the peak load. This average density change was later used along with Eq. (4.6) to facilitate the calculation of inertia effects based on boundary measured data.

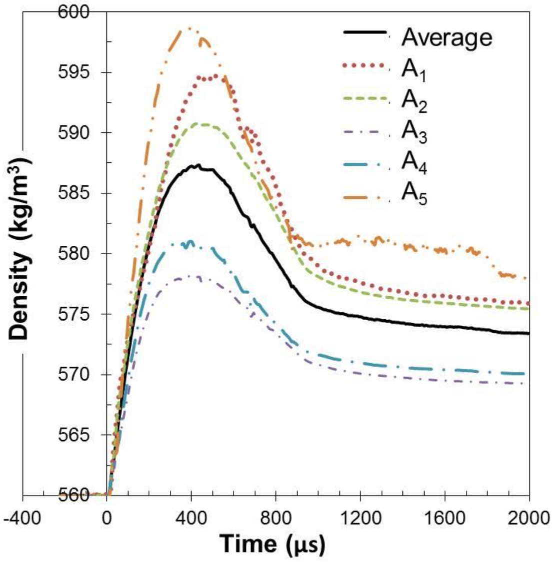

Figure 4.14 Variation of local density in time for the representative sections shown in Figure 4.13b.

Curves showing local evolution of axial acceleration are plotted in Figure 4.15. All local curves show a sudden drop during the first 30 μs after the impact. This is followed by a sharp deceleration and a sign change occurred at t=50 μs. The oscillations observed in the axial acceleration curves is attributed to the elastic wave reverberation along specimen axis. Based on the elastic modulus of the material measured at quasi-static conditions (E=780 MPa), the time required for the stress equilibration was determined as 73.2 μs. This characteristic time is equivalent to the time required for three consecutive reverberations of the elastic wave in the material [24], which is also found to be equal to the time of sharp variations in the acceleration curves during the first ~75 μs after the impact. Acceleration curves indicate slight change in value after the transient duration (i.e. after t≈75 μs). Further oscillations seen in the acceleration curves are basically due to the numerical noise sourced from the temporal noise in the displacement data.

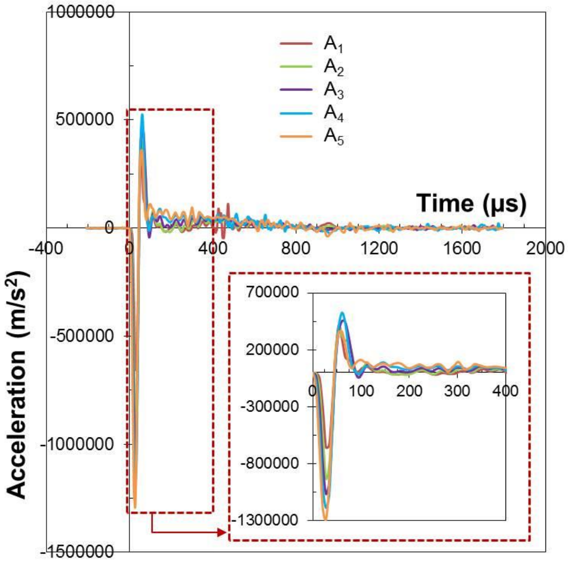

Figure 4.15 Variation of local axial acceleration with time, extracted from the representative locations shown in Figure 4.13b.

The significant variations observed in the local acceleration response of the material result in the development of substantial inertia stresses in the specimen. This inertia stress was calculated from the spatial length-wise variation of acceleration and density, as discussed earlier in Eq. (4.5). Figure 4.16 shows the variation of inertia stress along the specimen length calculated at different times after the impact. The magnitude of the inertia stress is shown to be highest at the impacted side of the specimen at all times. This observation is consistent with the acceleration curves shown earlier in Figure 4.15, in which the highest accelerations were found to develop over the regions more closely associated with the impacted side of the specimen. Another point worth noting is that the inertia stresses developed in the specimen remain compressive (negative) during the first 50 μs after the impact. During this time, the compressive inertia stresses add up to the compressive boundary-measured stress and increase the overall axial stress magnitude applied on the specimen at any given location along its axis. Afterwards, on reversion of the axial acceleration, inertia stresses will become tensile (positive) and tend to decrease the overall stresses in the specimen by cancelling out some portion of the compressive stress measured at the specimen end.

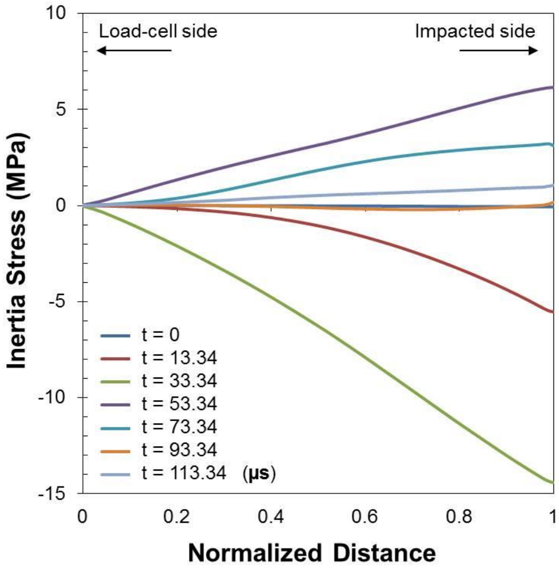

Figure 4.16 Variation of inertia stress with respect to the normalized length of the specimen at different instants after impact, determined using full-field data.

Superimposing the obtained inertia stress with the true stress measured at the specimen boundary, local evolution of total axial stress can be evaluated. Figure 4.17 shows the variation of total axial stress with time. Note that, for convenience, the compressive stresses are plotted in positive values hereafter. Substantial length-wise variability in total stress is observed during the initial 100 μs time after the impact. The degree of such spatial variability tends to reduce at longer durations, as the damping of the acceleration occurs and the state of quasi-static stress equilibrium is achieved. Similarly, local length-wise variation of strain can be readily extracted as a direct output of the image correlation analysis, finally facilitating the extraction of local stress-strain curves at different locations along the specimen length. The local stress-strain curves can be averaged using Eqs. (4.8) and (4.9) to give an effective average constitutive response for the material.

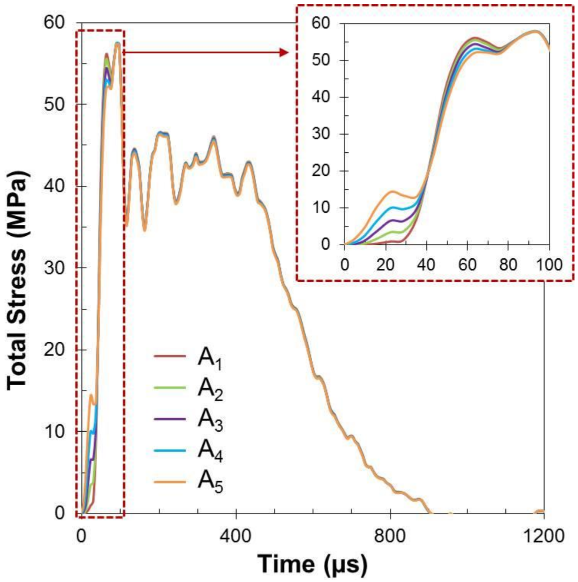

Figure 4.17 Variation of total (inertia plus boundary measured) stress with time at different locations in specimen length.

Figure 4.18 illustrates the effective stress-strain curve obtained by averaging all the local curves extracted along the specimen axis. Comparing Figure 4.18 with the nominal engineering stress-strain curve shown earlier in Figure 4.7, there is noticeable difference between the two curves at the early stages of deformation. In particular, the delayed stress rise time is no longer present in the curve obtained from the full-field approach. This is indeed expected here since the influence of inertia and the non-equilibrium state of stress are already accounted for in the non-parametric approach. Finally, the stress-strain curve shown in Figure 4.18 gives a more realistic measure for the actual constitutive response of the examined material. This can be further confirmed by extracting the slope of the curve at the elastic deformation regime. The elastic modulus determined from the curve presented in Figure 4.18 is 810 MPa, the value of which is slightly higher than the elastic modulus of the material measured at quasi-static loading conditions, i.e. 780 MPa. The increased elastic modulus measured from data presented in Figure 4.18 can be justified through the visco-elastic nature of the material employed here. Note that, conventionally, due to transient state of deformation at the early stages of the dynamic loading, measuring elastic modulus at high strain rate is impossible. For example, applying the same procedure on the nominal stress-strain curve shown in Figure 4.7 results in an elastic modulus of <200 MPa, which is significantly lower than the quasi-static modulus of the material, and thus may not be regarded as a reliable value. However, in the current work, the dynamic equilibrium was considered from the beginning of the loading by accounting for the inertia stress, which makes the analysis significantly more reliable.

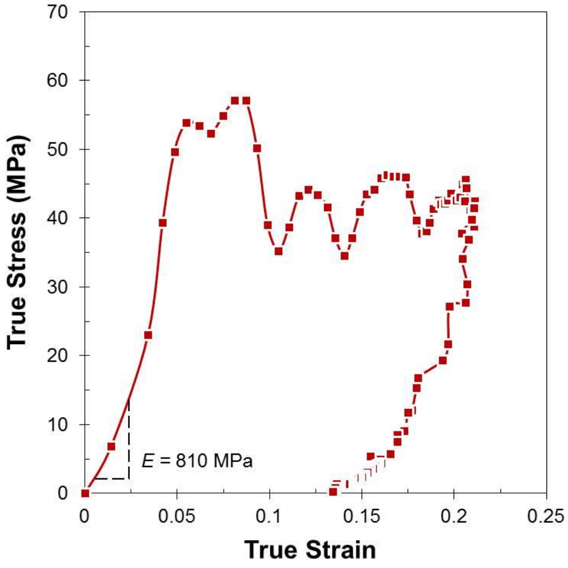

Figure 4.18 True stress-strain curve during loading and unloading, calculated from full-field data.

Another significant difference in the stress-strain curves obtained using conventional and full-field approaches is that the conventional methodology assumes uniform strain distribution along gauge area, and therefore does not take the influence of any local deformation into account. On the other hand, the stress-strain analysis based on the full-field measurement does include the effects due to local deformation. The experimental observation depicted in Figure 4.10 clearly confirms that the strain is not uniform across the length of the specimen.

Finally, the specific energy absorbed by the material calculated based on the two methods, i.e. conventional and the full-field stress analysis, are compared in Figure 4.19. To this purpose, the area below stress-strain curve was evaluated as the specific energy magnitude absorbed during a full loading-unloading cycle. As shown in Figure 4.19, the value of specific energy calculated using the full-field data is significantly higher compared with the value calculated following conventional method. The specific energy calculated from the conventional method is lower by 20%. This is again due to the fact that, by accounting the local deformation, compressibility and inertia, the full field method helps to determine more realistic constitutive response of the material.

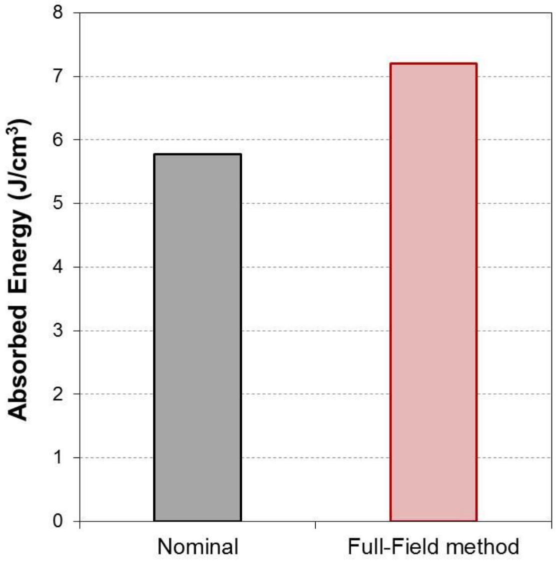

Figure 4.19 Comparing specific energy values determined from two different methods.

4.9 CONCLUSIONS

Constitutive and energy performance response of closed-cell polymeric foams subjected to intermediate-velocity impact were studied. Controlled direct impact was applied to foam specimens and the stress-strain response was investigated by two different methods. Nominal stress-strain response was first evaluated using simple definitions of engineering stress and engineering strain. It was shown that the nominal stress-strain response is incapable of predicting the accurate constitutive response of the foam, due to limitations associated with transient stress state, material compressibility and local length-wise variation of axial and radial strains. The deformation analysis of the impacted foam was also conducted using full-field measurements facilitated by the use of high speed photography and 3D digital image correlation. The analysis performed based on the full-field deformation measurements was shown to be able to accurately predict the deformation response of the material accounting for inertia loading, material compressibility and the spatial variation of strain. Specific energy absorbed during a complete loading-unloading cycle was determined using the two methods. It was shown that the application of conventional methodology, i.e. considering nominal stress-strain response, can underestimate the energy absorption characteristics of the polymeric foam specimen by 20%.

4.10 LIST OF REFERENCES

[1] Gibson LJ, Ashby MF. Cellular solids: Structure and properties. 2nd ed. Oxford. 1997.

[2] Gardner N, Wang E, Kumar P, Shukla A. Blast mitigation in a sandwich composite using graded core and polyurea interlayer. Experimental Mechanics 2012; 52: 119-133.

[3] Koohbor B, Kidane A. Design optimization of continuously and discretely graded foam materials for efficient energy absorption. Materials and Design 2016; 102: 151-161.

[4] Zhao H. Testing of polymeric foams at high and medium strain rates. Polymer Testing 1997; 16: 507-516.

[5] Yunoshev AS, Sil'vestrov VV. Development of the polymeric split Hopkinson bar technique. Journal of Applied Mechanics Technical Physics 2001; 42(3): 558-564.

[6] Chen W, Zhang B, Forrestal MJ. A split Hopkinson bar technique for low-impedance materials. Experimental Mechanics 1999; 39(2): 81-85.

[7] Kidane A. On the Failure and Fracture of Polymer Foam Containing Discontinuities. ISRN Materials Science 2013, DOI:10.1155/2013/408596.

[8] Chen W, Lu F, Winfree N. High strain rate compressive behavior of a rigid polyurethane foam with various densities. Experimental Mechanics 2002; 42(1): 65-73.

[9] Song B, Chen W, Frew DJ. Dynamic compressive response and failure behavior of an epoxy syntactic foam. Journal of Composite Materials 2004; 38(11): 915-936.

[10] Zhang J, Kikuchi N, Li V, Yee A, Nusholtz G. Constitutive modeling of polymeric foam material subjected to dynamic crash loading. International Journal of Impact Engineering 1998; 21(5): 369-386.

[11] Avalle M, Belingardi G, Montanini R. Characterization of polymeric structural foams under compressive impact loading by means of energy-absorption diagram. International Journal of Impact Engineering 2001; 25: 455-472.

[12] Ouellet S, Cronin S, Worswick M. Compressive response of polymeric foams under quasi-static, medium and high strain rate conditions. Polymer Testing 2006; 25: 731-743.

[13] Ouellet S, Cronin DS, Moulton J, Petel EO. High rate characterization of polymeric closed-cell foams: Challenges related to size effects. In: Chalivendra V, Song B, Casem D (Editors), Dynamic behavior of materials – Volume 1, Proceedings of the 2012 Annual Conference on Experimental and Applied Mechanics, Springer, 2013, pp 21-28. DOI 10.1007/978-1-4614-4238-7_4

[14] Kanaun S, Tkachenko O. Representative volume element and effective elastic properties of open cell foam materials with random microstructures. Journal of Mechanics of Materails and Structures 2007; 2(7): 1607-1628.

[15] Alsayednoor J, Harrison P, Guo Z. Large strain compressive response of 2-D periodic representative volume element for random foam microstructures. Mechanics of Materials 2013; 66: 7-20.

[16] Tekoglu C, Gibson LJ, Pardoen T, Onck PR. Size effects in foams: Experiments and modeling. Progress in Materials Science 2011; 56: 109-138.

[17] Pierron F, Grédiac M. The virtual fields method: Extracting constitutive mechanical parameters from full-field deformation measurements. Springer, NY, 2012.

[18] Othman R, Aloui S, Poitou A. Identification of non-homogeneous stress fields in dynamic experiments with a non-parametric method. Polymer Testing 2010; 29: 616-623.

[19] Koohbor B, Mallon S, Kidane A, Lu W. The deformation and failure response of closed-cell PMDI foams subjected to dynamic impact loading. Polymer Testing 2015; 44: 112-124.

[20] Koohbor B, Kidane A, Lu W, Sutton MA. Investigation of the dynamic stress-strain response of compressible polymeric foam using a non-parametric analysis. International Journal of Impact Engineering 2016; 91: 170-182.

[21] Sjoblom PO, Hatness JT. On low-velocity impact testing of composite materials. Journal of Composite Materials 1988; 22: 30-52.

[22] Lu W. Mechanical characterization of rigid polyurethane foams. Sandia Report 2014: SADN2014-20708.

[23] Mallon S, Koohbor B, Kidane A, Sutton MA. Fracture behavior of prestressed composites subjected to shock loading: A DIC-based study. Experimental Mechanics 2015; 55: 211.-225

[24] Davies EDH, Hunter SC. The dynamic compression testing of solids by the method of the split Hopkinson pressure bar. Journal of Mechanics and Physics of Solids 1963; 11(3): 155-179.

CHAPTER 5

MESO-SCALE STRAIN LOCALIZATION AND FAILURE RESPONSE OF AN ORTHOTROPIC WOVEN GLASS-FIBER REINFORCED COMPOSITE [4]

---

[4] Koohbor B, Ravindran S, Kidane A. *Composites Part B: Engineering* 2015; 78: 308-318. doi:10.1016/j.compositesb.2015.03.064
Reused here with permission of publisher.

5.1 ABSTRACT

The present work focuses on studying the multi-scale deformation and failure mechanisms of an orthogonally woven glass fiber reinforced composite as a function of fiber orientation angle using digital image correlation. The full-field displacement and strain localization are effectively captured at meso-scale. At continuum scale, a remarkable change in mechanical response is observed when the loading axis diverges from principal axes. The variation in the global mechanical response is observed to be most prominent in the change of stiffness and strain at failure. At meso scale, a high degree of local deformation heterogeneity is observed and the level of inhomogeneity is found to be more prominent in case of the 45° off-axis specimens. While fiber-pull out is the major failure mode in the case of specimen loaded parallel to 0° and 90° fiber orientation, the localized shear strain developed in polymer-rich regions is the driving failure cause in the case of 45° off-axis specimen.

5.2 INTRODUCTION

Deformation and failure response of fiber reinforced composites depends not only on the mechanical properties of their constituents but also on the interactions between the two components, i.e. the reinforcing fibers and the softer matrix. The remarkable differences between the mechanical response of the stiffer fibers and compliant matrix can give rise to significant local deformation heterogeneity, particularly in fiber/matrix interface vicinity, often followed by crack nucleation, debonding of fiber/matrix interface or matrix failure. Insufficient adhesion between the fibers and matrix can also increase the risk of local failures in the areas within the matrix confined by reinforcing fibers. This type of failure can also be dominant when highly nonhomogeneous deformation takes place either due to complex loading or boundary conditions during the service life of the composite. Therefore, deeper knowledge of the meso-mechanics and the local deformation response of such materials can contribute to the improvements in safety and design of these structures. So far, numerous numerical studies have been conducted in order to examine the meso-scale mechanical response and local failure mechanisms present during the mechanical loading of textile composites [1-4]. Lomov et al. [1] have reviewed the finite element based approaches developed in meso-scale modeling of textile composites, found in a great body of literature from the early 1990's to 2007. The main focus of this review has been to provide a detailed study on the meso-FE modeling of textile composites, emphasizing on realistic geometrical modeling, meshing strategies and damage detection algorithms. Finally, they proposed a road map in handling different stages of meso-FE analysis that can be applied to different textile reinforcement architectures. Similar approaches have been used in recent years in modeling the meso-scale failure mechanisms of fiber reinforced composites [2-4].

Although there exist extensive experimental works in the literature on characterization of textile composites at macro-scale level, there is a great gap in understanding the deformation and failure mechanisms at smaller length scales. The recent development of full-field measurement techniques, such as digital image correlation (DIC), has made it possible to capture the deformation of a material at different length and time scales, even in the case of complex and heterogeneous materials systems [5] This method has been successfully practiced in the meso-scale study of random, e.g. [6], as well as textile composites [7-12]. For instance, Godara and Raabe [7] used DIC to experimentally investigate the meso-scale deformation of cross woven composites, focusing on the influence of fiber orientation angle. Using qualitative-based analyses of the fracture surface of their specimens, they were able to correlate the local deformation response to the bulk failure mechanism. However in this work, a rather large surface area of 5×40 mm^2 was considered, which effectively reduces the resolution of the local measurements. Lomov et al. [8, 9] have successfully used mesoscopic DIC-based experiments at significantly smaller length scales compared with the one reported by Godara and Raabe [7] on woven textile reinforcements to study the fabric behavior and yarn interaction mechanisms in the material. However, still the area of interest on which the full-field strain measurements have been carried out is >5 mm^2, which limits the application of the utilized experimental methodology only to composite specimens with larger yarn widths. Similar meso-scale digital image correlation has been utilized for characterizing the local mechanical response and damage inspection of fiber reinforced composites in recent works [10-12]. For instance, the local strain accumulation was used by Fard et al. [12] as a criterion to indicate the damage initiation zones. The location of the local deformation heterogeneities captured by DIC was further analyzed using micro-CT scanning for damage characterization of woven CFRP specimens in a research by Ullah et al. [13].

A more detailed survey within the present literature indicates that there exists a lack of a thorough experimental study which (1) investigates the local deformation response of woven composites with sub-millimeter yarn dimensions; and (2) provides more quantitative observations on the local strain fields, that could provide information on the fiber/matrix interaction as well as the damage initiation and bulk failure mechanisms of the material. In light of this, the present work was conducted with the purpose of studying the macro and meso-scale deformation of an orthotropic glass fiber reinforced composite with sub-millimeter yarn dimensions. Digital image correlation was utilized to capture and quantify the multi-scale full-field displacement and strain distributions within the samples of woven composites subjected to tensile loading at different fiber orientations. By carefully observing and analyzing the local deformation field and characterizing the local material response, the possible failure mechanisms for specimens of different fiber orientations were identified. To our knowledge, this is the first detailed experimental work which attempts to quantify the local strain heterogeneity in composites at submillimeter length scale and based on which offer possible explanation on the different macro-scale failure mechanisms observed in composites at different fiber orientation angles.

5.3. MATERIAL AND SPECIMEN GEOMETRY

The material examined in this work is a 1 mm thick five-layer orthogonally woven glass fiber fabric combined with halogenated epoxy resin, containing approximately 70 Vol% glass fibers. The glass fibers of ~7 µm diameter are processed into tows interwoven to an orthotropic plain weave fabric. The plain weave configuration of the fiber bundles make unit cells of 0.75×0.75 mm^2 dimensions in the material. The configuration of the woven bundles in the composite is shown in Figure 5.1. This material was manufactured in sheets of 1200×900 mm^2 dimensions by Norplex-Micarta®

under the commercial name NP130, with E_1=25.9 GPa, E_2=23.2 GPa, G_{12}=5.0 GPa and ν_{12}=0.15 [14].

Tensile specimens of two different sizes, small and large specimens, are machined from the sheet described above to study the deformation response of the material at different length scales. For the small-scale (meso-scale) experiments, rectangular coupon specimens of 40 mm×10 mm×1 mm were extracted from the as-fabricated composite sheets using a waterjet machine. Specimens with fiber orientation angles, $\beta = 0^o$, $\pm 45^o$ and 90^o, relative to the principal fiber orientations were extracted. A schematic view of the orientation of the rectangular tensile samples is illustrated in Figure 5.1.

For large scale (macro-scale) experiments, larger off-axis specimens of 170 mm×25 mm×1 mm dimensions were extracted from the original composite sheet at orientations identical to those of small-scale tensile specimens, i.e. $\beta = 0^o$, $\pm 45^o$ and 90^o.

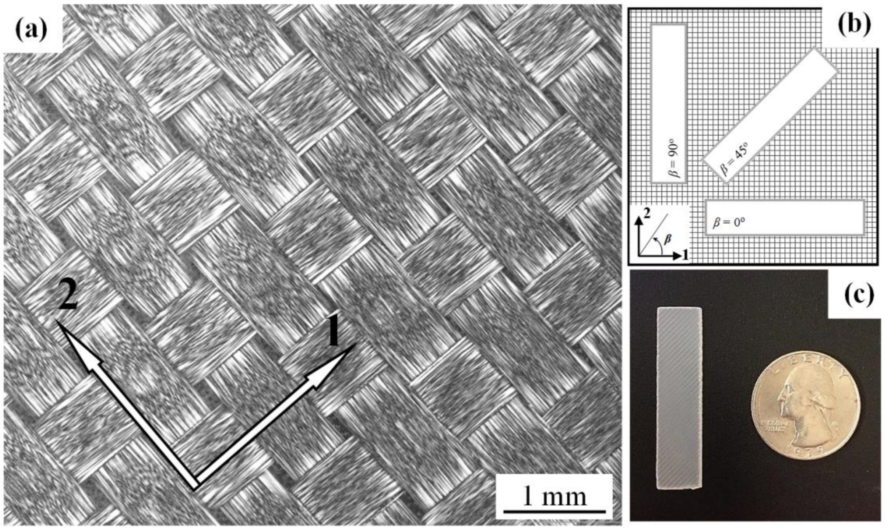

Figure 5.1 (a) The structure of the woven bundles of the composite used in this study, with the principal directions marked as 1 and 2. The image was taken using a scanning acoustic microscope. Orientation of the small-scale off-axis tensile specimens extracted from the original sheet is shown in (b) and the actual size of the tensile specimen is depicted in (c).

5.4. TENSILE EXPERIMENTS

The tensile properties of the specimens were evaluated at two scales. The global tensile behavior of the off-axis specimens was investigated by conducting tensile tests on large specimens. A 250 kN MTS machine was utilized for the evaluation of global flow response of the specimens. Tensile specimens were affixed into the machine using aluminum tabs placed on either side of the specimen thickness at both ends, to minimize the damage caused by hardened serrated steel grips of the machine. Loading was applied monotonically until complete failure at a rate of 0.254 mm.min^{-1}, corresponding to a nominal strain rate of 4×10^{-5} s^{-1}, using displacement control mode. A single 5 MP camera equipped with a 55 mm lens was used to capture images during the loading stage. Load and displacement data were acquired simultaneously with the camera system through a data acquisition system at a rate of 2 Hz. The images along with the load data were later used as the input for the DIC measurements.

In order to examine the local deformation response of the specimens, tensile experiments were also performed on the small-scale rectangular coupons using a miniature 2 kN tensile machine. Tensile experiments were conducted in room temperature under displacement control mode. Specimens were fastened into a small tensile frame using a pair of aluminum tabs attached to either end of the specimen, to prevent any possible damage caused by serrated steel grips of the tensile machine. The tensile frame with a mounted small tensile specimen is shown in Figure 5.2. A set of optical microscopy system equipped with a CCD camera was coupled with the tensile frame to facilitate the meso-scale DIC measurements. The optical microscope system mounted on top of the tensile frame is shown in Figure 5.2. During loading, the displacement control mode with crosshead speed of 0.1 mm.min^{-1} was utilized in all small-scale experiments, resulting in an average strain rate of 8×10^{-5} s^{-1}.

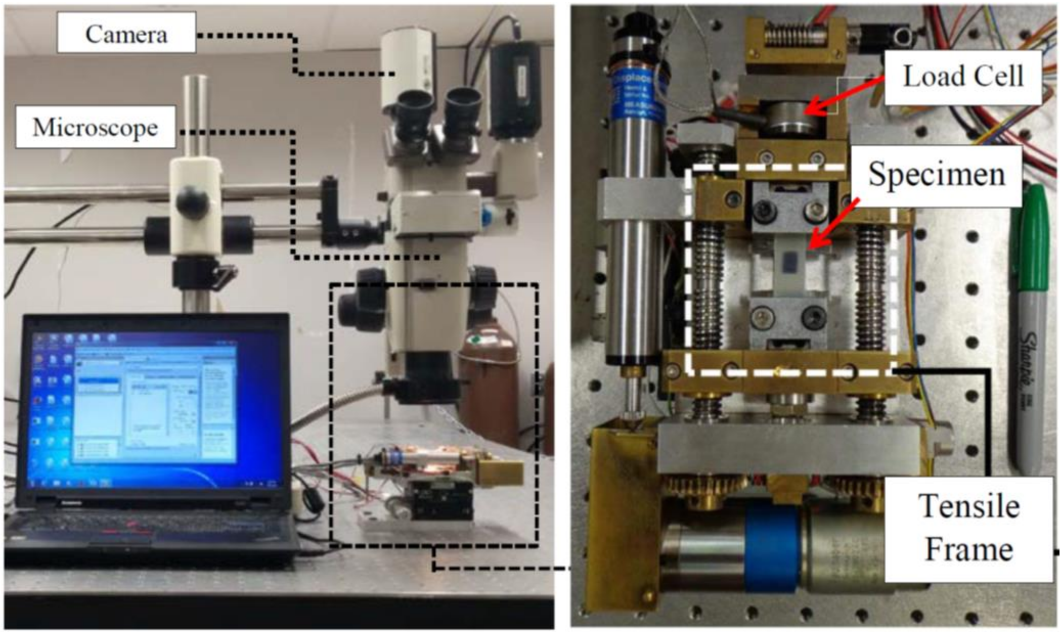

Figure 5.2 The optical microscope system with the camera mounted on top of the miniature tensile frame, used to study the meso-scale deformation response of the small-scale specimens is shown on the left. Details of the miniature tensile frame with specimen mounted on it are shown on the right.

To capture the local deformation response of the small tensile specimens during loading, images were taken continuously at a rate of 2 Hz from the surface of the specimen using the optical microscope adjusted perpendicular and at a ~20 mm vertical distance above the tensile specimen. The resolution of the images was 1360×1060 pixel^2 and the framing rate of the camera was synchronized with that of the load cell through a data acquisition system. Three tests were performed for each case corresponding to specimens with fiber orientation angle $\beta = 0^o$, $\pm 45^o$ and 90^o; and the macroscopic stress-strain relation was reported by averaging the set of results obtained for each case.

5.5. DIGITAL IMAGE CORRELATION

To facilitate the digital image correlation analysis, the specimen surface has to be speckled with a high contrast, random and homogenous size speckle pattern. For the case of macro-scale experiments, a thin layer of white paint was first manually applied on the surface of the large off-axis tensile specimens. Then, an air gun was used to spray a fine-particle black pattern on top of the white surface. With this technique a random, homogenized and high contrast speckle pattern with the average speckle size of 40 µm is achieved as shown in Figure 5.3. The field of view for this experiment was 220×170 mm^2.

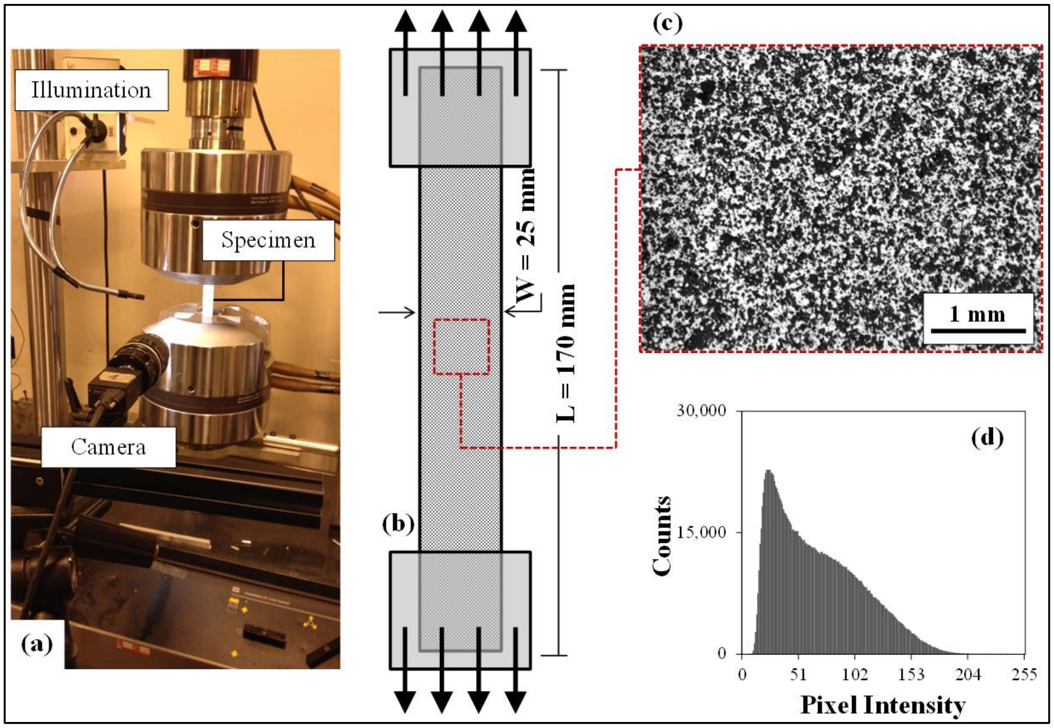

Figure 5.3 (a) The experimental setup used to study the global mechanical behavior of off-axis tensile specimens, with the schematic specimen geometry shown in (b). Typical speckle pattern applied on the specimen with its corresponding grey scale histogram are also shown in (c) and (d), respectively.

Images taken during the tensile loading were then used to extract the displacement and strain fields. The commercial image correlation software Vic-2D® was used to extract the displacement and strain fields. In this software, subset and step sizes of 63 pixel and 19 pixel dimensions were selected, respectively. Once the strain field is extracted, the average strain over the gage length area along with the load cell data was used to plot the stress-strain curve. In addition, the axial and transverse strain distributions within the area of interest were used to calculate the global elastic modulus and Poisson's ratio of specimens with different fiber orientation angles. Further details of the utilized analysis procedure can be found elsewhere [14, 15].

For the case of meso-scale deformation experiments, images were taken at magnifications higher than that used for the continuum scale experiment. Experiments were conducted at two different magnifications, 75× and 225×, which correspond to $3\times2.3\ mm^2$ and $1\times0.78\ mm^2$ fields of views, respectively. Further details and specifications of the high magnification experiments can be found in Table 5.1. Note that the highest magnification used in this work allowed us to study the local deformation within an area containing only a single unit cell. In order to perform DIC at such high magnifications, a far smaller speckle pattern must be achieved to accurately calculate the displacements and the strains. Fortuitously, at this magnification, a natural characteristic of the material was noticed to provide a nice high contrast speckle pattern. The pattern could have been resulted due to the presence of fairly small air bubbles trapped inside the epoxy matrix during the processing of the composite sheets. To take advantage of such unique material characteristic as the speckling method, a small area on the back side of each tensile specimen was painted with a glossy black paint (see Figure 5.4a) to permit the partial reflection of the light emitted through the front side of the specimen. In this manner, by observing the front surface of the specimen through a high magnification lens with a coaxial localized illumination system, an evenly-distributed fine pattern is obtained. Preparation of the specimens using this method will yield in a high contrast advantageous speckle pattern useful for meso-scale digital image correlation measurements. The speckle patterns developed using this method are shown in Figure 5.4b and 5.4c for two different magnifications.

Table 5.1 High magnification full-field measurement details

Magnification	Field of view dimensions (mm^2)	Pixel-to-length ratio (µm/pixel)
75 X	3.0 × 2.3	2.205
225 X	1.0 × 0.78	0.735

Similar to the continuum scale studies, the meso-scale local deformation response of the specimens with different fiber orientation angles was also studied using DIC. The high magnification images taken during the tensile loading were used as the input and the displacement and strain fields were extracted using Vic-2D®. For the case of 75× magnification, a subset size of 21 pixels with step size of 5 pixels was utilized, while in the case of 225× magnification, subset and step sizes of 63 pixels and 5 pixels were utilized, respectively.

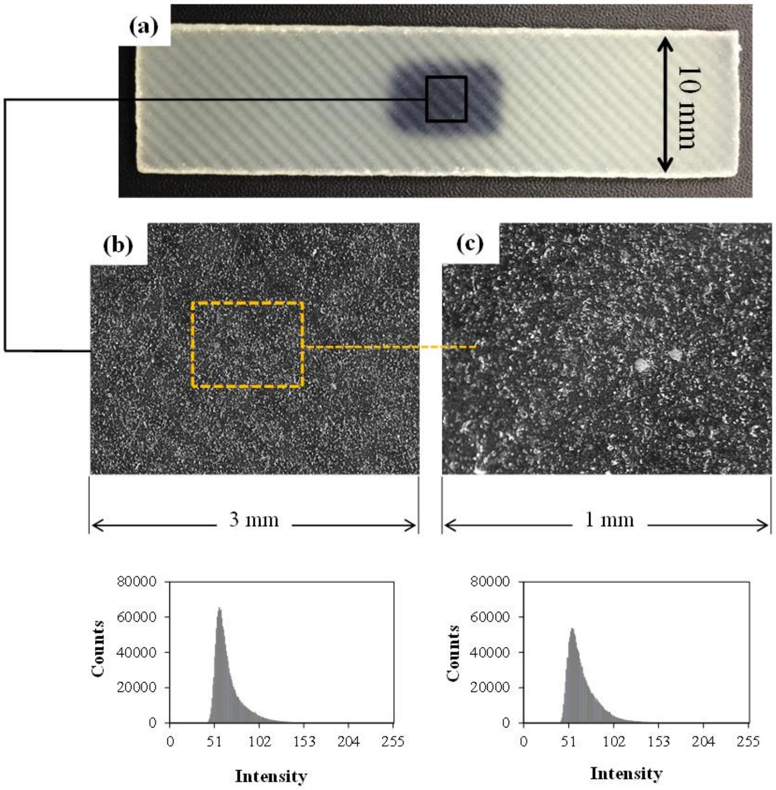

Figure 5.4 (a) Tensile specimen used for meso-scale observations with the speckled areas of interest shown in (b) and (c) for high magnification observations.

5.6. GLOBAL TENSILE RESPONSE AND FAILURE MECHANISMS

Global stress-strain curves for specimens with different fiber orientation angles were obtained by averaging the axial strain field over the entire gage area of the large specimen along with the load measured form the load cell. Note that the full-field evolution of the vertical strain component, ε_{yy}, within the gage length area containing several hundred data points, is obtained as a direct output of a DIC analysis. It has been documented that, in the case of orthotropic composites, spatial averaging of the full-field strain data from DIC can give more accurate results when compared with conventional extensometer (see e.g. [14, 16]). Considering this, the average uniaxial strains were used in this work to determine stress-strain response of the specimens with different fiber orientation angles. The global stress-strain curves were also obtained using the same procedure by averaging the axial strain components over the gage length of the small-scale specimens at 75× magnification. The stress-strain curves obtained from three independent experiments on the β=±45° specimen are plotted in Figure 5.5a, indicating the repeatability of the obtained results. The global stress-strain curves for specimens with different fiber orientation angles obtained following the same procedure are plotted in Figure 5.5b. It can be seen that the two sets of results, i.e. the stress-strain curves obtained from small and large tensile specimens, show a very good agreement, except that the 2 kN load cell in the miniature tensile frame limits the extents of the stress applied on the specimens to about 160 MPa. These results indicate two important aspects:

1) The influence of the specimen dimensions (size effect) is minimal at this length scale, and the flow behavior of the material obtained from the small-scale tensile experiments is sufficiently accurate to represent the material's deformation response in tension.

2) The size of the field of view at 75× magnification is 3×2.3 mm^2. Considering the size of a single unit cell of the material (≈0.8×0.8 mm^2), it is believed that at least 10 unit cells would be present within the field of view at this magnification. Thus, the strain averaging at 75× magnification has been carried out on at least 10 unit cells. The agreement of the effective stress-strain response obtained by averaging the strain fields at 75× with the global stress-strain response of the large (standard size) specimen indicated that the field of view at 75× is sufficiently large to be statically representative of the global response of the examined composite material. Kanit et.al [17] define the representative volume element (RVE) as "RVE size can be associated with a given

precision of the estimation of the wanted overall property and the number of realizations of a given volume V of microstructure that one is able to consider". Following this definition and considering Figure 5.5b of the current work, it can be stated that the size of the field-of-view at 75× is sufficiently larger than the RVE size of the composite specimens used in the present work.

From the global stress-strain curves shown in Figure 5.5b, a remarkable change in the deformation response of specimens with different fiber orientation angles is evident. A significant drop in the value of elastic modulus with an increased strain-to-failure is observed when the fiber orientation angle changes from $0^o/90^o$ to $\pm45^o$, relative to the tensile axis. To provide a quantitative assessment, the global elastic moduli and Poisson's ratios of the off-axis tensile specimens were also calculated according to the procedure detailed in Refs. [14, 15]. A summary of the mechanical properties determined for samples with different fiber orientation angles is shown in Table 5.2. In ideal cases, for orthotropic materials such as the one considered in this study, a biaxial symmetry response is expected, i.e. the mechanical response of the specimens with $\beta=0^o$ and $\beta=90^o$ is expected to be identical. However, in practice the number of reinforcing fibers in the principal fiber angles are usually different, leading to relatively different mechanical and fracture properties when testing specimens extracted from the two principal fiber orientations, i.e. $\beta=0^o$ and $\beta=90^o$ [14, 18].

As clearly indicated in Table 5.2, the material properties exhibit a strong sensitivity to the orientation of the reinforcing fibers. Such anisotropic mechanical response can be explained through the load bearing mechanisms present in the specimens of different fiber orientation angles. For the case of $\beta=0^o$ and $\beta=90^o$ specimens, the load is mostly taken by the reinforcing fibers, which possess greater stiffness and lower ductility. The loading continues and is carried predominantly by the fibers until the failure strain of the fibers. Upon the failure of the fibers, the load would immediately transfer to the matrix. However, at this time, the magnitude of the load would be far beyond the strength of the matrix material, thus, leading to a complete failure of the composite instantaneously without showing any plastic flow.

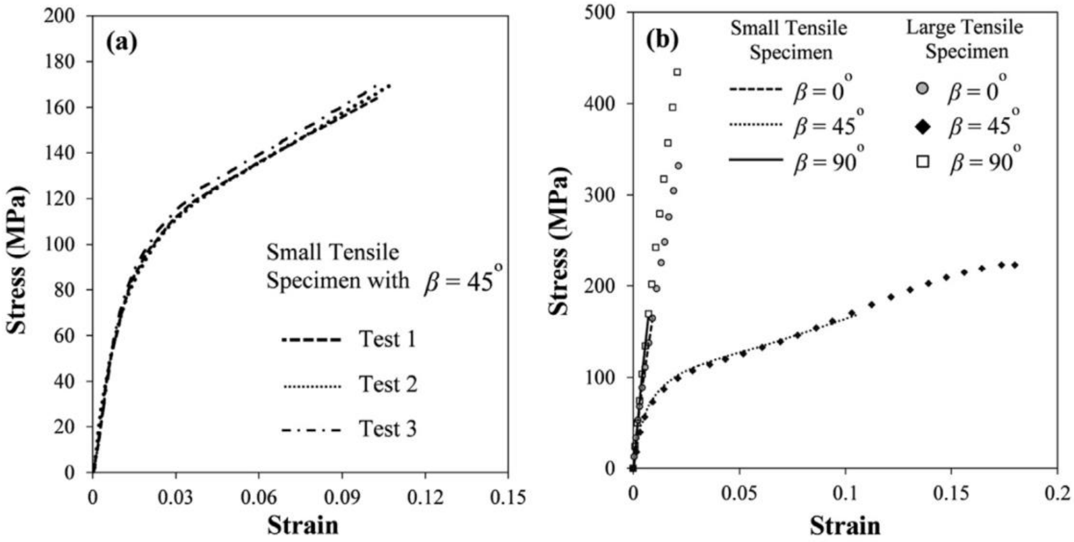

Figure 5.5 (a) Global stress-strain curves plotted for three independent tensile tests on the small scale β=45o specimen, confirming the repeatability of the conducted experiments. (b) Global stress-strain curves of the specimens with different fiber orientation angles, comparing the results obtained for small and large scale tensile specimens.

Table 5.2 Global elastic modulus, *E*, Poisson’s ratio, *v*, and failure strain, ε_f, determined for samples with different fiber orientation angles

β **(°)**	***E*** **(GPa)**	***v***	**ε_f (%)**
0	24.52	0.190	2.2
45	14.36	0.541	18.1
90	26.75	0.196	2.1

The front view of the fractured large specimens is illustrated in Figure 5.6. A rather straight fracture edge with dominated fiber pull-out mechanism is evident for specimens of $\beta=0^o/90^o$ (Figure 5.6b and 5.6c). The degree of fiber pull-out for $\beta=90^o$ specimen, mainly at regions closer to the specimen edge, seems to be higher than that observed for $\beta=0^o$. Such qualitatively higher level of fiber pull-out is in agreement with the stronger mechanical response measured earlier for $\beta=90^o$ specimen. Transverse fiber pull-out is also indicated to some extent, particularly within the regions closer to the middle section (x=W/2) of $\beta=0^o/90^o$ specimens. The explanations provided earlier can be strengthened when the top view of the fracture surfaces are examined. The deep pockets formed on the fracture surface of $\beta=0^o$ specimen, as shown in Figure 5.7b, indicate the fiber pull-out mechanism.

For the case of $\beta=45^o$, on the other hand, failure has occurred at multiple $\pm45^o$ angle orientations (Figure 5.6d). The conical structure formed at the fracture surface of this specimen indicates that the tensile load imposed to the specimen could have resulted in large shear deformations to be developed at the fiber/matrix interface. Such shear deformation can dominate void nucleation and coalescence within the fiber/matrix interface, consequently leading to multiple angled fracture planes, as shown in Figure 5.6d [7].

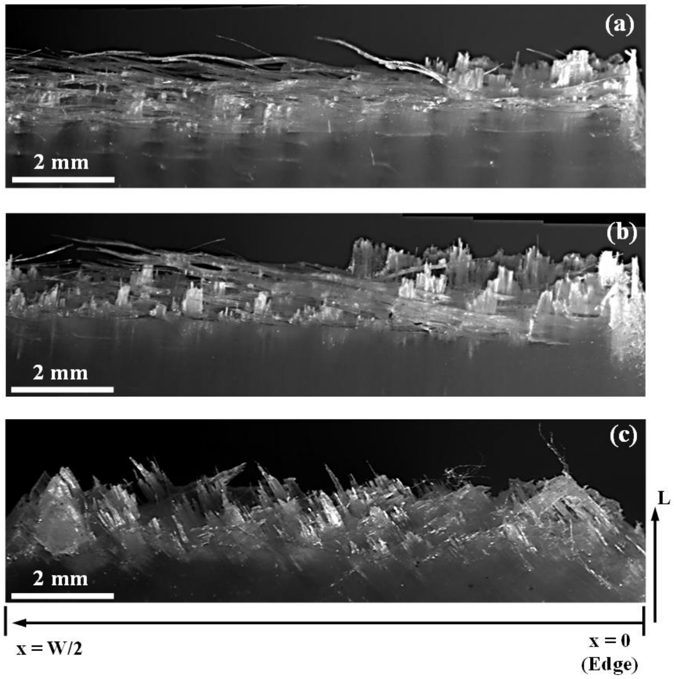

Figure 5.6 Front surface view of the fractured specimens with (a) β=0°, (b) β=90° and (c) β=45°.

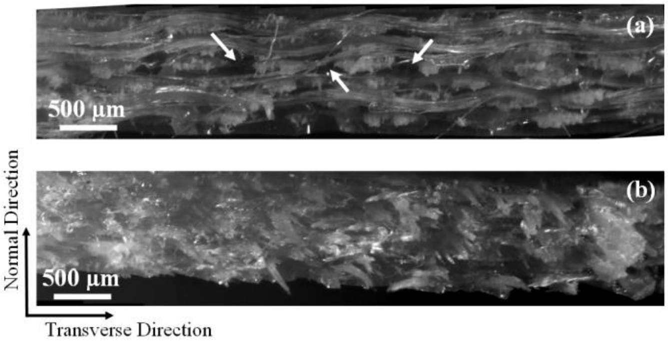

Figure 5.7 Fracture surface view of the specimens with (a) β=0° and (b) β=45°. The deep pockets indicating the fiber pull-out have been marked with arrows on (a).

During loading, the fiber bundles oriented at ±45° angles in β=45° specimen cause the applied tensile load to be shared between the compliant matrix and the stiffer fiber bundles. In this case, the matrix would initially take much of the tensile load. As the loading progresses, the fibers would partially stretch and rotate towards the loading direction. This tendency of the fibers to re-orient towards the loading direction in a woven composite is referred to as ‘fiber trellising’, and attributes to the significantly larger plastic deformation observed in the case of off-axis specimens [19]. During fiber trellising, the fibers are rotated towards the loading direction, rather than being stretched in tension. Therefore, the far-field load would be shared between the fibers and the matrix, whereas the deformation would basically occur within the matrix only, under a shear-type deformation. The shear-type deformation in this case is followed by nucleation of micro cracks within the epoxy-rich regions. Another possible mechanism argued by Godara and Raabe [7] states that “when the fibers are oriented at $\pm 45^o$ with respect to the tensile axis, the applied load is resolved and induces shear flow in the matrix even at the lower applied tensile load. When the local shear stress exceeds the shear strength of the polymer matrix, it starts flowing plastically and dominates the material behavior.” The occurrence of this mechanism usually spans over a wide range of global strain and eventually ends with the formation of a rough conical fracture surface, as shown in Figure 5.7c.

5.7. MESO-SCALE DEFORMATION IN ON-AXIS SPECIMENS

Meso-scale deformation response of the specimens extracted parallel to the principal fiber orientations, i.e. $\beta=0^o$ and $\beta=90^o$, was investigated using the full-field strain maps obtained from DIC measurements performed on small-scale tensile specimens. The evolution of accumulated vertical strain, εyy, in a local 3×2.3 mm^2 area has been typically depicted for a specimen of $\beta=0^o$ in Figure 5.8. A very similar pattern of strain inhomogeneity was observed for $\beta=90^o$ specimen, as well. The heterogeneous deformation response of the material at meso scale is clearly observed when the full-field small-scale strain distribution maps are compared with their relative global strain values. The local strain maps show highly uneven values comparing to the global tensile strain components in all cases. The level of difference, compared with the global strain, increases remarkably at higher global strains as shown in Figure 5.9. The locally accumulated vertical strains are indicated by a periodic pattern, showing minima and maxima at certain locations, corresponding to high strain domains (HS) and low strain domains (LS) in the material. Also, comparing Figures 5.9a and 5.9b, a higher level of discrepancy between the locally measured and global strain values are observed for the β=90° specimen, which might also be attributed to the different number of fibers used in the processing of the composite sheets. In this case (Figure 5.9b), the periodic variation of the local vertical strain exhibits a more pronounced fluctuation relative to the global strain values, when compared to the specimen with β=0°, i.e. Figure 5.9a.

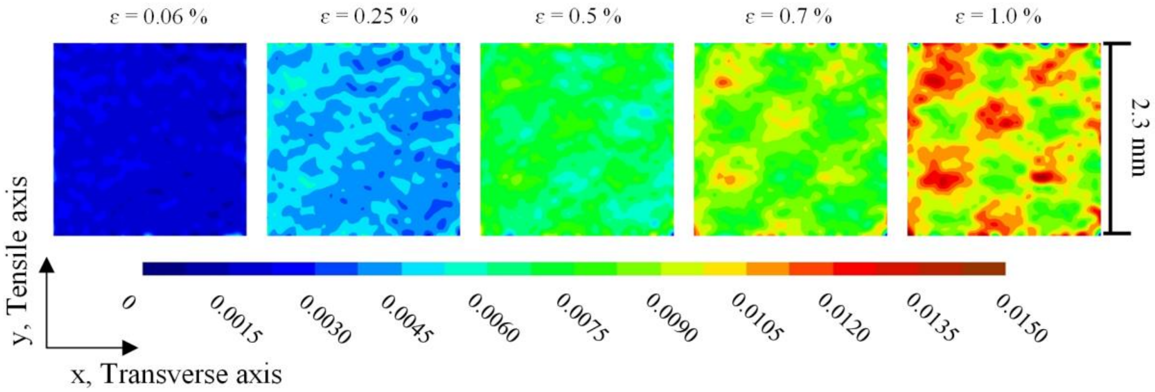

Figure 5.8 Evolution of the local high and low strain domains at different global strain magnitudes, for specimen with β=0°. The global strain magnitudes corresponding to each strain contour can be found on above the contours.

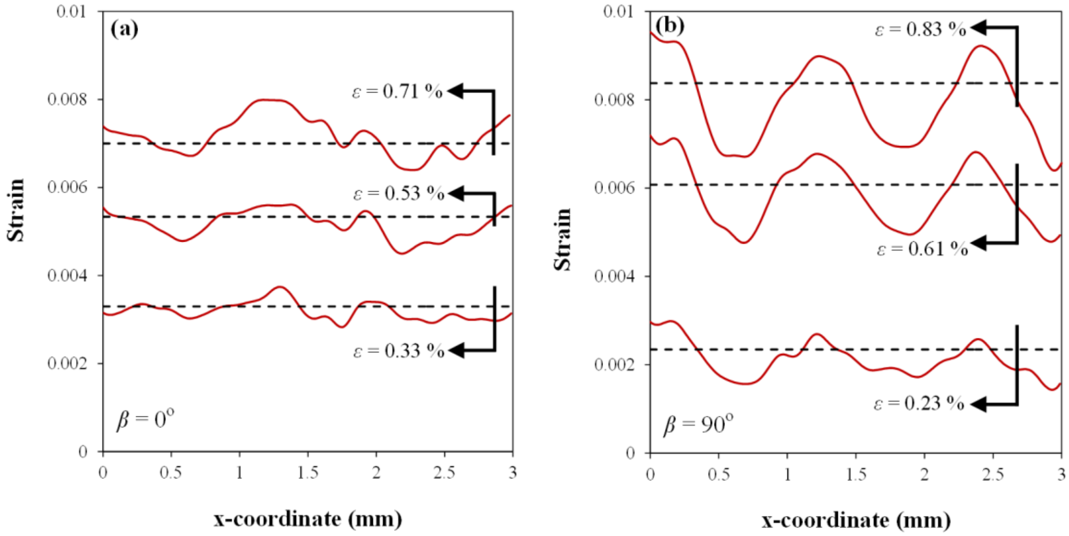

Figure 5.9 A comparison between the magnitudes of local and global vertical strains developed in specimens with (a) β=0° and (b) β=90°.

The nature of deformation inhomogeneity in specimens of β=0° and β=90° at meso scale can be explained through the load bearing mechanisms present in these samples, as described earlier. The reinforcing fibers for both β=0° and β=90° cases are oriented parallel to the tensile axis. The fibers aligned parallel to the tensile axis are in a state of iso-strain, while the transverse fibers are in iso-stress conditions [7]. The softer polymer matrix present in between the transverse fiber bundles, on the other hand, would be unable to bear the equivalent imposed tensile load which was transferred to the fibers oriented along the tensile axis. Therefore, due to the difference of the deformation response between the compliant matrix and the stiffer transversely oriented fibers, a highly localized vertical strain would be developed within the epoxy-rich regions located in between the transverse fiber bundles, as shown in Figure 5.10. This figure demonstrates a sub-millimeter epoxy-rich region confined by transverse and longitudinal fiber bundles, which has undergone a larger magnitude of vertical strain. The local vertical strain developed within this region shows a ~50% higher value than the far-field strain applied on the specimen. The highly localized accumulation of vertical strain in these regions, as described earlier, can be considered as failure initiation sites in the specimens loaded parallel to their principal axes, i.e. β=0º/90º. Figure 5.11 also shows a comparison between the local strain values on high and low strain domains for specimens of β=0º and β=90º. Comparing the LS and HS domains for these specimens, a local difference of ~50% for β=0º and ~30% for β=90º was measured, at a global vertical strain of about 0.75%. As explained earlier, due to its locally weaker mechanical strength in the epoxy-rich regions, the material will eventually fail mainly by longitudinal fiber pull-out mechanism, as well as transverse fiber pull-out to some extent. This was earlier demonstrated and confirmed in fracture surface studies of the specimens of β=0º and β=90º in Figures 5.6b and 5.6c.

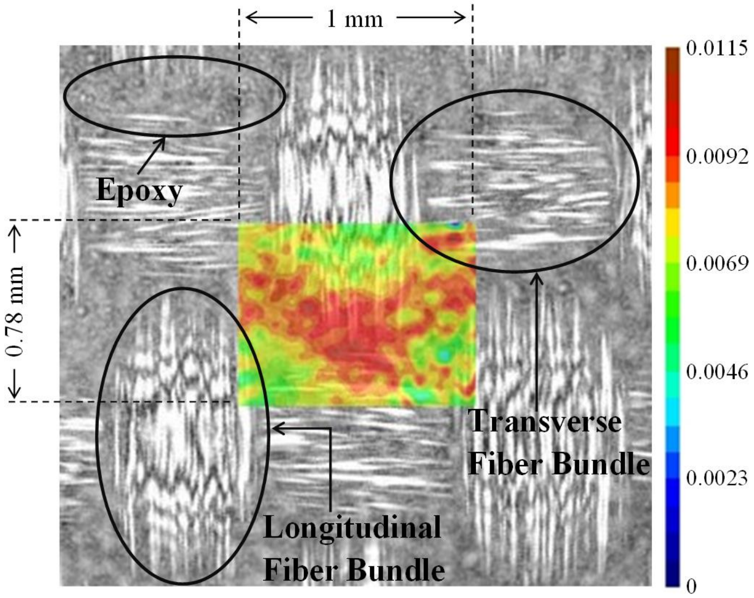

Figure 5.10 The local vertical strain (ε_{yy}) contour map, showing highly localized strain magnitude within the regions located in between the transverse fiber bundles for a β=90º specimen (The global vertical strain = 0.75%). Note that the location of the area of interest was marked before the meso-scale observations, and the contour map was overlaid on the microstructural image afterwards.

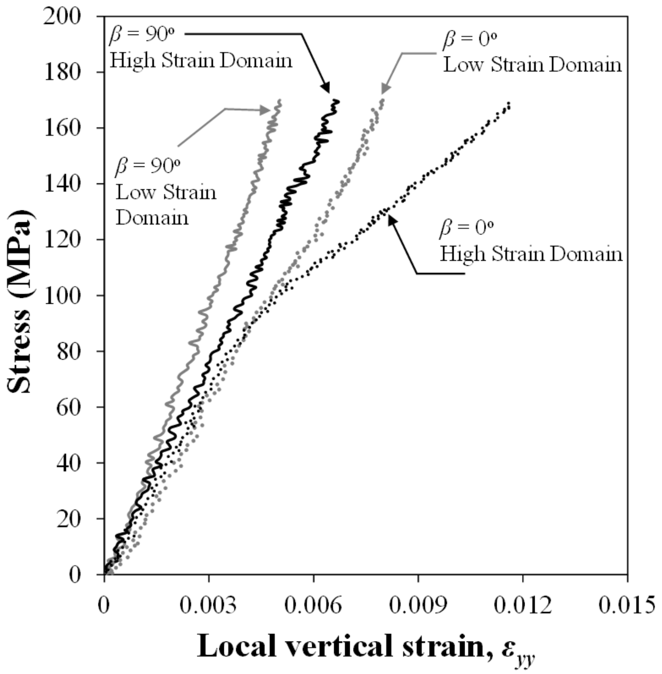

Figure 5.11 Evolution of local vertical strain component at low and high strain domains for specimens of β=0° and β=90°.

5.8. MESO-SCALE DEFORMATION IN β=45° SPECIMEN

Meso-scale deformation response of off-axis specimen with β=45° was also examined similar to β=0°/90° specimens at different magnifications. A highly nonhomogeneous deformation is evolved during the tensile straining of the specimen. Similar to what observed for specimens of β=0°/90°, the level of deformation inhomogeneity increases with increasing the magnitude of the global strain applied on the specimen, as shown in Figure 5.12. Local strain values seem to have a greater level of homogeneity at lower global stain magnitudes. However, with further increase of the applied tensile load, particularly well after the yield strength is reached, the deformation heterogeneity becomes more pronounced. This is followed by formation of distinct high and low strain domains within the area of interest, as illustrated in Figure 5.13 and Figure 5.14.

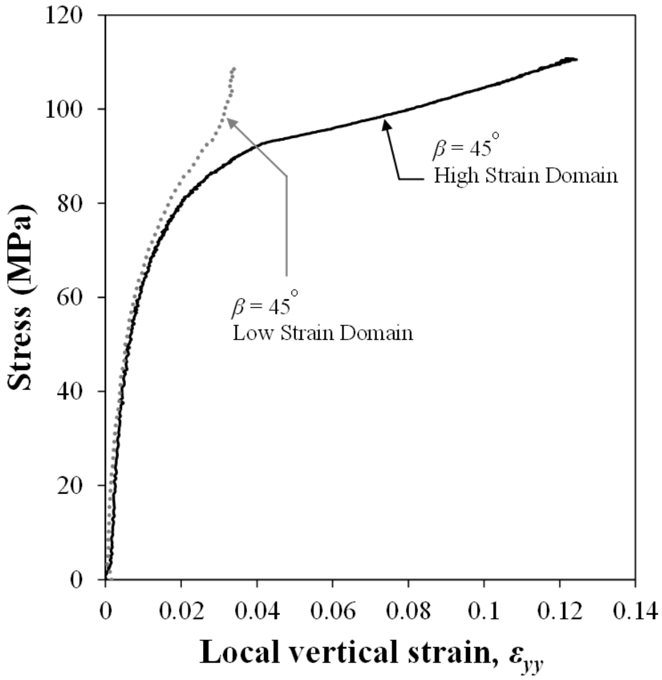

Figure 5.12 Evolution of local vertical strain component at low and high strain domains for specimens of β=45°.

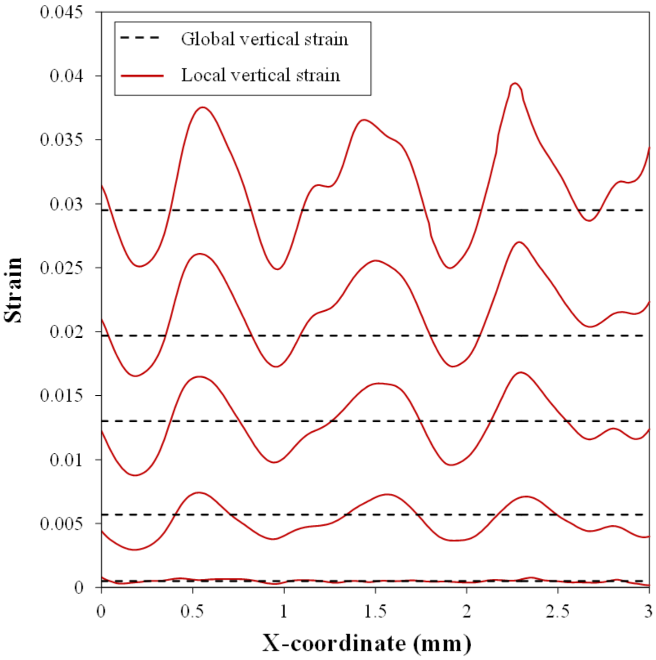

Figure 5.13 A comparison between the magnitudes of local and global vertical strains developed in the specimen β=45°. A higher level of inhomogeneity is observed as the global strain magnitude is increased.

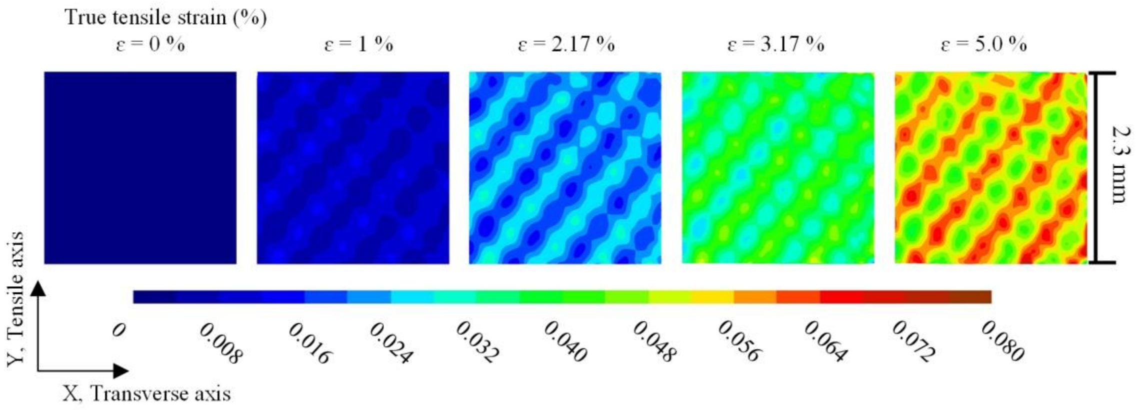

Figure 5.14 Evolution of the local high and low strain domains at different global strain magnitudes, for specimen with β=45°. The global strain magnitudes corresponding to each strain contour can be found on its above.

Typical vertical strain contours for β=45° specimen at higher magnification are illustrated in Figure 5.15, comparing the developed strain fields in macro and meso scales. It is interesting to note that at 8% global strain, the local strain on the LS areas (locations at which reinforcing fibers are dominantly present) is almost 0, while the strain in the matrix zone reaches to above 10%. This explains why the β=45° specimens exhibit a remarkably larger failure strain compared with the β=0°/90° specimens. As described in earlier sections, for the case of β=45° specimen, the load bearing mechanism would be completely different from that of β=0°/90° specimens. In this case, the applied tensile stress is expected to be shared between the epoxy and the trellising fiber bundles oriented at ±45° angles with respect to the principal axes. However, owing to the different flow responses of the constituent phases in the composite, i.e. epoxy and glass fibers, as well as the described fiber trellising phenomenon, a shear strain would be developed in the interfacial regions between fiber bundles and the matrix. The presence of such high shear strain values is demonstrated in Figure 5.16, where the contour maps of local vertical strain (ε_{yy}) and local shear strain (ε_{xy}) components for β=45° specimen are plotted. Note that the local maximum shear strain value developed in HS domains is about 15% of the local vertical strain component and about 20% of the global tensile strain. Such high magnitudes of the shear stain, which is mostly carried by the softer epoxy phase, can result in the formation of micro voids in these areas. Further tensile deformation of the specimen yields in the coalescence of such voids, and eventually the specimen failure. The failure of the specimen in this case would take place exhibiting a highly roughened conical fracture surface, as earlier demonstrated in Figures 5.6d and 5.7c.

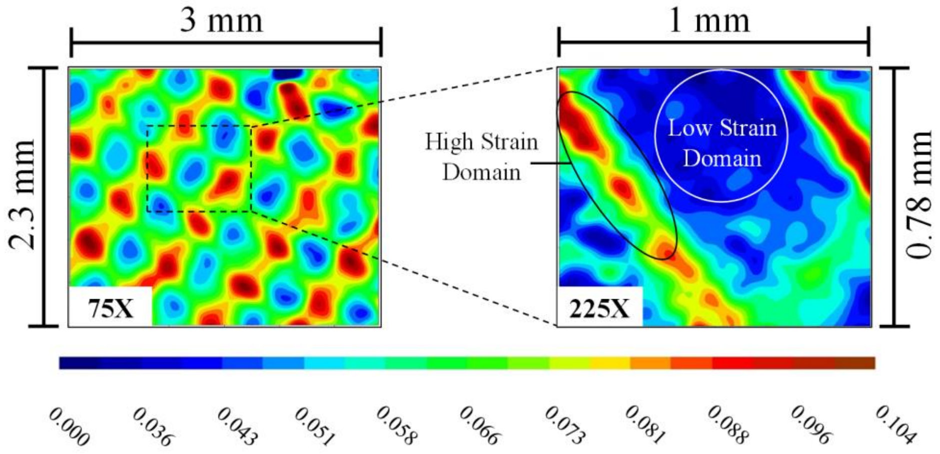

Figure 5.15 Meso-scale vertical strain contour maps taken at different magnifications for specimen with β=45^o, at a global strain magnitude of 8%.

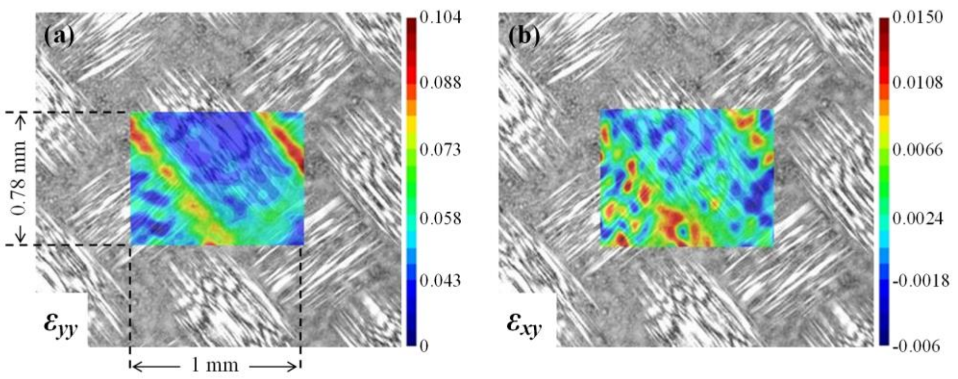

Figure 5.16 The local (a) vertical strain, ε_{yy}, and (b) shear strain, ε_{xy}, contour maps for a β=45^o specimen (The global vertical strain = 8%).

5.9. CONCLUSIONS

Multiscale experiments based on digital image correlation were conducted to study the in-plane deformation response of glass-fiber reinforced woven composites subjected to tensile loading. The main failure mechanisms for composites specimen loaded at different fiber orientation angle were also investigated. The global stress-strain responses, as well as the bulk failure modes were found to be highly sensitive to the angle between the loading axis and the principal fiber orientations. The failure strain of 45^o off-axis specimens was shown to be at least 8 times higher than that obtained for the specimens extracted parallel to the principal axes. A remarkable difference in the fracture surface of the specimens with different fiber orientation angles was also observed, exhibiting a rather flat surface with significant fiber pull-out failure mechanism for the case of specimen with fibers oriented at 0^o and 90^o angle relative to the tensile loading direction. The failure and deformation mechanism of these specimens were further investigated through meso-scale deformation studies. It was revealed that a high magnitude of localized normal strain is developed within the regions between soft polymer matrix and the transverse fiber bundles, which eventually causes fiber pull-out and the formation of a rather flat fracture surface. On the other hand, the conical rough fracture surface of the off axis 45^o specimen investigated through meso-scale DIC revealed that domains of high shear strain are formed within the polymer-rich regions confined by the fiber bundles, which eventually give rise to a shear type failure associated with a rough conical shear surface. To our knowledge, this is the first time that the local heterogeneity and its effect on the failure mechanism in woven fiber-reinforced composites with different fiber orientations have been experimentally investigated at submillimeter and macro scales, concurrently. We believe that the results of such studies can give a better insight in understanding of the deformation response of composites, in general.

5.10 LIST OF REFERENCES

[1] Lomov SV, Ivanov DS, Verpoest I, Zako M, Kurashiki T, Nakai H, Hirosawa S. Meso-FE modeling of textile composites: Road map, data flow and algorithms. Composite Science and Technology 2007; 67: 1870-1891.

[2] Tabatabaei SA, Lomov SV, Verpoest I. Assessment of embedded element technique in meso-FE modeling of fibre reinforced composites. Composite Structures 2014; 107: 436-446.

[3] Zhang C, Binienda WK. A meso-scale finite element model for simulating free-edge effect in carbon/epoxy textile composite. Mechanics of Materials 2014; 76: 1-19.

[4] Naouar N, Vidal-Salle E, Schneider J, Maire E, Boisse P. Meso-scale FE analyses of textile composite reinforcement deformation based on X-ray computed tomography. Composite Structures 2014; 116: 165-176.

[5] Sutton MA, Orteu JJ, Schreier HW. Image correlation for shape, motion and deformation measurements – Basic concepts, theory and applications. Springer, NY, 2009.

[6] Godara A, Raabe D, Bergmann I, Putz R, Muller U. Influence of additives on the global mechanical behavior and the microscopic strain localization in wood reinforced polypropylene composites during tensile deformation investigated using digital image correlation. Composite Science and Technology 2008; 69: 139-146.

[7] Godara A, Raabe D. Influence of fiber orientation on global mechanical behavior and mesoscale strain localization in a short glass-fiber-reinforced epoxy polymer composite during tensile deformation investigated using digital image correlation. Composite Science and Technology 2007; 67: 2417-2427.

[8] Lomov SV, Ivanov DS, Verpoest I, Zako M, Kurashiki T, Nakai H, Molimard J, Vautrin A. Full-field strain measurements for validation of meso-FE analysis of textile composites. Composites Part A-Applied Science 2008; 39: 1218-1231.

[9] Lomov SV, Boisse Ph, Deluycker E, Morestin F, Vanclooster K, Vandepitte D, Verpoest I, Willems A. Full-field strain measurements in textile deformability studies. Composites Part A-Applied Science 2008; 39: 1232-1244.

[10] Nicoletto G, Anzelotti G, Riva E. Mesoscopic strain fields in woven composites: Experiments vs. finite element modeling. Optics and Lasers in Engineering 2009; 47: 352-359.

[11] Daggumati S, Voet E, Van Paepegem W, Degrieck J, Xu J, Lomov SV, Verpoest I. Local strain in a 5-harness satin weave composite under static tension: Part 1 – Experimental analysis. Composite Science and Technology 2011; 71: 1171-1179.

[12] Fard MY, Sadat SM, Raji BB, Chattopadhyay A. Damage characterization of surface and sub-surface defects in stitch-bonded biaxial carbon/epoxy composites. Composites Part B-Engineering 2014; 56: 821-829.

[13] Ullah H, Harland AR, Silberchmidt VV. Characterization of mechanical behavior and damage analysis of 2D woven composites under bending. Composites Part B-Engineering 2015; 75: 156-166.

[14] Pollock P, Yu L, Sutton MA, Guo S, Majumdar P, Gresil M. Full-field measurements for determining orthotropic elastic parameters of woven glass-epoxy composites using off-axis tensile specimens. Experimental Techniques 2012; 38: 61-71.

[15] Koohbor B, Mallon S, Kidane A, Sutton MA. A DIC-based study of in-plane mechanical response and fracture of orthotropic carbon fiber reinforced composite. Composites Part B-Engineering 2014; 66: 388-399.

[16] Kraft SM, Moslehy EA, Bai Y, Gordon AP. Characterization of the orthotropic elastic constants of a micronic woven wire mesh via digital image correlation. Experimental Mechanics 2014; 54: 501-514.

[17] Kanit T, Forest S, Galliet I, Mounoury V, Jeulin D. Determination of the size of the representative volume element for random composites: statistical and numerical approach. International Journal of Solids and Structures 2003; 40: 3647-3679.

[18] Mallon S, Koohbor B, Kidane A, Sutton MA. Fracture behavior of prestressed composites subjected to shock loading: a DIC-based study. Experimental Mechanics 2015; 55: 211-225.

[19] Xue P, Cao J, Chen J. Integrated micro/macro-mechanical model of woven fabric composites under large deformation. Composite Structures 2005; 70: 69-80.

CHAPTER 6

MESO-SCALE EXPERIMENTAL ANALYSIS OF NON-LINEAR TENSILE RESPONSE AND FIBER TRELLISING MECHANISMS IN WOVEN COMPOSITES [5]

---

[5] Koohbor B, Ravindran S, Kidane A. *Journal of Reinforced Plastics and Composites* 2016; 35(12): 986-995. doi: 10.1177/0731684416633771
Reused here with permission of publisher.

6.1 ABSTRACT

Non-linear deformation response of plain woven carbon fiber reinforced composites is experimentally studied at meso-scales. Stereovision digital image correlation is utilized to capture the full-field strain distribution over an area containing approximately five unit cells. The evolutions of local strains on the fiber bundles and matrix rich regions as a function of loading are extracted. The effect of fiber orientation angle on fiber bundles stretch ratio and their angle of rotation (fiber trellising) and the related underlying failure mechanisms are analyzed using the measured full-field displacement data. The results indicate that the local load bearing mechanisms are different in on-axis and off-axis loading conditions; while, the larger global failure strain noticed in off-axis conditions is attributed to the occurrence of fiber rotation. The fiber trellising is also shown to promote high local shear strain and consequently leads to the protrusion of the matrix material on the deformed specimen surface.

6.2 INTRODUCTION

It is well-established that fiber composites exhibit non-linear stress-strain response under off-axis loading. This non-linearity is often observed in the global tensile stress-strain curves of off-axis specimens and is the consequence of complex load bearing mechanisms resulted from interactions between the reinforcing fibers and the matrix [1]. It is also understood that the global mechanical response of off-axis fiber composites has a strong sensitivity to the angle between the loading direction and the orientation of the fibers. The fiber orientation angle affects the degree of the non-linearity in the constitutive response of the composite [2-4].

Although detailed studies of micro- and macroscopic behavior of fiber composites are currently available in the literature, there are only few studies dealing with the meso-scale response of fiber composites, particularly from the experimental perspective [5-12]. These experimental-base investigations have generally been carried out in a more qualitative sense to understand the yarn interaction mechanisms [9, 10], the nature of deformation inhomogeneity in fiber composites [5, 12], detection of damage initiation [11], to provide correlation between the macro-scale deformation and failure response to the meso-scale behavior of the material [7], and to validate FE simulation [6]. Lomov et al. [5], for instance, conducted strain measurements at meso-scales on various fabrics to study their deformability under shear and tensile loading conditions. In their work, 2D digital image correlation (DIC) was used to successfully capture the local deformation response and to assess the deformation homogeneity in a variety of fabrics. Meso-scale full-field strain maps measured by Ivanon et al. [6] were used for plasticity detection, damage initiation modeling and validation of meso-FE models. The meso-scale deformation analysis of short fiber reinforced epoxy composite conducted by Godara and Raabe [7] attempted to identify high and low strain domains within the axially-loaded off-axis composite specimens. Meso-scale strain localization and local deformation response of woven glass fiber reinforced composites was studied in a recent work by the authors [8]. Strain mapping was successfully practiced in sub-millimeter scales using optical microscopy in conjunction with 2D digital image correlation. This work also was performed in a more qualitative sense to identify the load bearing mechanisms existing in different off-axis specimens. It is interesting to note that the application of digital image correlation is the common method in all research works mentioned above. This is due to the capability of the technique to capture accurate full-field deformation response of materials, as well as the availability of plug-and-play commercial systems [13]. This powerful optical technique has been successfully practiced in the deformation and failure analyses of fiber composites at a wide range of time and length scales [14, 15].The angle-dependence of the macroscale constitutive response of woven composites has long been understood in the composite research community. A more detailed survey in the available literature on woven fiber composites reveals that the local deformation mechanisms, as well as the origin of the non-linear deformation response are not yet well understood. The underlying mechanisms behind this orientation dependence are believed to be due to the occurrence of fiber trellising mechanism in the off-axis specimens subjected to in-plane tension [8]. Fiber trellising has so far only been investigated either at macro scales or through the use of complex finite element analyses . However, fiber trellising is a local mechanism and no evidence on the meso-scale experimental study of this phenomenon is found in the literature. In light of this, the present work attempts to experimentally study the meso-scale deformation response of a plain woven carbon fiber reinforced composite and to provide quantitative information on the nature of deformation non-linearity in tensile behavior of off-axis composite specimens.

In this regard, stereo-vision digital image correlation (3D DIC) was utilized to capture full-field strain maps at submillimeter length scales. Theoretically, for flat samples loaded in-plane, the use of a single camera system and 2D DIC is sufficient. However, the accuracy of 2D DIC is highly affected by the out-of-plane deformation.

The use of 3D DIC has been established to allow for a substantially more accurate evaluation of the full-field displacement and strain distributions, particularly when significant out-of-plane displacement is present within the field of interest [16]. The presence of such out-of-plane motions was confirmed in this study as a direct result of fiber trellising, which causes the protrusion of soft matrix material on the surface of the specimen. In addition, the principal mechanisms behind the non-linear response of off-axis woven composite specimens, i.e. fiber trellising and individual fiber bundle stretch were successfully studied by providing quantitative analyses based on experimental measurements. This, to our knowledge, has never been conducted in the existing literature on the subject. The authors strongly believe that the current research is the first of its kind to deal with a detailed study of underlying mechanisms in the fiber trellising phenomenon from an experimental perspective.

6.3 MATERIAL AND SPECIMEN GEOMETRY

Quasi-static tensile experiments were conducted on three layer orthogonally woven carbon fiber reinforced composite sheets of 0.8 mm thickness. The composite contains approximately 70 Vol% carbon fibers. Carbon fibers of ~7 µm in diameter are processed into tows interwoven to a plain weave fabric, forming unit cells of ~1.8×1.8 mm^2 dimensions. Further details on the properties of the composite specimens used in the present work can be found elsewhere [3]. Rectangular specimens of 25 mm wide and 175 mm long were cut out of the as-received composite sheet in directions of $\beta = 0^o$, 15^o, 30^o and 45^o, measured from the vertical principal direction, as shown in Figure 6.1a. The grip length was 25 mm at both specimen ends, resulting in a gage length of 125 mm.

Specimens were inserted into the tensile machine with their grip length held inside the hydraulic grips. To protect against the damage caused by serrated steel grips, 2 mm thick aluminum tabs were epoxied on the grip section at both ends of the tensile specimens, as shown in Figure 6.1b.

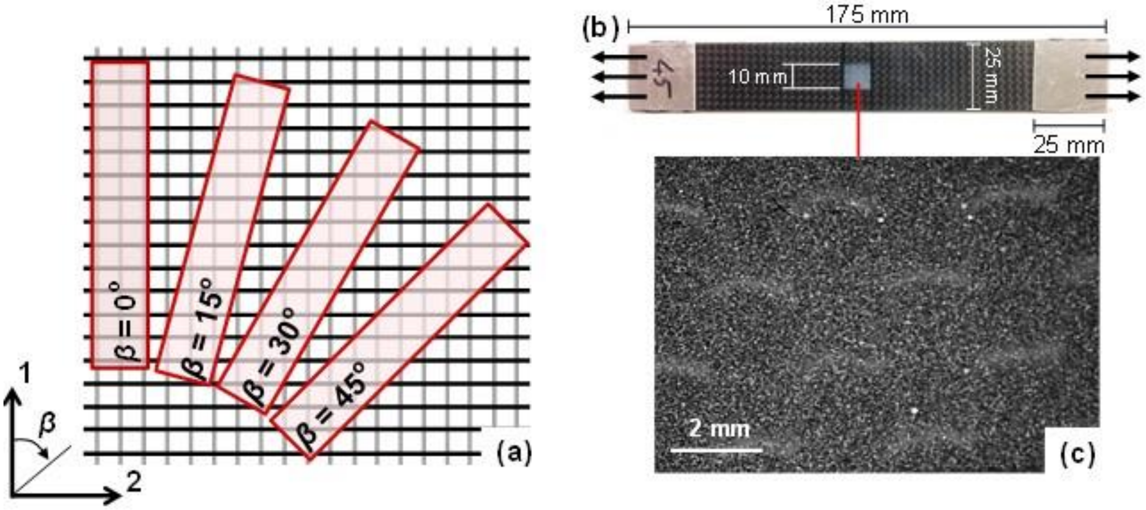

Figure 6.1 (a) Schematic view of the off-axis tensile specimens. An actual tensile specimen is illustrated in (b) and the typical speckle pattern applied on the specimen center can be seen in (c).

6.4 TENSILE EXPERIMENTS AND DIGITAL IMAGE CORRELATION

Tensile tests were performed using a 250 kN MTS machine in displacement control mode at a rate of 1.5 mm min^{-1}, which is equivalent to a mean strain rate of 2×10^{-4} s^{-1}. Load and cross-head displacement data were acquired from the load-cell and displacement sensors of the tensile frame, respectively, while their sampling rates were synchronized with the framing rate of the cameras used for the image correlation purpose.

3D digital image correlation was used to study the full-field deformation response of specimens at meso scales. A high-contrast, random and isotropic speckle pattern is required to extract full-field deformation response using DIC. Taking advantage of the natural black color of the specimens, a white speckle pattern containing ~20 µm equally spaced dots was applied on a 10×10 mm^2 area at the center of each specimen using an air brush and a diluted flat white paint (see Figure 6.1b and 6.1c).

A stereovision camera system containing a pair of 5 MP CCD cameras, each equipped with a high magnification 100 mm Macro lens was used to capture stereo images of the speckled area during loading. In the case of stereovision digital image correlation (3D DIC), the out-of-plane motion will not have any significant contribution to the in-plane deformation measurement and hence, the accuracy of the in-plane strain measurements will be substantially improved [16]. The camera system was calibrated prior to the tensile experiments using 6×6 mm^2 calibration plates [17]. External illumination containing high intensity LED white light source was used to promote uniform illumination of the specimen in the region of interest. Figure 6.2 depicts the experimental setup used in this work. Calibration details of the stereovision system are listed in Table 6.1.

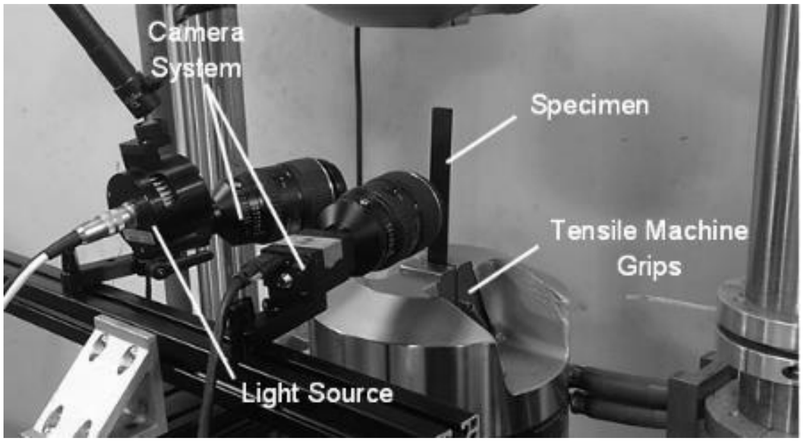

Figure 6.2 The experimental setup utilized to capture meso-scale deformation response of the specimens in this work.

Table 6.1 System parameters obtained from calibration of the stereo camera arrangements

Parameter	**Camera 1**	**Camera 2**
Center - x (pixels)	1003	682
Center - y (pixels)	1299	597
Focal length - x (pixels)	52005	55023
Focal length - y (pixels)	52014	55043
Skew (°)	0.94	-3.39
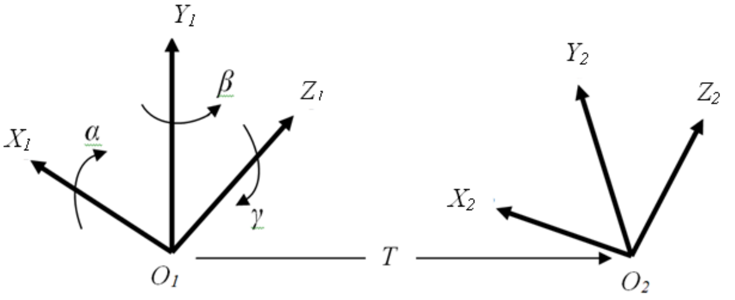		
Alpha (°)	-0.34	
Beta (°)	-28.07	
Gamma (°)	0.00	
Tx (mm)	103.77	
Ty (mm)	0.42	
Tz (mm)	38.75	

Images from the speckled region were taken during tensile loading, at full-field resolution of 2448×2048 pixel^2 and at a rate of 1 fps. Images acquired during the tensile experiments were used to extract the displacement and strain fields using commercial DIC software Vic-3D [17]. In this software, subset and step sizes of 81 pixel and 9 pixel were selected, respectively, and a spatial resolution of 7.21 μm/pix was determined.

6.5 MATHEMATICAL ANALYSIS OF FIBER TRELLISING

When woven composites are subjected to off-axis tensile loading, the fiber bundles tend to re-orient towards the direction of the applied load. This behavior is referred to as ‘fiber trellising’ and is documented to occur when the angle between the fiber bundles changes from 90° [8, 18, 19]. The highest degree of fiber trellising in woven composites is observed in 45° off-axis specimen and accounts for the large non-linear deformation response observed in the material. In this work, fiber trellising phenomenon was studied and quantitatively analyzed at meso-scales, by tracking the local deformation and rotation of fiber bundles, as discussed below.

Let us consider a single fiber bundle with initial length l_i and initial angle θ_i, relative to the horizontal axis as shown in Figure 6.3. Upon exertion of the tensile load, the section is stretched to a length l_f and rotated towards the loading direction. The angle between the principal bundle axis and horizontal axis is increased to θ_f at this point. Variables l_i and l_f can be quantified by tracking the displacement fields at positions A and B, as:

$$l_i = \sqrt{(x_B - x_A)^2 + (y_B - y_A)^2} \tag{6.1a}$$

$$l_f = \sqrt{(x_{B'} - x_{A'})^2 + (y_{B'} - y_{A'})^2} = \sqrt{[(x_B - x_A) + (u_B - u_A)]^2 + [(y_B - y_A) + (v_B - v_A)]^2} \tag{6.1b}$$

where x_k and y_k represent the original coordinates at point k, respectively; and u_k and v_k are the horizontal and vertical displacement components at the same point, respectively. Similarly, the angle θ, in undeformed (θ_i) and deformed (θ_f) states can be calculated as:

$$\theta_i = \tan^{-1}\left[\frac{y_B - y_A}{x_B - x_A}\right] \tag{6.2a}$$

$$\theta_f = \tan^{-1}\left[\frac{y_{B'} - y_{A'}}{x_{B'} - x_{A'}}\right] = \tan^{-1}\left[\frac{(y_B - y_A) + (v_B - v_A)}{(x_B - x_A) + (u_B - u_A)}\right] \tag{6.2b}$$

All variables shown in Eq. (6.1) and (6.2) can be obtained from the results of meso-scale DIC analyses. Obtaining the local fiber stretch magnitude and its angle change facilitates a quantitative analysis of fiber trellising occurred in different off-axis specimens.

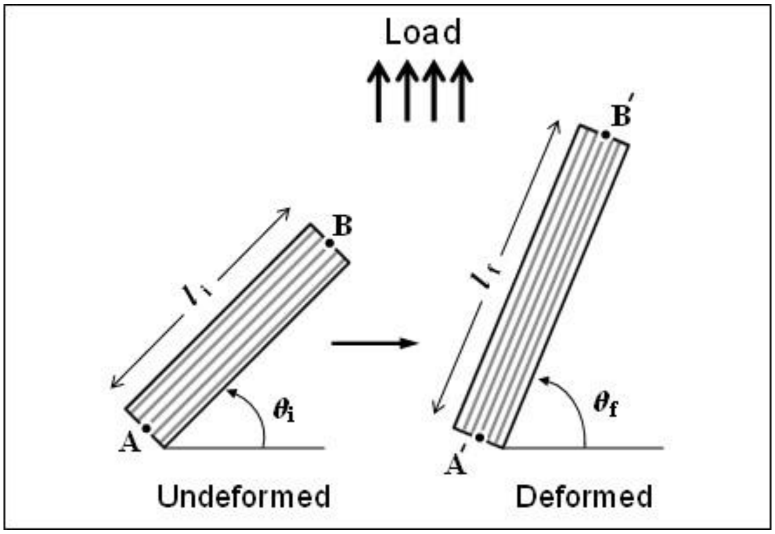

Figure 6.3 Schematic configurations of a single longitudinal tow, before and after application of the tensile load.

6.6 GLOBAL STRESS-STRAIN CURVES

Global stress-strain curves of the off-axis specimens were obtained using two methods. First, following the conventional procedure, load and displacement in the gauge area were measured from the machine load-cell and cross-head motion, respectively, and the global flow curves were plotted. In the second approach, the load measured by the machine load-cell was used to determine the global stress value. However, the strain developed in the specimen was obtained by spatial averaging of the full-field vertical strain maps captured by DIC [2, 3]. Figure 6.4 shows the global true stress-strain curves obtained using the two approaches. Close agreement between the two sets of curves indicates that the field of view (10×10 mm^2) used in the DIC analysis has been large enough to be statistically representative of the global response of the material [8, 20].

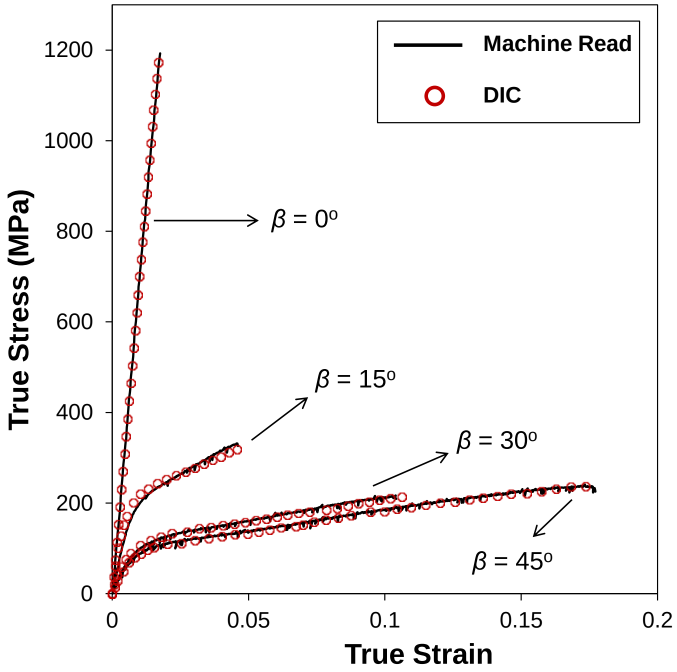

Figure 6.4 Global stress-strain curves obtained for the off-axis specimens.

Global mechanical properties of the off-axis specimens were extracted from the global flow curves and are listed in Table 6.2. In addition, a comparison has been made between the global mechanical parameters determined in this work with those documented in the literature. Table 6.2 also shows this comparison, indicating a good agreement between the results obtained in this work with those available in the literature. The off-axis specimens exhibit significantly different mechanical response in terms of elastic modulus, Poisson's ratio and strain-to-failure. The failure strain (ε_f) at global scale was found to be one order of magnitude larger for the case of $\beta = 45^o$ compared with $\beta = 0^o$. Such substantial variation observed in the global mechanical response of composite specimens can be further investigated considering the differences in the underlying load bearing mechanisms in each specimen.

Table 6.2 Global mechanical properties of the off-axis specimens

β (º)	Obtained in this work			Documented in [3]		
	E (GPa)	υ	ε_f (%)	E (GPa)	υ	ε_f (%)
0	68.1	0.076	1.75	59.75	0.076	1.90
15	35.9	0.487	4.61	30.06	0.469	4.80
30	16.7	0.739	10.42	16.11	0.740	15.45
45	11.9	0.779	17.72	11.73	0.794	17.90

6.7 MESO-SCALE DEFORMATION RESPONSE

Typical contours showing the evolution of full-field vertical strain on a 5×5 mm^2 area at the center of 45^o off-axis specimen are plotted in Figure 6.5. The contour maps show highly non-homogeneous strain fields, with noticeably large vertical strain component localized in multiple parallel inclined strips. Note that the maximum local strain values shown here are considerably higher than the corresponding global strain in each image. Such local non-homogeneous deformation response has also been observed in the case of other off-axis specimens, however with different degrees of non-homogeneity.

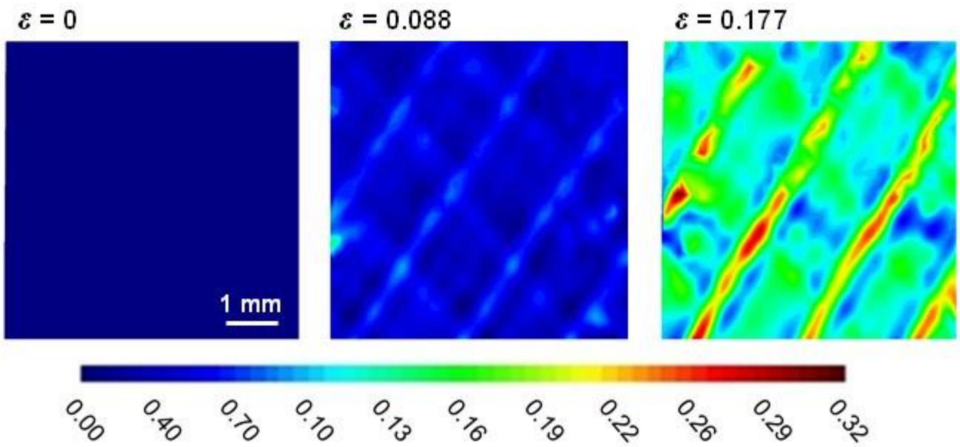

Figure 6.5 Evolution of vertical strain component at different global strain magnitudes for 45^o off -axis specimen. The global strain magnitude corresponding to each plot is indicated on the top. Far-field load is applied vertically.

Figure 6.6 demonstrates the local non-homogeneity of the vertical strain at the instant of failure, for different off-axis specimens. Considering the locations of maximum and minimum local vertical strains, it is observed that for β = 0° the largest magnitude of local strain is developed within the areas containing mostly fiber bundles oriented parallel to the direction of the tensile load (see Figure 6.6a). This indicates that the longitudinal tows undergo the tensile deformation in β = 0°, and accordingly, it can be expected that the tensile load is mostly carried by these tows. On the other hand, for other off-axis specimens, i.e. β = 15°, 30° and 45°, the largest local strain is developed in epoxy-rich areas confined between longitudinal and transverse tows, as seen in Figure 6.6b and 6.6c. Note that the degree of strain localization significantly increases in β = 45° specimen compared with β = 15°. In addition, the fiber-rich areas for these specimens show substantially lower strain magnitudes.

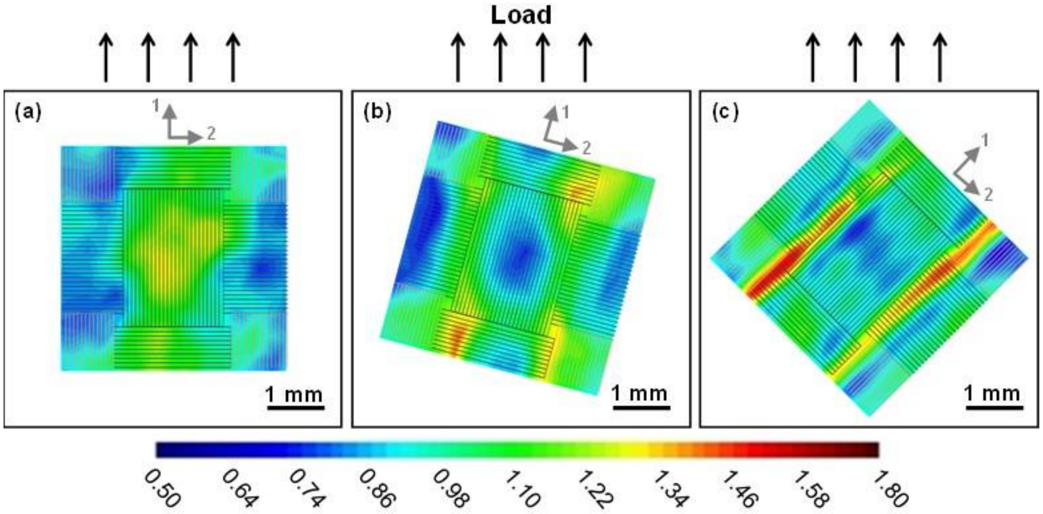

Figure 6.6 Full-field distribution of normalized vertical strain component ($\varepsilon_{yy}/\varepsilon_f$) for (a) β = 0° (b) β = 15° and (c) β = 45°. Directions of the far-field load and principal fibers are marked.

Comparison between two extreme cases, i.e. β = 0° and β = 45° has also been made by plotting the variation of normalized local vertical strain across three unit cells, as shown in Figure 6.7. Note that the curves in Figure 6.7 represent the variation of normalized vertical strain (ε_{yy}) at the instant of failure for each specimen, where ε_f denotes the failure strain of the corresponding sample. Figure 6.7 also confirms the expected significantly larger variation of strain across the cells in the case of 45° off-axis specimen compared with β = 0°. To explain such differences, it should be noted that in off-axis specimens, i.e. β = 15°, 30° and 45°, the application of an axial tensile load could result in the rotation of the fiber bundles towards the loading direction, in addition to the stretching of the fiber bundles. This tendency of the fibers to re-orient towards the loading axis, or the so-called 'fiber trellising' phenomenon, attributes to the large local plastic deformation observed in off-axis specimens.

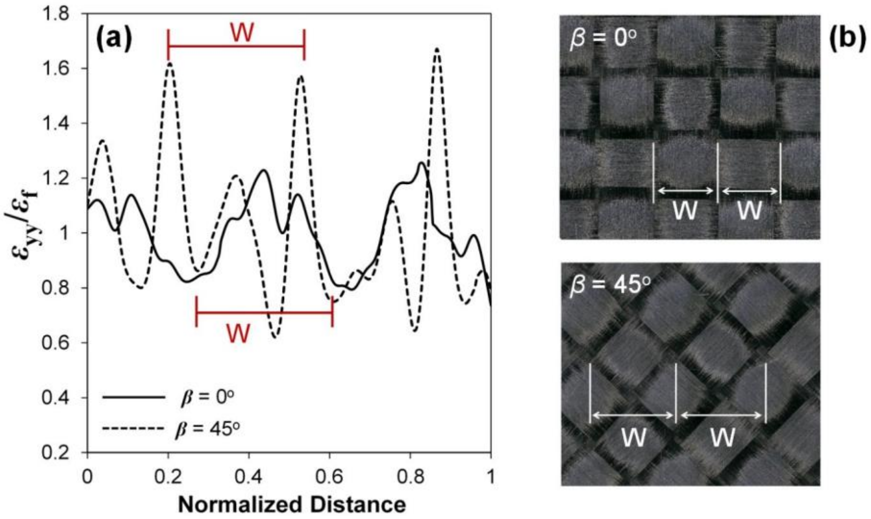

Figure 6.7 (a) Variation of normalized vertical strain component ($\varepsilon_{yy}/\varepsilon_f$) across three unit cells of width 'W', shown schematically in (b), for the specimens with β = 0° and β = 45°. Note that far-field load is applied vertically.

The magnitude of fiber stretch was measured for each specimen, according to Eq. (6.1). Figure 6.8 shows the variation of fiber stretch ratio, $\Delta l/l_i$, as a function of global vertical strain applied on each specimen. Considering the curves in Figure 6.8, the following two remarks need to be discussed:

1) It is clearly observed that the value of the fiber stretch ratio in $\beta = 0^o$ at any given point during deformation is close to the global strain value applied on the specimen. This observation is in agreement with the discussion provided earlier on the more significant role of longitudinal fiber tows in load bearing mechanism of this specimen. This behavior significantly changes with increasing the angle between the fiber bundles and the loading direction.

2) Although the global failure strain magnitudes of the specimens in the present work were found to be remarkably different, the magnitudes of their corresponding fiber stretch ratios upon failure were relatively close, being in the range of 1.07% to 1.28%. This agrees well with the fact that when failure occurs, the fiber stretch cannot be larger than the failure strain of the fiber, regardless of its tensile loading angle. On the other hand, the larger values of global failure strains measured for specimens with $0^o < \beta \leq 45^o$ might be attributed to fiber trellising [19].

The fiber rotation angles calculated based on Eq. (6.2) are depicted in Figure 6.9 for different specimens. It is clearly observed that the angle of fiber rotation calculated for the off-axis specimens are substantially larger compared with the on-axis specimen. It is also evident that the $\beta = 45^o$ specimen exhibits the largest value of rotation, $\Delta\theta \approx 9^o$, at the instant of failure. Such high degree of in-plane rotation can impose a large shear strain on the epoxy-rich regions of the material confined within the longitudinal and transverse fiber bundles. The development of this large shear strain has been exemplified in Figure 6.10, where the full-field shear strain distributions for two extreme cases, i.e. β = 0° and β = 45°, are displayed.

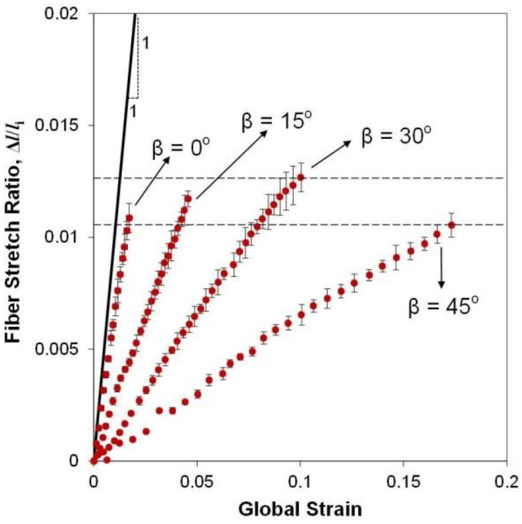

Figure 6.8 Variation of fiber stretch ratio ($\Delta l/l_i$) with respect to the global vertical strain for different off-axis specimens examined in this work. Each curve represents the average of three independent measurements.

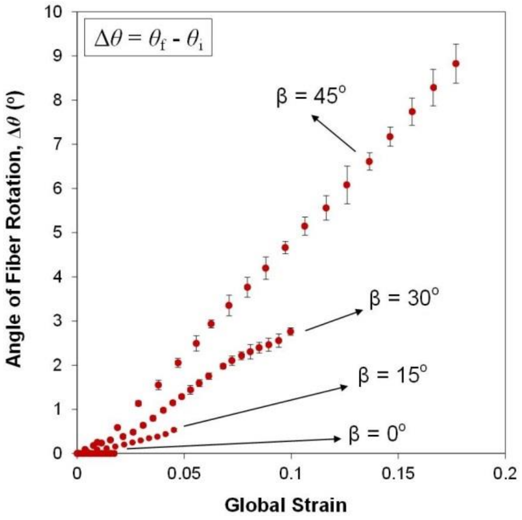

Figure 6.9 Variation of fiber rotation angle ($\Delta\theta$) with respect to the global vertical strain for off-axis specimens examined in this work.

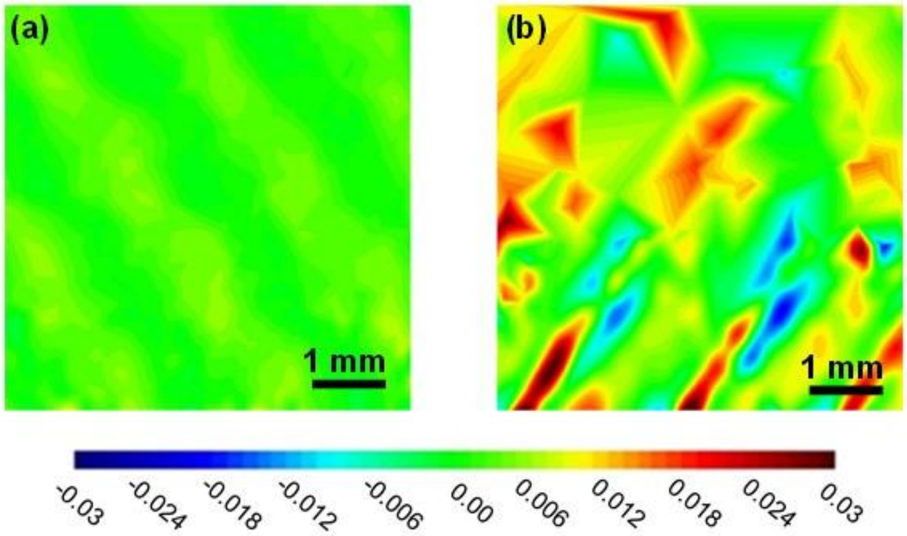

Figure 6.10 Full-field distribution of shear strain component (ε_{xy}) for (a) β = 0° and (b) β = 45°, at the instant of failure.

Further post-mortem investigations revealed that the occurrence of large in-plane rotations in off-axis specimens can increase surface asperity of the deformed material. Figure 6.11 depicts the high magnification images taken from the surface of the specimens after failure. The degree of the so-called surface asperity is significantly higher for β = 45° and is decreased progressively as β converges to 0°. Also, the 3D profile measurements conducted on the specimen surface indicate that the peak value of the surface asperity for β = 45° is located over the intersection of longitudinal and transverse fiber tows.

The observation of the developed local surface asperities in β = 45° can again be explained through the fiber trellising mechanism. As discussed earlier, the large rotation of the fibers can exert substantially large values of shear deformation on the epoxy regions confined within the orthogonal fiber tows. This large deformation magnitude may eventually cause the relatively softer epoxy to be extruded out of the plane of the lamina. This mechanism results in the formation of surface asperities on the epoxy rich regions on the surface ply, as illustrated earlier in Figure 6.11. However, the occurrence of such local out-of-plane deformation of the epoxy within the inner plies of the composite sheet may give rise to the partial delamination of the plies, yielding in the nucleation of internal damage. The explained mechanism can be considered as a possible internal damage mechanism for woven composite subjected to off-axis tensile loading conditions and can be a point of interest for future investigations on the subject.

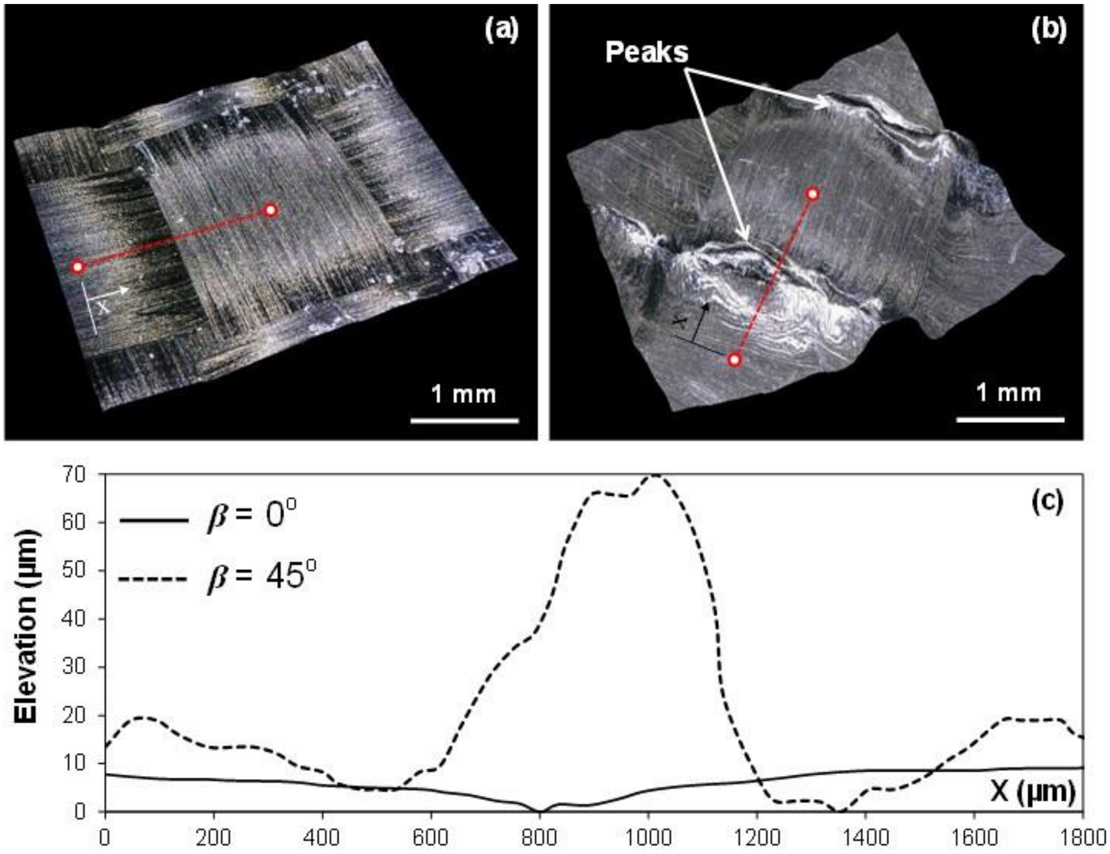

Figure 6.11 High magnification images showing the surface profile of (a) β = 0° and (b) β = 45° off-axis specimens after failure. The magnitudes of the surface elevation along the transverse direction (dashed line marked on (a) and (b)) are plotted in (c).

6.8 CONCLUSIONS

Off-axis tensile deformation response of an orthogonally woven carbon fiber reinforced composite was studied at mesoscopic scales. Stereovision digital image correlation was used to capture full-field displacement and strain distributions over a millimeter-sized area at the center of the specimens. The significantly different global mechanical responses of the off-axis specimens in this work were explained through the load bearing mechanisms as a function of fiber orientation, while the experimental data were used to validate the proposed mechanisms. Non-linear response observed in specimens with $0^{o} < \beta \leq 45^{o}$ relative to the loading direction, were explained as a result of the concurrent deformation of fibers and matrix when the specimen is subjected to far-field tensile loading. The experimental results also indicated that such non-linear response is mainly due to the occurrence of the in-plane rotation of longitudinal and transverse fiber tows, imposing large shear strains onto the softer epoxy-rich regions within the material. The large shear deformations were found to develop remarkable out-of-plane deformation of the matrix material, resulting in epoxy protrusion and consequently increasing the surface roughness of the deformed specimens.

6.9 LIST OF REFERENCES

[1] Ogihara S, Reifsnider KL. Characterization of nonlinear behavior in woven composite laminates. Applied Composite Materials 2002; 9: 249-263.

[2] Pollock P, Yu L, Sutton MA, Guo S, Majumdar P, Gresil M. Full-field measurements for determining orthotropic elastic parameters of woven glass-epoxy composites using off-axis tensile specimens. Experimental Techniques 2014; 38: 61-71.

[3] Koohbor B, Mallon S, Kidane A, Sutton MA. A DIC-based study of in-plane mechanical response and fracture of orthotropic carbon fiber reinforced composite. Composites Part B-Engineering 2014; 66: 388-399.

[4] Xing L, Reifsnider KL, Huang X. Progressive damage modeling for large deformation loading of composite structures. Composite Science and Technology 2009; 69: 780-784.

[5] Lomov SV, Boisse P, Deluycker E, Morestin F, Vanclooster K, Vandepitte D, Verpoest I, Willems A. Full-field strain measurements in textile deformability studies. Composites Part A-Applied Science 2008; 39: 1232-1244.

[6] Ivanov D, Ivanov S, Lomov S, Verpoest I. Strain mapping analysis of textile composites. Optics and Lasers in Engineering 2009; 47: 360-370.

[7] Godara A, Raabe D. Influence of fiber orientation on global mechanical behavior and mesoscale strain localization in a short glass fiber-reinforced epoxy polymer composite during tensile deformation investigated using digital image correlation. Composite Science and Technology 2007; 67: 2417-2427.

[8] Koohbor B, Ravindran S, Kidane A. Meso-scale strain localization and failure response of an orthotropic woven glass-fiber reinforced composite. Composites Part B-Engineering 2015; 78: 308-318.

[9] Lomov SV, Ivanov DS, Verpoest I, Zako M, Kurashiki T, Nakai H, Molimard J, and Vautrin A. Full-field strain measurements for validation of meso-FE analysis of textile composites. Composites Part A–Applied Science 2008; 39: 1218-1231.

[10] Daggumati S, Voet E, Van Paepegem W, Degrieck J, Xu J, Lomov SV, Verpoest I. Local strain in a 5-harness satin weave composite under static tension: Part 1 – Experimental analysis. Composite Science and Technology 2011; 71: 1171-1179.

[11] Ullah H, Harland AR, Silberscmidt VV. Characterisation of mechanical behaviour and damage analysis of 2D woven composites under bending. Composites Part B–Engineering 2015; 75: 156-166.

[12] Nicoletto G, Anzelotti G, Riva E. Mesoscopic strain field in woven composites: Experimental vs. finite element modeling. Optics and Lasers in Engineering 2009; 47: 352-359.

[13] Sutton MA, Orteu JJ, Schreier HW. Image correlation for shape, motion and deformation measurements. New York: Springer, 2009.

[14] Canal LP, Gonzalez C, Molina-Aldareguia JM, Segurado J, Llorca J. Application of digital image correlation at micro-scale in fiber-reinforced composites. Composites Part A-Applied Science 2012; 43: 1630-1638.

[15] Mallon S, Koohbor B, Kidane A, Sutton MA. Fracture behavior of prestressed composites subjected to shock loading: A DIC-based study. Experimental Mechanics 2015; 55: 211-225.

[16] Sutton MA, Yan JH, Tiwari V, Schreier HW, Orteu JJ. The effect of out-of-plane motion on 2D and 3D digital image correlation measurements. Optics and Lasers in Engineering 2008; 46: 746-757.

[17] http://www.correlatedsolutions.com

[18] Xue P, Peng X, Cao J. A non-orthogonal constitutive model for characterizing woven composites. Composites Part A-Applied Science 2003; 34: 183-193.

[19] Xue P, Cao J, Chen J. Integrated micro/macro-mechanical models of woven fabric composites under large deformation. Composite Structures 2005; 70: 69-80.

[20] Kanit T, Forest S, Galliet I, Mounoury V, Jeulin D. Determination of the size of the representative volume element for random composites: Statistical and numerical approach. International Journal of Solids and Structures 2003; 40: 3647-3679.

CHAPTER 7

SUMMARY AND RECOMMENDATIONS

7.1 SUMMARY

Dynamic deformation response of polymeric foams subjected to intermediate and high velocity direct impact was studied in the first part of this research. Full-field measurements were conducted to investigate the concurrent influences of inertia loading and material compressibility, through a non-parametric stress analysis. The following remarks summarize the highlights of the first part of the present document:

- Closed-cell polymeric foam specimens with different length-to-diameter ratios were subjected to intermediate and high-velocity direct impact.
- It was clearly shown that inertia loading is significant during dynamic deformation response of polymeric foams. Presence of inertia effect makes the conventional analysis of constitutive response of low impedance polymeric foams inaccurate. Conventional analysis here is referred to the determination of strain and stresses using only boundary measured data.
- Due to the compressible nature of polymeric foams, change of density must also be incorporated in the analysis, in order to increase the level of accuracy and obtain more realistic constitutive information.
- The challenges due to the inertia and material compressibility were resolved by implementing an experimental approach based on high speed photography

and full-field measurements, in which the concurrent influences of transient deformation and change of density were compensated for through a non-parametric analysis.

- It was clearly observed that inertia loading is more prominent in the case of specimens with higher length-to-diameter ratio. This was explained through the wave propagation mechanisms in the material.
- The proposed non-parametric approach was shown to facilitate the identification of the inelastic constitutive response of the material over a wide range of strains and strain rates from the measurements conducted on a minimum number of tests. In ideal cases, the analysis can be used to identify visco-plastic constitutive laws over a great range of strain rates using a single well-controlled impact experiment.

Second par to the present document was dedicated to the study of full-field deformation response and underlying deformation mechanisms in woven composites, at mesoscopic scales. 2D and 3D Full-field measurements were conducted at submillimeter scales to reveal the non-homogeneous nature of deformation in woven composites. The results obtained in this regard can be summarized as the following:

- Tensile response of woven composites shows strong sensitivity to the angle between the applied far-field load and the fiber directions. Such sensitivity is shown in terms of elastic modulus, Poisson’s ratio, strain to failure and apparent failure mechanisms.
- Load bearing mechanisms were found to be completely different for on and off-axis specimens. In on-axis specimens, i.e. specimens loaded along the

principal fiber directions, reinforcing fibers are the main load bearing component; whereas in the case of off-axis specimens, both fibers and matrix contribute to the load bearing performance of the material.

- Strong deformation inhomogeneity was observed at mesoscopic scales. Strain inhomogeneity was found to be more pronounced in off-axis specimens.
- Low and high strain domains were identified over the surface of the specimens extracted from different angles relative to the fiber directions. For on-axis specimens, the high strain domains were located over the longitudinal fiber bundles aligned with the direction of the far-field load. In off-axis specimens, high strain domains were identified over the matrix-rich areas confined between longitudinal and transverse fiber bundles, while low strain domains were detected over fiber bundles.
- Fiber trellising was shown to be the primary mechanism behind the large global failure strain and high deformation non-linearity in off-axis specimens. This phenomenon is controlled by the concurrent stretching and rotation of the fiber bundles towards the direction of the applied tensile load.
- A quantitative analysis of fiber trellising revealed that the fiber rotation is the major phenomenon contributing to the large strain to failures observed for the off-axis woven composites; while the material, regardless of on- or off-axis loading conditions, fails when the magnitude of strain on the fiber bundles reaches the maximum tolerable strain of the reinforcing fiber material.

7.2 RECOMMENDATIONS

Regarding the non-parametric dynamic stress analysis described in this work, the following recommendations are proposed:

- The approach detailed in this document is a general methodology that can be employed to study the high strain rate deformation response of soft and low mechanical impedance materials. The application of this methodology in the analysis of the constative response of soft organic and inorganic materials is recommended for the future studies.
- One particular concept that has recently gained extensive attention is the use of graded foams in a number of applications, including but not limited to superior energy absorbing components [1-3], armor and recreational helmets [4], car bumpers [5] and footwear design [6]. The stress analysis approach detailed in this work can be implemented for an accurate assessment of the energy absorption and overall load bearing performance of layered and continuously graded foams for various applications. This idea has the potential for the design of next generation energy dissipating components.
- The viscoplastic constitutive model identification detailed in Chapter 3 can be combined with controlled high temperature experimental measurements to facilitate the study of the deformation response of materials under extreme strain rate and temperature conditions.
- The main limiting points in the experimental work conducted in this work were the temporal and spatial resolution of the camera system. Employing more advanced camera systems, particularly newly developed ultra-high

speed cameras currently available, can definitely result in more accurate evaluation of the dynamic behavior of low impedance cellular materials.

Regarding the full-field characterization of woven composites at mesoscopic scales, the following remarks summarize the scope of the recommended future work:

- In order to gain a better insight on the concept of fiber trellising mechanism, application of the described experimental methods on single-layer unidirectional and woven laminas is proposed.
- The utilized full-field deformation characterization approach can be further extended to identify the representative volume element (RVE) of woven composites through experimental measurements. This has already been investigated for the case of metallic materials [7], but no evidence on the applicability of such methodology in composite materials can be found in the available literature.
- A potential application of the meso-scale strain measurement in woven composites is in the identification of local strain histories over low-strain and high-strain domains. Such local data can be directly used to establish a correlation between the local deformation and globally applied strains on a woven composite material. The significance of this is in the multiscale and micromechanics modeling approaches where the boundary conditions applied on global scale can be directly related to the small scale deformation response. the ultimate goal here would be to determine a single master curve [8] that (1)

is a function of the orientation angle the specimen, and (2) correlates the globally applied stress to the local strain history within the material.

7.3 LIST OF REFERENCES

[1] Gupta N. A functionally graded synthetic foam material for high energy absorption under compression. Materials Letters 2007; 61: 979-982.

[2] Cui L, Kiernan S, Gilchrist MD. Designing the energy absorption capacity of functionally graded foam materials. Materials Science and Engineering A 2009; 507: 215-225.

[3] Koohbor B, Kidane A. Design optimization of continuously and discretely graded foam materials for efficient energy absorption. Materials & Design 2016; 102: 151-161.

[4] Rueda MA, Cui L, Gilchrist MD. Optimization of energy absorbing liner for equestrian helmets. Part I: Layered foam liner. Materials & Design 2009; 30: 3405-3413.

[5] Xiao Z, Fang J, Sun G, Li Q. Crashworthiness design for functionally graded foam-filled bumper beam. Advances in Engineering Software 2015; 85: 81-95.

[6] Shimazaki Y, Nozu S, Inoue T. Shock-absorbing properties of functionally graded EVA laminates for footwear design. Polymer Testing 2016; 54: 98-103.

[7] Efstathiou C, Sehitoglu H, Lambros J. Multiscale strain measurements of plastically deforming polycrystalline titanium: Role of deformation heterogeneities. International Journal of Plasticity 2010; 26: 93-106.

[8] Ogihara S, Reifsnider KL. Characterization of nonlinear behavior in woven composite laminates. Applied Composite Materials 2002; 9: 249-263.

[9] Tamuzs V, Dzezitis K, Reifsnider K. Fatigue of woven composite laminates in off-axis loading I. The mastercurves. Applied Composite Materials 2004; 11: 259-279.

BIBLIOGRAPHY

Aloui S, Othman R, Poitou A, Guegan P, El-Borgi S. Non-parametric identification of the non-homogeneous stress in high strain-rate uni-axial experiments. Mechanical Research Communications 2008; 35: 392-397.

Alsayednoor J, Harrison P, Guo Z. Large strain compressive response of 2-D periodic representative volume element for random foam microstructures. Mechanics of Materials 2013; 66: 7-20.

Avalle M, Belingardi G, Montanini R. Characterization of polymeric structural foams under compressive impact loading by means of energy-absorption diagram. International Journal of Impact Engineering 2001; 25: 445-472.

Avril S, Pierron F, Sutton M, Yan J. Identification of elasto-visco-plastic parameters and characterization of Lüders behavior using digital image correlation and the virtual fields method. Mechanics of Materials 2008; 40: 729-742.

Bacon C. An experimental method for considering dispersion and attenuation in a viscoelastic Hopkinson bar. Experimental Mechanics 1998; 38(4): 242-249.

Bobbili R, Madhu V, Gogia AK. Neural network modeling to evaluate the dynamic flow stress of high strength armor steels under high strain rate compression. Defence Technology 2014; 10: 334-342.

Boisse P, Zouari B, Gasser A. A mesoscopic approach for simulation of woven fibre composite forming. Composite Science and Technology 2005; 65: 429-436.

Bouix R, Viot, Lataillade JL. Polypropylene foam behavior under dynamic loadings: Strain rate, density and microstructure effects. International Journal of Impact Engineering 2009; 36: 329-342.

Canal LP, Gonzalez C, Molina-Aldareguia JM, Segurado J, Llorca J. Application of digital image correlation at micro-scale in fiber-reinforced composites. Composites Part A-Applied Science 2012; 43: 1630-1638.

Casem DT, Fourney WL, Chang P. A polymeric split Hopkinson pressure bar instrumented with velocity gages. Experimental Mechanics 2003; 43(4): 420-427.

Casem DT, Fourney W, Chang P. Wave separation in viscoelastic pressure bars using single-point measurements of strain and velocity. Polymer Testing 2003; 22(2): 155-164.

Chen W, Zhang B, Forrestal MJ. A split Hopkinson bar technique for low-impedance materials. Experimental Mechanics 1999; 39(2): 81-85.

Chen W, Lu F, Winfree N. High strain rate compressive behavior of a rigid polyurethane foam with various densities. Experimental Mechanics 2002; 42(1): 65-73.

Chen R, Huang S, Xia K, Lu F. A modified Hopkinson bar system for testing ultra-soft materials under intermediate strain rates. In: DYMAT-International Conference on the Mechanical and Physical Behaviour of Materials under Dynamic Loading, vol. 1, pp. 389-394. EDP Sciences, 2009. DOI: 10.1051/dymat/2009055

Cui L, Kiernan S, Gilchrist MD. Designing the energy absorption capacity of functionally graded foam materials. Materials Science and Engineering A 2009; 507: 215-225.

Daggumati S, Voet E, Van Paepegem W, Degrieck J, Xu J, Lomov SV, Verpoest I. Local strain in a 5-harness satin weave composite under static tension: Part 1 – Experimental analysis. Composite Science and Technology 2011; 71: 1171-1179.

Davies EDH, Hunter SC. The dynamic compression testing of solids by the method of the split Hopkinson pressure bar. Journal of Mechanics and Physics of Solids 1963; 11(3): 155-179.

Efstathiou C, Sehitoglu H, Lambros J. Multiscale strain measurements of plastically deforming polycrystalline titanium: Role of deformation heterogeneities. International Journal of Plasticity 2010; 26: 93-106.

Fard MY, Sadat SM, Raji BB, Chattopadhyay A. Damage characterization of surface and sub-surface defects in stitch-bonded biaxial carbon/epoxy composites. Composites Part B-Engineering 2014; 56: 821-829.

Field JE, Walley SM, Proud WG, Goldrein HT, Siviour CR. Review of experimental techniques for high rate deformation and shock studies. International Journal of Impact Engineering 2004; 30: 725-775.

Flores-Johnson EA, Li QM. Low velocity impact on polymeric foams. Journal of Cellular Plastics 2011; 47: 45-63.

Gama BA, Lopatnikov SL, Gillespie JW. Hopkinson bar experimental technique: A critical review. Applied Mechanics Reviews 2004; 57(4): 223-250.

Gardner N, Wang E, Kumar P, Shukla A. Blast mitigation in a sandwich composite using graded core and polyurea interlayer. Experimental Mechanics 2012; 52: 119-133.

Gibson LJ, Ashby MF. Cellular solids: Structure and properties. 2nd ed. Oxford. 1997.

Gilat A, Schmidt TE, Walker AL. Full field measurement in compression and tensile split Hopkinson bar experiments. Experimental Mechanics 2009; 49: 291-302.

Godara A, Raabe D. Influence of fiber orientation on global mechanical behavior and mesoscale strain localization in a short glass-fiber-reinforced epoxy polymer composite during tensile deformation investigated using digital image correlation. Composite Science and Technology 2007; 67: 2417-2427.

Godara A, Raabe D, Bergmann I, Putz R, Muller U. Influence of additives on the global mechanical behavior and the microscopic strain localization in wood reinforced polypropylene composites during tensile deformation investigated using digital image correlation. Composite Science and Technology 2008; 69: 139-146.

Gupta N. A functionally graded synthetic foam material for high energy absorption under compression. Materials Letters 2007; 61: 979-982.

Hopkinson B. A method of measuring the pressure produced in the detonation of high explosives or by the impact of bullets. Philosophical Transactions of the Royal Society of London 1914; 213: 437-456.

Ivanov D, Ivanov S, Lomov S, Verpoest I. Strain mapping analysis of textile composites. Optics and Lasers in Engineering 2009; 47: 360-370.

Iwamoto T, Yokoyama T. Effects of radial inertia and end friction in specimen geometry in split Hopkinson pressure bar tests: A computational study. Mechanics of Materials 2012; 51: 97-109.

Kanaun S, Tkachenko O. Representative volume element and effective elastic properties of open cell foam materials with random microstructures. Journal of Mechanics of Materials and Structures. 2007; 2(7): 1607-1628.

Kanit T, Forest S, Galliet I, Mounoury V, Jeulin D. Determination of the size of the representative volume element for random composites: statistical and numerical approach. International Journal of Solids and Structures 2003; 40: 3647-3679.

Kidane A. On the Failure and Fracture of Polymer Foam Containing Discontinuities. ISRN Materials Science 2013, DOI:10.1155/2013/408596.

Koohbor B, Mallon S, Kidane A, Sutton MA. A DIC-based study of in-plane mechanical response and fracture of orthotropic carbon fiber reinforced composites. Composites Part B-Engineering 2014; 66: 388-399.

Koohbor B, Mallon S, Kidane A, Lu WY. The deformation and failure response of closed-cell PMDI foams subjected to dynamic impact loading. Polymer Testing 2015; 44: 112-124.

Koohbor B, Kidane A, Lu WY, Sutton MA. Investigation of the dynamic stress-strain response of compressible polymeric foam using a non-parametric analysis. International Journal of Impact Engineering 2016; 91: 170-182.

Koohbor B, Kidane A. Design optimization of continuously and discretely graded foam materials for efficient energy absorption. Materials and Design 2016; 102: 151-161.

Kraft SM, Moslehy EA, Bai Y, Gordon AP. Characterization of the orthotropic elastic constants of a micronic woven wire mesh via digital image correlation. Experimental Mechanics 2014; 54: 501-514.

Lam SW, Xue P, Tao XM, Yu TX. Multi-scale study of tensile properties and large deformation mechanisms of polyethylene terephthalate/polypropylene knitted composites. Composite Science and Technology 2003; 63: 1337-1348.

Lava P, Cooreman S, Coppieters S, De Strycker M, Debruyne D. Assessment of measuring errors in DIC using deformation fields generated by plastic FEA. Optics and Lasers in Engineering 2009; 47: 747-753.

Lee D, Tippur H, Bogert P. Quasi-static and dynamic fracture of graphite/epoxy composites: An optical study of loading-rate effects

Linul E, Marsavina L, Voiconi T, Sadowski T. Study of factors influencing the mechanical properties of polyurethane foams under dynamic compression. Journal of Physics: Conference Series 2013; 451: 1-6.

Liu J, Saletti D, Pattofatto S, Zhao H. Impact testing of polymer foam using Hopkinson bars and digital image analysis. Polymer Testing 2014; 36: 101-109.

Liu Q, Subhash G, Gao XL. A parametric study on crushability of open-cell structural polymeric foams. Journal of Porous Materials 2005; 12: 233-248.

Liu Q, Subhash G. A phenomenological constitutive model for foams under large deformations. Polymer Engineering and Science 2004; 44(3): 463-473.

Lomov SV, Ivanov DS, Verpoest I, Zako M, Kurashiki T, Nakai H, Hirosawa S. Meso-FE modeling of textile composites: Road map, data flow and algorithms. Composite Science and Technology 2007; 67: 1870-1891.

Lomov SV, Ivanov DS, Verpoest I, Zako M, Kurashiki T, Nakai H, Molimard J, Vautrin A. Full-field strain measurements for validation of meso-FE analysis of textile composites. Composites Part A-Applied Science 2008; 39: 1218-1231.

Lomov SV, Boisse P, Deluycker E, Morestin F, Vanclooster K, Vandepitte D, Verpoest I, Willems A. Full-field strain measurements in textile deformability studies. Composites Part A-Applied Science 2008; 39: 1232-1244.

Lu WY. Mechanical characterization of rigid polyurethane foams. Sandia Report 2014: SADN2014-20708.

Mallon S, Koohbor B, Kidane A, Sutton MA. Fracture behavior of prestressed composites subjected to shock loading: A DIC-based study. Experimental Mechanics 2015; 55: 211-225.

Mallon S, Koohbor B, Kidane A. Fracture of pre-stressed woven glass fiber composite exposed to shock loading. In: Song B, Casem D, Kimberley J (Editors), Dynamic behavior of materials – Volume 1, Proceedings of the 2014 Annual Conference on Experimental and Applied Mechanics, Springer, 2015, pp 213-219. DOI 10.1007/978-3-319-06995-1_32

Mallon S, Kidane A, Lu WY. Full-field deformation observation of polymer foam subjected to shock loading. In: Song B, Casem D, Kimberley J (Editors), Dynamic behavior of materials – Volume 1, Proceedings of the 2014 Annual Conference on Experimental and Applied Mechanics, Springer, 2015, pp 83-89. DOI 10.1007/978-3-319-06995-1_14

Moulart R, Pierron F, Hallett SR, Wisnom MR. Full-field strain measurement and identification of composites moduli at high strain rate with the virtual fields methods. Experimental Mechanics 2011; 51: 509-536.

Mulliken AD, Boyce MC. Mechanics of the rate-dependent elastic-plastic deformation of glassy polymers from low to high strain rates. International Journal of Solids and Structures 2006; 43: 1331-1356.

Nagy A, Ko WL, Lindholm US. Mechanical behavior of foamed materials under dynamic compression. Journal of Cellular Plastics 1974; 10(3): 127-134.

Naouar N, Vidal-Salle E, Schneider J, Maire E, Boisse P. Meso-scale FE analyses of textile composite reinforcement deformation based on X-ray computed tomography. Composite Structures 2014; 116: 165-176.

Nicholas T, Recht RF. Introduction to impact phenomena. In: High Velocity Impact Dynamics, Edited by Zukas JA. 1990, John Wiley & Sons, 1990.

Nicoletto G, Anzelotti G, Riva E. Mesoscopic strain fields in woven composites: Experiments vs. finite element modeling. Optics and Lasers in Engineering 2009; 47: 352-359.

Ogihara S, Reifsnider KL. Characterization of nonlinear behavior in woven composite laminates. Applied Composite Materials 2002; 9: 249-263.

Othman R, Aloui S, Poitou A. Identification of non-homogeneous stress fields in dynamic experiments with a non-parametric method. Polymer Testing 2010; 29: 616-623.

Ouellet S, Cronin D, Worswick M. Compressive response of polymeric foams under quasi-static, medium and high strain rate conditions. Polymer Testing 2006; 25: 731-743.

Ouellet S, Cronin DS, Moulton J, Petel EO. High rate characterization of polymeric closed-cell foams: Challenges related to size effects. In: Chalivendra V, Song B, Casem D (Editors), Dynamic behavior of materials – Volume 1, Proceedings of the 2012 Annual Conference on Experimental and Applied Mechanics, Springer, 2013, pp 21-28. DOI 10.1007/978-1-4614-4238-7_4

Pal S, Maiti S, Subhash G. Effect of microscopic deformation mechanisms on the dynamic response of soft cellular materials. Mechanics of Materials 2010; 42: 118-133.

Petel OE, Ouellet S, Frost DL, Higgins AJ. Shock Hugoniot measurements in foam. Journal of Physics: Conference Series 2014; 500: 1-6.

Pierron F, Sutton MA, Tiwari V. Ultra high speed DIC and virtual fields method analysis of a three point bending impact test on an aluminum bar. Experimental Mechanics 2011; 51: 537-563.

Pierron F, Forquin P. Ultra-high-speed full-field deformation measurements on concrete spalling specimens and stiffness identification with the virtual fields method. Strain 2012; 48: 388-405.

Pierron F, Grédiac M. The virtual fields method: Extracting constitutive mechanical parameters from full-field deformation measurements. Springer, NY, 2012.

Pierron F, Zhu H, Siviour C. Beyond Hopkinson's bar. Philosophical Transactions of the Royal Society A 2014; 372: 20130195.

Pollock P, Yu L, Sutton MA, Guo S, Majumdar P, Gresil M. Full-field measurements for determining orthotropic elastic parameters of woven glass-epoxy composites using off-axis tensile specimens. Experimental Techniques 2012; 38: 61-71.

Ravindran S, Tessema A, Kidane A. Local deformation and failure mechanisms of polymer bonded energetic materials subjected to high strain rate loading. Journal of Dynamic Behavior of Materials 2016; 2: 146-156.

Rossi M, Lava P, Pierron F, Debruyne D, Sasso M. Effect of DIC resolution, noise and interpolation error on identification results with the VFM. Strain 2015; 51: 206-222.

Rueda MA, Cui L, Gilchrist MD. Optimization of energy absorbing liner for equestrian helmets. Part I: Layered foam liner. Materials & Design 2009; 30: 3405-3413.

Samanta SK. Dynamic deformation of aluminum and copper at elevated temperatures. Journal of Mechanics and Physics of Solids 1971; 19: 117.

Sharma A, Shukla A, Prosser RA. Mechanical characterization of soft materials using high speed photography and split Hopkinson pressure bar technique. Journal of Materials Science 2002; 37(5): 1005-1017.

Shimazaki Y, Nozu S, Inoue T. Shock-absorbing properties of functionally graded EVA laminates for footwear design. Polymer Testing 2016; 54: 98-103.

Sjoblom PO, Hatness JT. On low-velocity impact testing of composite materials. Journal of Composite Materials 1988; 22: 30-52.

Song B, Chen W. Dynamic stress equilibrium in split Hopkinson pressure bar tests on soft materials. Experimental Mechanics 2004; 44: 300-312.

Song B, Chen W, Frew DJ. Dynamic compressive response and failure behavior of an epoxy syntactic foam. Journal of Composite Materials 2004; 38(11): 915-936.

Subhash G, Liu Q. Crushability maps for structural polymeric foams in uniaxial loading under rigid confinement. Experimental Mechanics 2004; 44(3): 289-294.

Subhash G, Liu Q, Gao X. Quasistatic and high strain rate uniaxial compressive response of polymeric structural foams. International Journal of Impact Engineering 2006; 32(7): 1113-1126.

Sutton MA, Yan JH, Tiwari V, Schreier HW, Orteu JJ. The effect of out-of-plane motion on 2D and 3D digital image correlation measurements. Optics and Lasers in Engineering 2008; 46: 746-757.

Sutton MA, Orteu JJ, Schrier HW. Image correlation for shape, motion and deformation measurements. Springer. NY. 2009.

Tabatabaei SA, Lomov SV, Verpoest I. Assessment of embedded element technique in meso-FE modeling of fibre reinforced composites. Composite Structures 2014; 107: 436-446.

Tamuzs V, Dzezitis K, Reifsnider K. Fatigue of woven composite laminates in off-axis loading I. The mastercurves. Applied Composite Materials 2004; 11: 259-279.

Tan PJ, Reid SR, Harrigan JJ. On the dynamic mechanical properties of open-cell metal foams–A re-assessment of the 'simple-shock theory'. International Journal of Solids and Structures 2012; 49: 2744-2753.

Taylor G. The use of flat-ended projectiles for determining dynamic yield stress – I. Theoretical considerations. Philosophical Transactions of the Royal Society A 1948; 194: 289-299.

Tekoglu C, Gibson LJ, Pardoen T, Onck PR. Size effects in foams: Experiments and modeling. Progress in Materials Science 2011; 56: 109-138.

Ullah H, Harland AR, Silberchmidt VV. Characterization of mechanical behavior and damage analysis of 2D woven composites under bending. Composites Part B-Engineering 2015; 75: 156-166.

Viot P, Beani F, Lataillade JL. Polymeric foam behavior under dynamic compressive loading. Journal of Materials Science 2005; 40: 5829-5837.

Wang L, Labibes K, Azari A, Pluvinage G. Generalization of split Hopkinson bar technique to use viscoelastic bars. International Journal of Impact Engineering 1994; 15(5): 669-686.

Wang L, Ding Y, Yang L. Experimental investigation on dynamic constitutive behavior of aluminum foams by new inverse methods from wave propagation measurements. International Journal of Impact Engineering 2013; 62: 48-59.

Whisler D, Kim H. Experimental and simulated high strain dynamic loading of polyurethane foam. Polymer Testing 2015; 41: 219-230.

Xiao Z, Fang J, Sun G, Li Q. Crashworthiness design for functionally graded foam-filled bumper beam. Advances in Engineering Software 2015; 85: 81-95.

Xing L, Reifsnider KL, Huang X. Progressive damage modeling for large deformation loading of composite structures. Composite Science and Technology 2009; 69: 780-784.

Xue P, Peng X, Cao J. A non-orthogonal constitutive model for characterizing woven composites. Composites Part A-Applied Science 2003; 34: 183-193.

Xue P, Cao J, Chen J. Integrated micro/macro-mechanical model of woven fabric composites under large deformation. Composite Structures 2005; 70: 69-80.

Yi J, Boyce MC, Lee GF, Balizer E. Large deformation rate-dependent stress-strain behavior of polyurea and polyurethanes. Polymer 2006; 47: 319-329.

Yoon S, Giannakopoulos I, Siviour CR. Application of the virtual fields method to the uniaxial behavior of rubbers at medium strain rates. International Journal of Solids and Structures 2015; 69-70: 553-568.

Yunoshev AS, Sil'vestrov VV. Development of the polymeric split Hopkinson bar technique. Journal of Applied Mechanics and Technical Physics 2001; 42(3): 558-564.

Zhang C, Binienda WK. A meso-scale finite element model for simulating free-edge effect in carbon/epoxy textile composite. Mechanics of Materials 2014; 76: 1-19.

Zhang J, Kikuchi N, Li V, Yee A, Nusholtz G. Constitutive modeling of polymeric foam material subjected to dynamic crash loading. International Journal of Impact Engineering 1998; 21(5): 369-386.

Zhang X, Zhang H. Optimal design of functionally graded foam material under impact loading. International Journal of Mechanical Sciences 2013; 68: 199-211.

Zhao H. Testing of polymeric foams at high and medium strain rates. Polymer Testing 1997; 16: 507-516.

Zhao H, Gary G, Klepaczko JR. On the use of a viscoelastic split Hopkinson pressure bar. International Journal of Impact Engineering 1997; 19(4): 319-330.

APPENDIX A

PUBLISHER PERMISSION

Permission to reuse the paper entitled “Investigation of the dynamic stress-strain response of compressible polymeric foam using a non-parametric analysis” as Chapter 2 in this document:

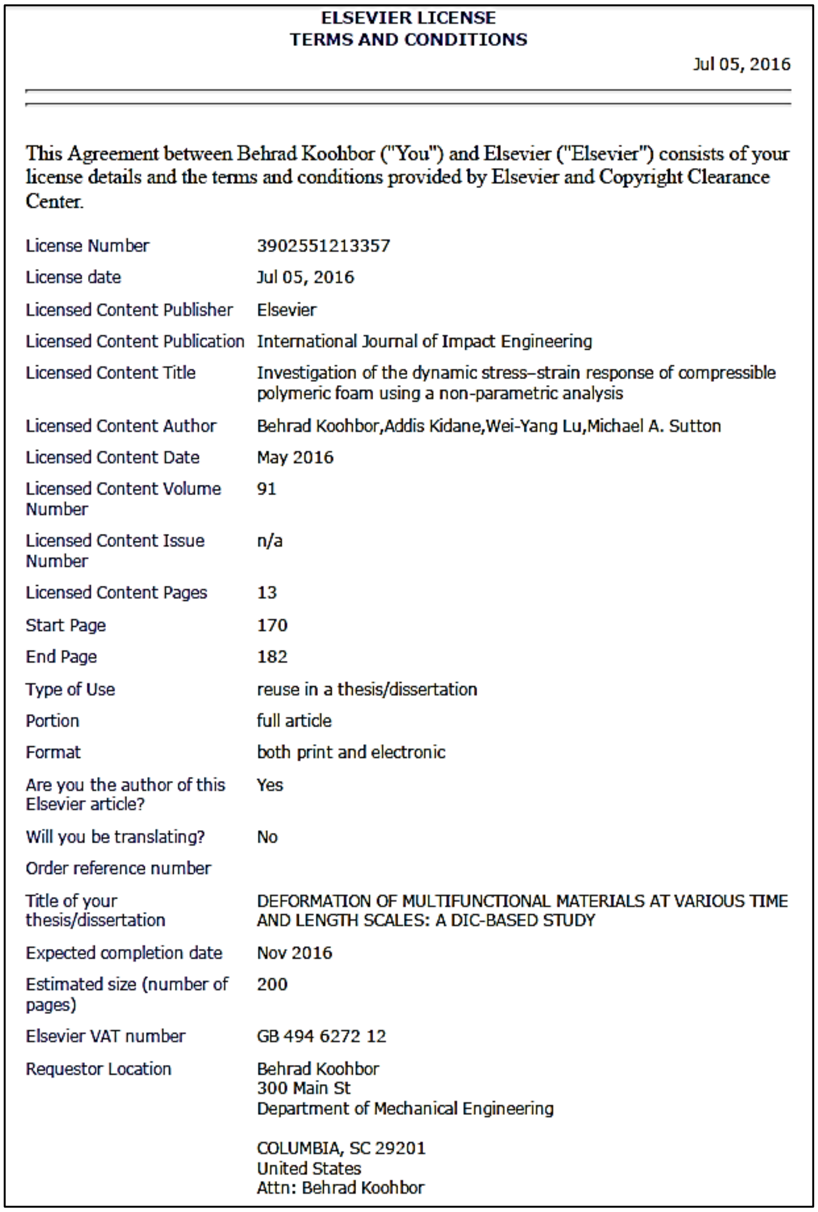

ELSEVIER LICENSE
TERMS AND CONDITIONS

Jul 05, 2016

This Agreement between Behrad Koohbor ("You") and Elsevier ("Elsevier") consists of your license details and the terms and conditions provided by Elsevier and Copyright Clearance Center.

License Number	3902551213357
License date	Jul 05, 2016
Licensed Content Publisher	Elsevier
Licensed Content Publication	International Journal of Impact Engineering
Licensed Content Title	Investigation of the dynamic stress–strain response of compressible polymeric foam using a non-parametric analysis
Licensed Content Author	Behrad Koohbor,Addis Kidane,Wei-Yang Lu,Michael A. Sutton
Licensed Content Date	May 2016
Licensed Content Volume Number	91
Licensed Content Issue Number	n/a
Licensed Content Pages	13
Start Page	170
End Page	182
Type of Use	reuse in a thesis/dissertation
Portion	full article
Format	both print and electronic
Are you the author of this Elsevier article?	Yes
Will you be translating?	No
Order reference number	
Title of your thesis/dissertation	DEFORMATION OF MULTIFUNCTIONAL MATERIALS AT VARIOUS TIME AND LENGTH SCALES: A DIC-BASED STUDY
Expected completion date	Nov 2016
Estimated size (number of pages)	200
Elsevier VAT number	GB 494 6272 12
Requestor Location	Behrad Koohbor 300 Main St Department of Mechanical Engineering COLUMBIA, SC 29201 United States Attn: Behrad Koohbor

Permission to reuse the paper entitled “Characterizing the constitutive response and energy absorption of rigid polymeric foams subjected to intermediate-velocity impact” as Chapter 4 in this document:

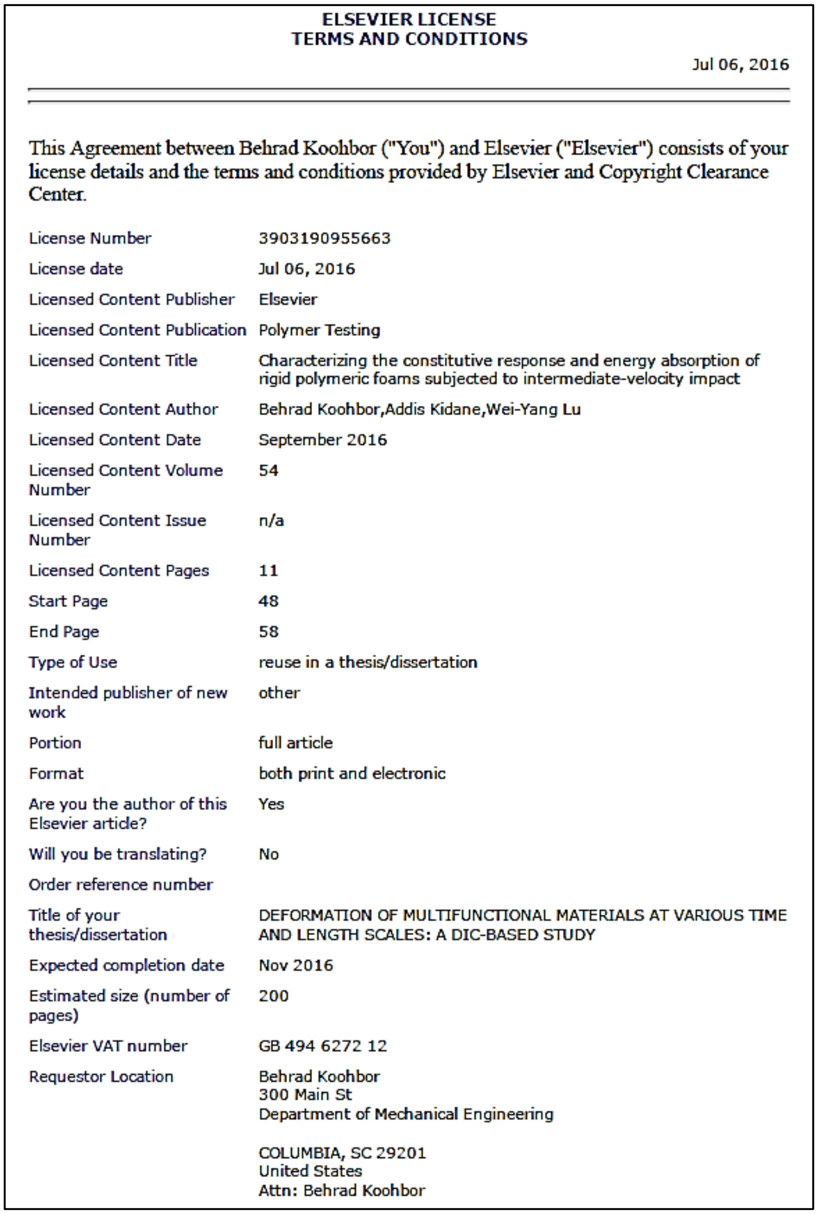

ELSEVIER LICENSE
TERMS AND CONDITIONS

Jul 06, 2016

This Agreement between Behrad Koohbor ("You") and Elsevier ("Elsevier") consists of your license details and the terms and conditions provided by Elsevier and Copyright Clearance Center.

License Number	3903190955663
License date	Jul 06, 2016
Licensed Content Publisher	Elsevier
Licensed Content Publication	Polymer Testing
Licensed Content Title	Characterizing the constitutive response and energy absorption of rigid polymeric foams subjected to intermediate-velocity impact
Licensed Content Author	Behrad Koohbor,Addis Kidane,Wei-Yang Lu
Licensed Content Date	September 2016
Licensed Content Volume Number	54
Licensed Content Issue Number	n/a
Licensed Content Pages	11
Start Page	48
End Page	58
Type of Use	reuse in a thesis/dissertation
Intended publisher of new work	other
Portion	full article
Format	both print and electronic
Are you the author of this Elsevier article?	Yes
Will you be translating?	No
Order reference number	
Title of your thesis/dissertation	DEFORMATION OF MULTIFUNCTIONAL MATERIALS AT VARIOUS TIME AND LENGTH SCALES: A DIC-BASED STUDY
Expected completion date	Nov 2016
Estimated size (number of pages)	200
Elsevier VAT number	GB 494 6272 12
Requestor Location	Behrad Koohbor 300 Main St Department of Mechanical Engineering COLUMBIA, SC 29201 United States Attn: Behrad Koohbor

Permission to reuse the paper entitled "Meso-scale strain localization and failure response of an orthotropic woven glass fiber reinforced composite" as Chapter 5 in this document:

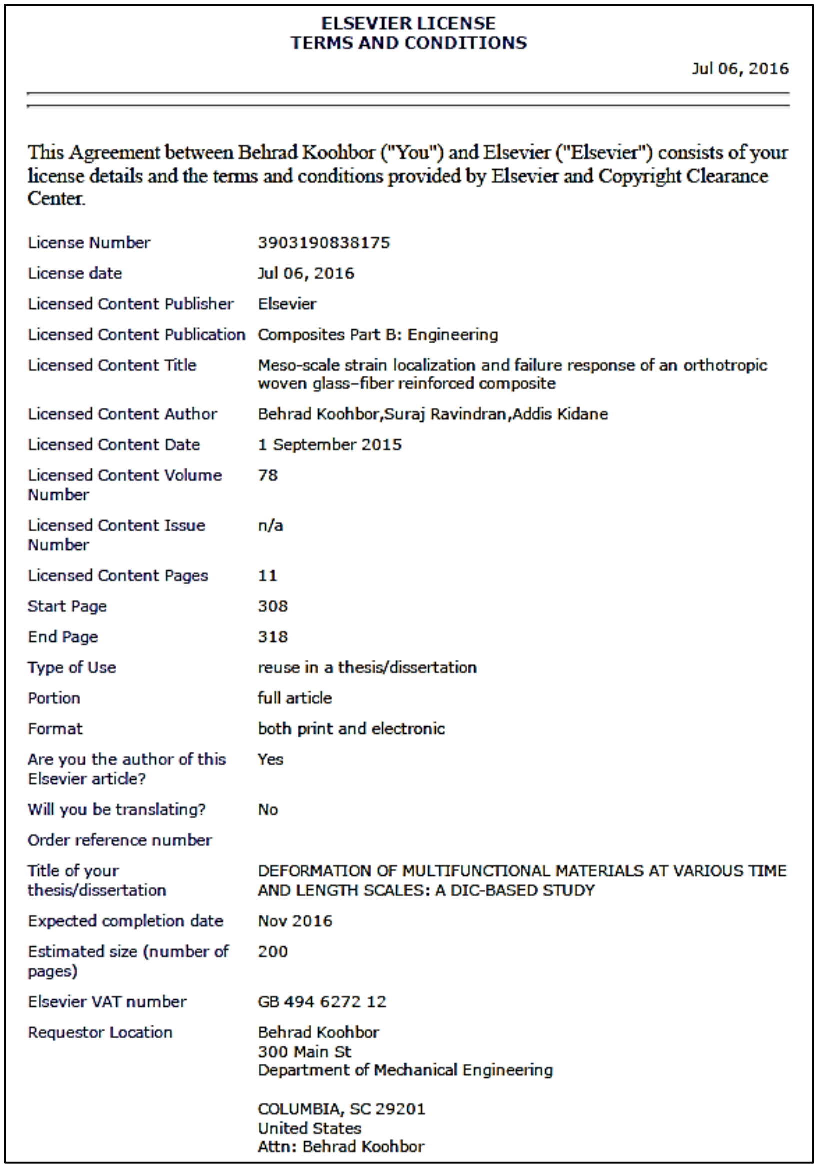

ELSEVIER LICENSE
TERMS AND CONDITIONS

Jul 06, 2016

This Agreement between Behrad Koohbor ("You") and Elsevier ("Elsevier") consists of your license details and the terms and conditions provided by Elsevier and Copyright Clearance Center.

License Number	3903190838175
License date	Jul 06, 2016
Licensed Content Publisher	Elsevier
Licensed Content Publication	Composites Part B: Engineering
Licensed Content Title	Meso-scale strain localization and failure response of an orthotropic woven glass–fiber reinforced composite
Licensed Content Author	Behrad Koohbor,Suraj Ravindran,Addis Kidane
Licensed Content Date	1 September 2015
Licensed Content Volume Number	78
Licensed Content Issue Number	n/a
Licensed Content Pages	11
Start Page	308
End Page	318
Type of Use	reuse in a thesis/dissertation
Portion	full article
Format	both print and electronic
Are you the author of this Elsevier article?	Yes
Will you be translating?	No
Order reference number	
Title of your thesis/dissertation	DEFORMATION OF MULTIFUNCTIONAL MATERIALS AT VARIOUS TIME AND LENGTH SCALES: A DIC-BASED STUDY
Expected completion date	Nov 2016
Estimated size (number of pages)	200
Elsevier VAT number	GB 494 6272 12
Requestor Location	Behrad Koohbor 300 Main St Department of Mechanical Engineering COLUMBIA, SC 29201 United States Attn: Behrad Koohbor

Permission to reuse the paper entitled "Meso-scale study of non-linear tensile response and fiber trellising in woven composites" as Chapter 6 in this document:

Title: Meso-scale study of non-linear tensile response and fiber trellising mechanisms in woven composites:

Author: Behrad Koohbor, Suraj Ravindran, Addis Kidane

Publication: Journal of Reinforced Plastics and Composites

Publisher: SAGE Publications

Date: 06/01/2016

Copyright © 2016, © SAGE Publications

If you're a copyright.com user, you can login to RightsLink using your copyright.com credentials. Already a RightsLink user or want to learn more?

Gratis Reuse

- Without further permission, as the Author of the journal article you may:
  - post the accepted version (version 2) on your personal website, department's website or your institution's repository. You may NOT post the published version (version 3) on a website or in a repository without permission from SAGE.
  - post the accepted version (version 2) of the article in any repository other than those listed above 12 months after official publication of the article.
  - use the published version (version 3) for your own teaching needs or to supply on an individual basis to research colleagues, provided that such supply is not for commercial purposes.
  - use the accepted or published version (version 2 or 3) in a book written or edited by you. To republish the article in a book NOT written or edited by you, permissions must be cleared on the previous page under the option 'Republish in a Book/Journal' by the publisher, editor or author who is compiling the new work.
- When posting or re-using the article electronically, please link to the original article and cite the DOI.